DAMAGE AND DAMAGE TOLERANCE OF HIGH TEMPERATURE COMPOSITES AND SANDWICH COMPOSITE STRUCTURES

by Michael Wladyslaw Czabaj

DAMAGE AND DAMAGE TOLERANCE OF HIGH TEMPERATURE COMPOSITES AND SANDWICH COMPOSITE STRUCTURES

A Dissertation

Presented to the Faculty of the Graduate School

of Cornell University

in Partial Fulfillment of the Requirements for the Degree of

Doctor of Philosophy

by

Michael Wladyslaw Czabaj

August 2010

DAMAGE AND DAMAGE TOLERANCE OF HIGH TEMPERATURE COMPOSITES AND SANDWICH COMPOSITE STRUCTURES

Michael Wladyslaw Czabaj, Ph.D.

Cornell University 2010

The first part of this dissertation examines application of polyimide matrix composites in severe hygrothermal environments. In particular, this work focuses on prediction of blistering and delamination of moisture-saturated graphite/polyimide composites due to rapid temperature heat-up. Two new experimental test methods are developed to determine initiation of blistering and delamination in laminates for a range of heating rates, moisture saturation levels, and extent of internal damage. The first method determines the onset of steam-induced blistering, or void formation, in initially undamaged specimens by monitoring their expansion during a ramped temperature increase. The second method involves testing of moisture-saturated composite specimens with pre-implanted circular delaminations. In these experiments, a set of high-temperature transverse extensometers are used to measure deformation of the delaminated region and determine the onset of delamination growth. For each method, a numerical hygrothermal-mechanical model is developed and implemented to predict internal steam pressure at onset of damage. In the case of steam-induced delamination, the internal pressure calculation is combined with linear elastic fracture mechanics to predict onset of delamination growth. Both studies demonstrate that there is a direct competition between initiation of blistering and onset of delamination growth during a hygrothermal cycle. This study suggests that there exists a critical flaw size below which blistering is

likely to occur and above which delamination growth is a preferred mode of failure.

The second part of this dissertation describes a combined experimental and computational effort to investigate damage tolerance of sandwich composite materials to barely visible impact damage. The experimental investigation focuses on sandwich panels with various combinations of thin-skin, quasi-isotropic, carbon/epoxy face sheets and low density aluminum honeycomb cores. The impact damage is induced in test specimens using quasi-static indentation with spherical indentors. The damage tolerance is measured using a compression after impact test. The evolution of impact damage and ultimate failure during compression is visualized using a shadow Moiré technique. The observed failure is typically due to dent deepening, delamination buckling and growth, compressive fiber failure, or any combination thereof. The residual compressive strength data demonstrate sensitivity to type of face sheet layup, core thickness and density, extent of initial indentation damage, and observed mode of failure. Based on the experimental results, a numerical simulation of the quasi-static indentation and compression after impact experiments is carried out in the frame work of the finite element method. To simulate the process of indentation and dent growth during compression, two distinct honeycomb core models are implemented. Additionally, a progressive, intra-laminar, failure model is implemented to simulate the fiber failure during compression. A comparison between experimental data and numerical results reveals that explicit modeling of honeycomb core geometry provides accurate prediction of damage resulting from quasi-static indentation. Moreover, the simulation of compression after impact successfully captures failure due to unstable indentation growth and compressive fiber failure; however, the model largely overestimates

the residual strength predictions. The inaccurate strength predictions illustrates a need for an improved modeling methodology that incorporates simulation of the initiation and evolution of inter-laminar delaminations.

BIOGRAPHICAL SKETCH

Michael W. Czabaj was born on January 5th, 1981 in Rzeszów, Poland, and moved to United States at age of 15. In 2000 he graduated from John F. Kennedy Memorial High School in Iselin, New Jersey. He attended Syracuse University and graduated with a Bachelor of Science degree in Aerospace Engineering. He began the Ph.D. program at Cornell University in the Department of Theoretical and Applied Mechanics in 2004.

To my parents.

ACKNOWLEDGEMENTS

First, I would like to thank my parents, to whom I dedicate this work, for sacrificing so much on my behalf. Without their encouragement and support my college education would have been impossible. I would like to thank my adviser, Dr. Alan T. Zehnder, for his support and guidance over the past six years. I consider myself very fortunate for having an adviser who was always available and willing to help me with my research. I would also like to thank my undergraduate adviser, Dr. Barry D. Davidson, for inspiring me to pursue my graduate education and for continuing to be my friend and mentor.

I would like to thank my sister, Olga, for being a great role model and her husband, Sachin, for always providing sound and interesting advice. I must thank my two friends, William Whitacre and Ranajay Ghosh, for their companionship during my stay at Cornell. I will always fondly remember our coffee break conversations outside of Thurston Hall. I would like to thank Miss Ashley Spear for being an important part of my life during my last year at Cornell. I would also like to thank her for proofreading and correcting most grammatical and spelling errors in this document. Lastly, I would like to thank Professors Herbert Hui, Anthony Ingraffea, Leigh Phoenix, and Petru Petrina as well as Paul Bishop, John Sinnot, Yuanming Zheng, John Hunt, and Dan Mittler. Without their help and encouragement, completion of this work would not have been possible.

My dissertation work was funded through the NASA Constellation University Institutes Project (CUIP), under grant NCC3-989 with Claudia Meyer as the project monitor.

TABLE OF CONTENTS

LIST OF TABLES

LIST OF FIGURES

CHAPTER 1

INTRODUCTION

Fiber-reinforced polymer matrix composites (PMCs) represent a versatile class of structural materials. Due to high specific strength, high specific stiffness, tailorability, and straightforward manufacturing, PMCs have applications in the aerospace, automotive, civil, and marine industries. Given the wide range of application, PMC structures are frequently exposed to complex mechanical and hygrothermal loadings throughout their lifetimes, making them susceptible to various forms of damage. Because of the incipient nature and inherent anisotropy of PMCs, in many instances, damage initiation and evolution is not well understood, and robust design and life prediction tools are often lacking. As a consequence, the inability to accurately predict damage and damage tolerance often results in over-conservative design practices, thereby considerably increasing costs and limiting application of PMC structures. Further experimental and analytical efforts are required to fully leverage the potential of PMCs and extend their applications. In this work, two studies are carried out to advance the understanding, analysis, and design of two types of PMCs with relevance in commercial and military aviation as well as future space exploration.

The first study focuses on a subset of PMCs called polyimide matrix composites. Because of their exceptional thermal performance, these composite structures are often used in applications where they are exposed to hot and humid environments and rapid rates of heating. The behavior of these laminated structures as a function of temperature, moisture content, and geometry is not well understood. In an effort to advance this understanding and provide basic design guidelines, chapters two and three of this work describe a study of blister-

ing and delamination, respectively, of moisture saturated graphite/polyimide composites.

The second study focuses on sandwich composite structures, which are easily manufactured and provide exceptional bending rigidity as compared to other skin-stiffened structures. Sandwich composite structures are susceptible to impact damage in their current applications in aviation and expected applications to next generation reusable launch vehicles. However, the performance of damaged sandwich composites is not well understood and demands further insight in order to extend and optimize their usage. In light of this, chapter four of this work describes experimental and numerical efforts aimed at assessing damage tolerance of sandwich composite structures with barely visible impact damage.

Conclusions describing the contributions and impact of these studies are provided at the end of each respective chapter.

CHAPTER 2

BLISTERING OF MOISTURE SATURATED GRAPHITE/POLYIMIDE COMPOSITES DUE TO RAPID HEATING*

*M.W. Czabaj, A.T. Zehnder, and K.C. Chuang. Blistering of Moisture Saturated Graphite/Polyimide Composites Due to Rapid Heating. *Journal of Composite Materials*, 43:153-174, 2009

2.1 Introduction

With an increased thermal resistance and high specific strength and stiffness, polyimide matrix composites (PiMCs) extend the role of composite materials into extreme temperature environments. Possible applications of PiMCs include next-generation space propulsion systems, rocket engine components, and advanced turbine blades [1, 2]. When compared to epoxy matrix composites, PiMCs are more expensive, and difficult to manufacture, and are thus likely to be used in applications where their high-temperature properties are truly needed and will be fully exploited. Thus, understanding how to model the high-temperature performance of these materials is critical to adopting them in real-world applications.

Among many issues surrounding PiMCs, delamination due to the rapid heat-up of moisture saturated laminates has emerged as a limiting factor on the allowable rates of heating [1]. When exposed to hot, high humidity environments, many PiMCs are capable of absorbing up to 1-1.5% moisture by weight. Moisture can be absorbed by the matrix or trapped inside voids or pre-existing flaws. As laminates heat up, the moisture will vaporize and develop high internal pressures. Such high pressures can lead to plasticization and hydrolysis of the matrix [3, 4], initiation of void nucleation, delamination of pre-existing flaws, and ultimately laminate failure [1, 3, 5].

To date, little effort has been given to the study of steam-induced damage, which can be explained by the fact that most composite materials still operate at or below aircraft-type temperatures in the neighborhood of 130 °C. At such temperatures, the relatively low vapor pressure of saturated steam is insufficient to

cause internal damage. However, due to the almost exponential dependence of saturation pressure on temperature, steam-induced damage can become significant in PiMCs used at high temperatures.

One of the few approaches for predicting steam-induced failure is proposed in the CMH-17 handbook [5]. There, for a predetermined material system and laminate thickness, test specimens are exposed to three different relative humidity (RH) levels, then heated at a desired mission time-temperature profile. When no damage is detected, the temperature range is increased. For a given initial moisture concentration, the temperature at which blistering is first detected determines the critical level of operation. Based on data from the three RH levels, a blister-temperature/initial-concentration envelope can then be constructed and used directly for damage prediction. However, since this method is restricted to the specific heating rate and geometry, it is somewhat limiting for design. A significant improvement upon the above method was proposed in the study by Rice *et al*. on AFR700B polyimide neat resin [3]. Rice *et al.* hypothesize that blistering of resin first occurs in the region of greatest moisture concentration, and hence the region of greatest steam pressure. In their study, a diffusion model was developed to predict moisture concentration within a resin sample up to the onset of blistering. The safety envelope is defined by testing specimens at different heating rates and saturation levels and overlaying their calculated 'drying paths' on a single plot of moisture versus temperature up to the point of blistering. This approach suggests that as long as maximum moisture concentration within a sample during the heat-up remains below this envelope, no blistering will be observed. This method is shown to successfully predict failure for several test cases; however, it cannot explain why, for very fast heating rates, samples tend to blister at much higher temperatures than what the theory pre-

dicts. The envelope may be dependent not only on the maximum concentration and geometry, but perhaps also on the rate of heating.

In recent work, Hui and Muralidharan developed a theory which allows for direct calculation of steam pressure inside a polymer with single or multiple micro-pores [6,7] and composites with crack-like cavities [8,9]. Assuming that the polymer/composite initially has no internal damage and void nucleation has not yet initiated, one can greatly simplify this theory and express the steam pressure within a material as

$$P(\underline{x},t) = P_{sat}(T(\underline{x},t))\frac{\psi(\underline{x},t)}{\psi_{max}}, \tag{2.1}$$

where $\underline{x}$ is position, T is temperature, P_{sat} is the saturation pressure of water at temperature T, ψ is the moisture concentration calculated by solving the nonlinear diffusion equation, and ψ_{max} is the maximum possible moisture concentration of the material.

In this study, we further extend the approach proposed by Rice. With the theory developed by Hui and Muralidharan we define steam-induced damage in terms of the critical pressure-temperature envelope. To better understand blister formation, experiments are performed on HFPE-II-52 polyimide neat resin (NR), as well as T650-35/HFPE-II-52 graphite/polyimide (Gr/Pi) laminates [10]. These experiments are performed by measuring the expansion of moisture-saturated samples at various heating rates in a thermal mechanical analyzer (TMA), which measures transverse thermal expansion. Departures of the hygrothermal expansion curve from the curve due solely to thermal expansion indicate the initiation of void growth. For each sample, a set of nonlinear moisture/temperature diffusion equations were solved numerically and the critical steam pressure at void initiation was calculated using Equation (2.1). Based

on a series of tests, a blister pressure-temperature envelope is obtained, clearly showing its dependence on initial moisture concentration and heating rate.

In what follows, the general theory and boundary conditions (specific to the TMA) used in the calculation of Equation (2.1) are presented. These descriptions are followed by a discussion of specimen preparation and methods for obtaining thermal/moisture diffusion properties for both materials. We then present results from the exploratory tests, which we use to validate our test methods and to define the onset of steam-induced damage. Finally, a pressure-temperature envelope is shown, along with a discussion on its applicability to design and life prediction.

2.2 Theory

To solve Equation (2.1) a set of non-linear moisture/temperature diffusion equations must be solved. Due to the test specimen shape (described in next section), the thermal and moisture diffusion are assumed to be fully three dimensional. The specimen is modeled as a rectangular prism with orthotropic thermal/moisture diffusion properties for Gr/Pi, and isotropic properties for NR. Due to the symmetry of the problem, only one-eighth of the specimen is modeled, as shown in Figure 2.1. It is assumed that all specimens are initially at temperature T_0 and have a moisture concentration of ψ_0. Specimens are heated by natural convection of air inside the TMA testing chamber. The air temperature is given by

$$T_{\text{inf}}(t) = T_0 + \dot{T}t, \qquad 0 \leq t \leq t_f, \tag{2.2}$$

where $\dot{T}$ is the heating rate. It is also assumed that moisture from the specimen diffuses into the testing chamber, which is assumed to be at zero relative humidity. The effect of volatiles released by the material during heat-up are neglected in the calculation of internal pressure. This assumption will be justified by results of the TGA/FTIR study.

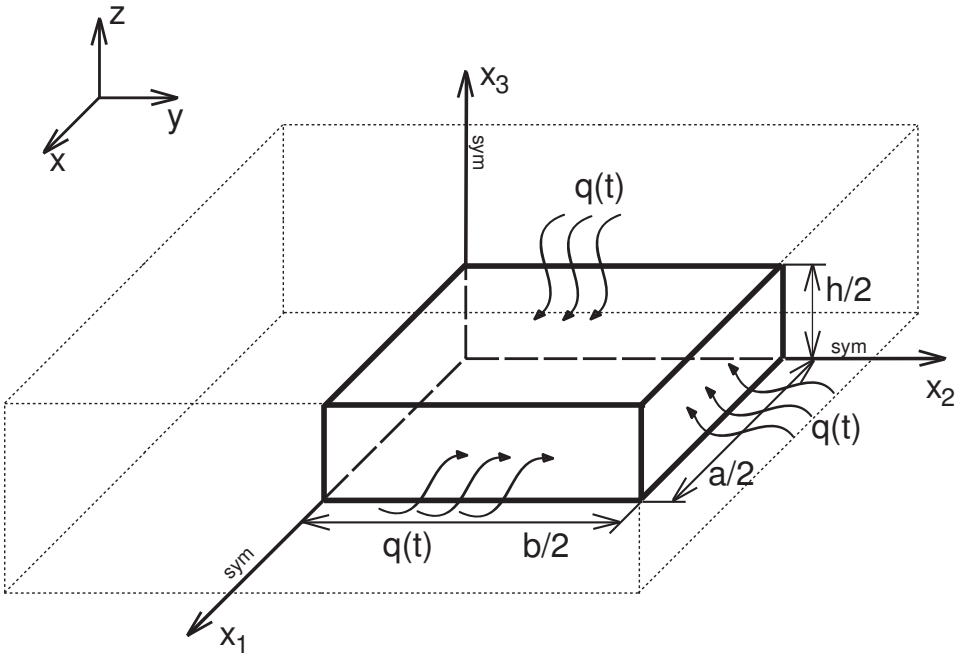

Figure 2.1: 3-D sketch of the specimen geometry.

For most polymer matrix composites, thermal equilibrium is achieved much faster than moisture equilibrium. The governing equations for heat and moisture transfer within a laminate sample are given by

$$\frac{\partial T}{\partial t} = C_{11}\frac{\partial^2 T}{\partial x_1^2} + C_{22}\frac{\partial^2 T}{\partial x_2^2} + C_{33}\frac{\partial^2 T}{\partial x_3^2}, \tag{2.3}$$

$$\frac{\partial \psi}{\partial t} = D_{11}(T(\underline{x},t))\frac{\partial^2 \psi}{\partial x_1^2} + D_{22}(T(\underline{x},t))\frac{\partial^2 \psi}{\partial x_2^2} + D_{33}(T(\underline{x},t))\frac{\partial^2 \psi}{\partial x_3^2}, \tag{2.4}$$

where T is the temperature, ψ is the moisture concentration, C_{11} and C_{22} are the in-plane thermal diffusivities, C_{33} is the out-of-plane thermal diffusivity and D_{ii}

represent the temperature-dependent moisture diffusivities. For the NR, Equations (2.4) and (2.3) reduce to the isotropic case where $C_{11} = C_{22} = C_{33} = C$ and $D_{11} = D_{22} = D_{33} = D(T)$, where

$$D(T) = D_0 e^{\left(\frac{-E_a}{RT}\right)}. \tag{2.5}$$

In Equation (2.5), D_0 is the pre-exponential factor, E_a is the activation energy, and R is the universal gas constant. Note the 1-way coupling in Equations (2.3) and (2.4), where moisture diffusivity depends on the material temperature.

Based on the temperature and humidity conditions within the TMA during a test, the convective boundary condition is given by

$$q(\underline{x}, t) = h(T_{surf}(\underline{x}, t) - T_{inf}(t)), \tag{2.6}$$

where q is the heat flux per area, h is the convection coefficient, T_{surf} is the surface temperature of the specimen, and T_{inf} is defined by Equation (2.2). The moisture concentration on the boundary is

$$\psi(t) = 0. \tag{2.7}$$

Equations (2.3) and (2.4) are integrated using an implicit, backward Euler, finite-difference (FD) scheme [11,12]. For each time step, the temperature distribution is calculated and used in Equation (2.5) to obtain the diffusivity for each grid point. Finally, the concentration and steam pressure are computed.

2.3 Experiments

2.3.1 Specimen Preparation

The polyimide NR sample was manufactured in a hot press by compression molding of the HFPE-II-52 powder in a 127×127×3 mm steel mold at a maximum temperature of 371 °C and 17.42 MPa part pressure. The sample was demolded, postcured in a vacuum oven at 371 °C for 16 hours, and cooled down to room temperature at 0.75 °C/min. The sample was finally cut into 4×4×3 mm specimens with a diamond wire saw. More specific details on resin synthesis, cure cycle, and molding procedure can be found in [10, 13–15].

The Gr/Pi laminate was manufactured using 4 plies of T650-35/HFPE-II-52, 8-harness satin weave, UC309 epoxy sizing, fabric prepreg. The laminate was cured in a 304×304 mm mold at a maximum temperature of 371 °C, 3.48 MPa part pressure, and 50 cm Hg vacuum. To prevent laminate warping and blistering caused by outgassing resin, the laminate was postcured in the hot press under 0.2 MPa part pressure for 16 hours, cooled down to room temperature at a rate of 0.75 °C/min, and then demolded. Based on results presented in [16], the exposure of epoxy sizing to 371 °C during cure and post-cure (approximately 20 hours) should cause complete decomposition of the sizing. The resulting laminate had an average thickness of 1.47 mm. To evaluate the quality of the cure, the laminate was ultrasonically inspected for areas of large porosity, surface flaws, and dry spots. The higher quality regions were further examined using resin digestion to access the void content (see Table 3.1). Specimens with dimensions of 10×10×1.47 mm were cut using a diamond wire saw.

Both NR and Gr/Pi specimens were saturated to different moisture contents corresponding to five different RH levels, as shown in Figure 2.2. Saturation was performed in a temperature-humidity chamber at 70 °C. Prior to saturation, all specimens were vacuum dried for 4 days at a temperature of 70 °C. The maximum moisture content for each system was obtained by soaking specimens in distilled water at a temperature of 70 °C, for up to 3 days.

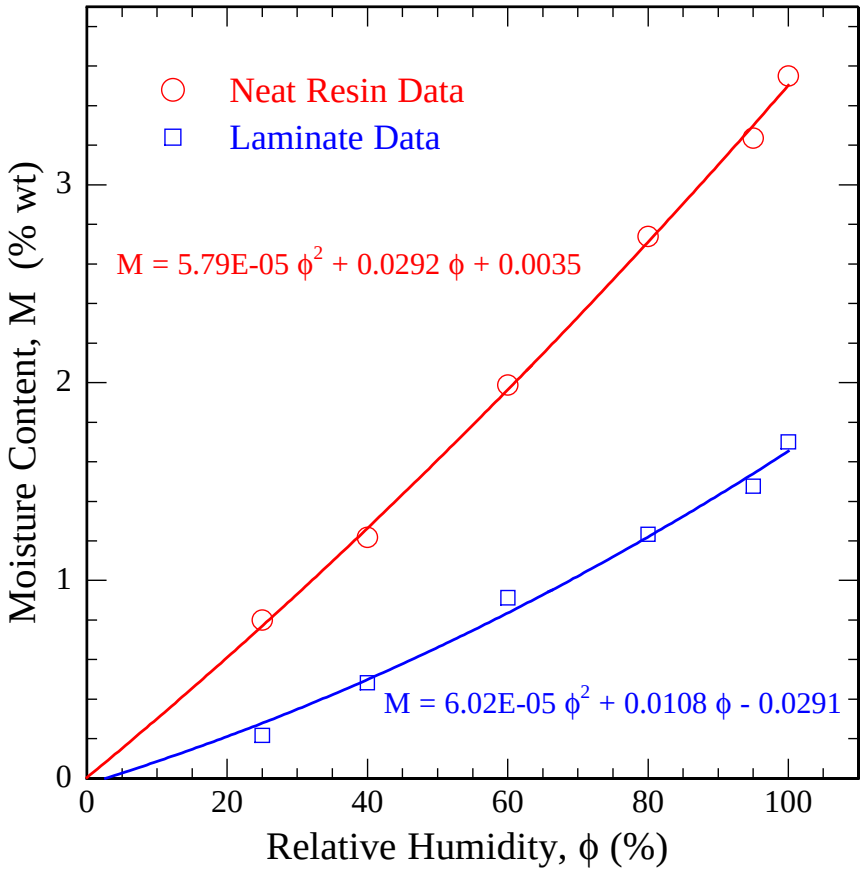

Figure 2.2: Equilibrium moisture content versus relative humidity - data and polynomial fit.

The relationship between moisture concentration, ψ used in Equations 2.1 and 2.4, and moisture content, M used in Figures 2.2 and 2.3 is given in [17]. In

general, M is defined as

$$M = \frac{m}{W_d} \times 100, \tag{2.8}$$

where m is the total weight of moisture in the material and W_d is the weight of dry material. Weight of moisture in the material is defined as

$$m = g \int_V \psi(\underline{x}, t) dV, \tag{2.9}$$

where g is the gravitational acceleration and V is the material volume.

2.3.2 Material Properties

The heat and moisture diffusion properties of polyimide NR and Gr/Pi laminate are presented in Tables 2.1 and 3.1. For polyimide, the density and thermal diffusivity values were taken from [18]. Moisture diffusivity was obtained experimentally [13] using weight gain (20-70°C) and weight loss (70-300 °C) tests, and is expressed as a function of temperature by Equation (2.5).

For the Gr/Pi laminate, the fiber volume fraction, resin volume fraction, and void content were measured using resin digestion [19]. The laminate density and specific heat were estimated using the rule of mixtures. Based on conductivity of resin and fibers, the in-plane and out-of-plane thermal conductivities for the laminate were calculated using the procedure outlined in [17]. Here, the 4 plies of woven fabric are approximated as a $[0/90]_4$ laminate. The 3-D temperature-dependent moisture diffusion properties could not be readily obtained without an extensive experimental study such as described in [13]. Instead, the laminated diffusivity is assumed to follow the Arrhenius equation [17], scaling with the diffusivity of the neat resin. With this assumption, we

measured the laminate diffusivity at a temperature of 70 °C and RH of 95%, and compared it to the diffusivity of NR at that temperature and RH to determine the scaling parameter. Assuming that this scaling does not change dramatically over the range of considered temperatures, the laminate diffusivity as a function of temperature is determined.

For the laminate diffusivity measured at 70 °C, an estimation of in-plane (3-direction) and out-of-plane (1,2-direction) moisture diffusivity was performed using a weight gain experiment (Figure 2.3). The out-of-plane diffusivity was obtained as suggested in [17] by measuring the weight gain of samples having a width-to-thickness ratio of 100:1, enforcing a 1-D, through-thickness diffusion. The out-of-plane diffusivity is calculated from the initial slope of the weight gain data.

The in-plane diffusivity is obtained by recording the weight gain of specimens with dimensions that enforce 3-D diffusion. For this measurement, a width-to-thickness ratio of 10:1 was used. It is assumed here that the in-plane diffusivities, D_{11} and D_{22} are equal, and are scalar multiples of the out-of-plane diffusivity [12], D_{33}. The scalar multiple is defined here as η. Using this fact, Equation (2.4) can be reduced to the isotropic case with $D = D_{33}$ and η^2 scaling the in-plane dimensions. The new equation can then be solved using a FD scheme while iterating η to match the numerical solution to the 3-D experimental weight gain data.

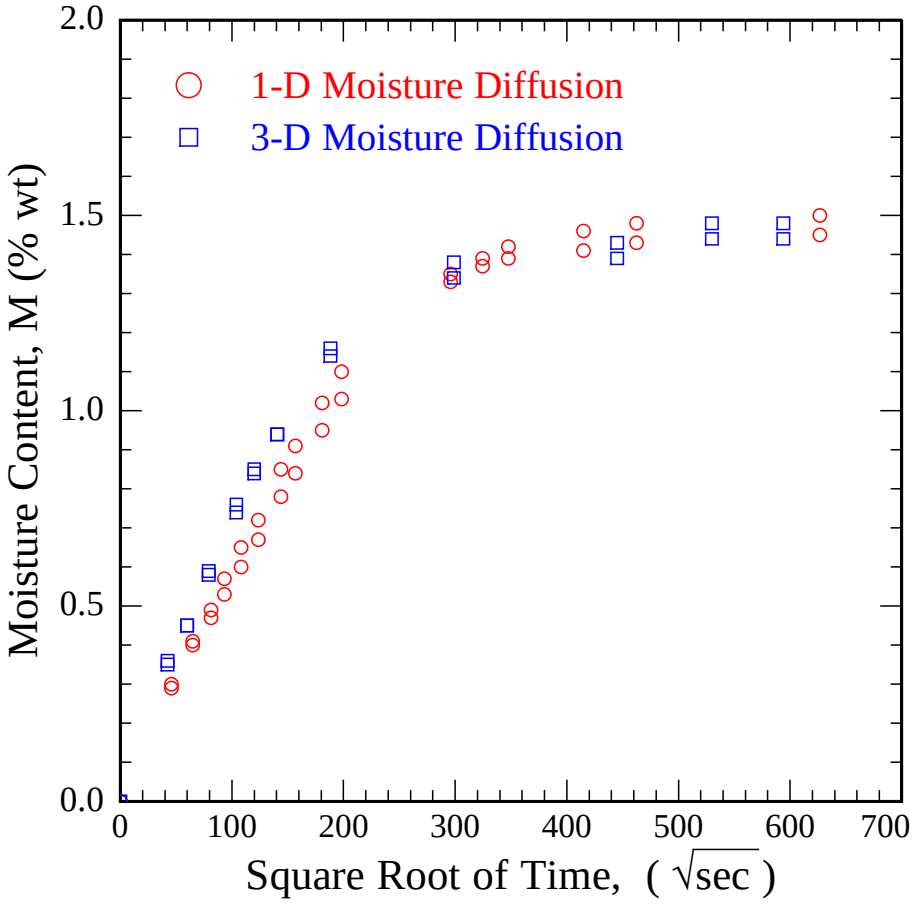

Figure 2.3: Weight gain data - Gr/Pi (70 °C, 95% RH). 1-D moisture diffusion obtained from specimens with aspect ratio of 100:1. 3-D moisture diffusion obtained from specimens with aspect ratio of 10:1.

2.3.3 TGA-FTIR Measurements

The theory presented in equation 2.1 assumes that the only source of blistering/delamination pressure is water vapor. To validate this assumption, the thermogravimetric analysis (TGA) and Fourier transform infrared spectroscopy (FTIR) measurements were performed on dry and moisture saturated neat resin and laminate samples. These measurements provide the total weight loss as

Table 2.1: Neat resin - material properties

Resin Density, ρ_r (g/mm^3)	0.00142
Pre-exponential Factor, D_0 (mm^2/s)	9
Activation Energy, E_a (g mm^2/mol s^2)	3.7x10^{13}
Thermal Diffusivity, C (mm^2/s)	0.16
Maximum Moisture Content, M$_{max}$ (% wt)	3.55
Glass Transition Temperature, T_g (°C)	351

Table 2.2: Gr/Pi laminate - material properties

Fiber Volume Fraction, V_f (%)	56.12
Resin Volume Fraction, V_r (%)	42.01
Void Content, V_v (%)	1.87
Laminate Density, ρ_l (g/mm^3)	0.00159
Pre-Exponential Factor, 1,2-direction, $D_{0_{11}} = D_{0_{22}}$ (mm^2/s)	7.97
Pre-Exponential Factor, 3-direction, $D_{0_{33}}$ (mm^2/s)	2.85
Activation Energy, E_a (g mm^2/mol s^2)	3.7x10^{13}
Thermal Diffusivity, 1,2-direction, $C_{11} = C_{22}$ (mm^2/s)	2.38
Thermal Diffusivity, 3-direction, C_{33} (mm^2/s)	0.56
Maximum Moisture Content, M$_{max}$ (% wt)	1.70

a function of temperature and identify the gasses emitted from the samples as they are heated.

The TGA measurements were conducted NASA Glenn Research Center using Thermo Electron Model 2950, and FTIR measurements were conducted us-

ing Thermo Electron Model 270. The TGA-FTIR measurements were conducted on dry and moisture saturated (95% RH) NR and Gr/Pi samples. The specimen size was 5×5×3 mm for NR, and 5×5×1.47 mm for Gr/Pi. All tests were performed in a nitrogen environment. All TGA tests were run from room temperature to 405 °C at a rate of 10 °C/s. The FTIR data was collected at temperatures of 43, 133, and 405 °C. A summary of results from TGA-FTIR measurements is presented in the results section.

2.3.4 Experimental Setup and Data Reduction

All experimental tests in this study were performed using the TA Instruments Q400 Thermomechanical Analyzer shown in Figure 2.4a. The TMA provides temperatures of -150 to 1000 °C and heating rates up to 3.3 °C/s. In the TMA, the specimen is placed on a circular quartz base (15 mm dia.) and its expansion is measured using a 2 mm diameter quartz probe. During the test, the probe is lowered onto the top surface of the specimen (Figure 2.4a-b) and a force of 0.02 N is applied to the specimen to establish contact and to prevent shifting during the test. The heating chamber is lowered onto the base and heat-up is controlled by a thermocouple that measures air temperature in the vicinity of the specimen. An example of TMA data (NR - M_0=3.23% wt. and $\dot{T}$=1.5 °C/s) is presented in Figures 2.5a-b. Figure 2.5a shows the time-varying air temperature inside the TMA test chamber during a temperature ramp, and Figure 2.5b shows the resulting vertical strain, ϵ, of the specimen as a function of air temperature. The transverse strain is defined as the ratio of extension measured by the quartz probe to initial specimen thickness.

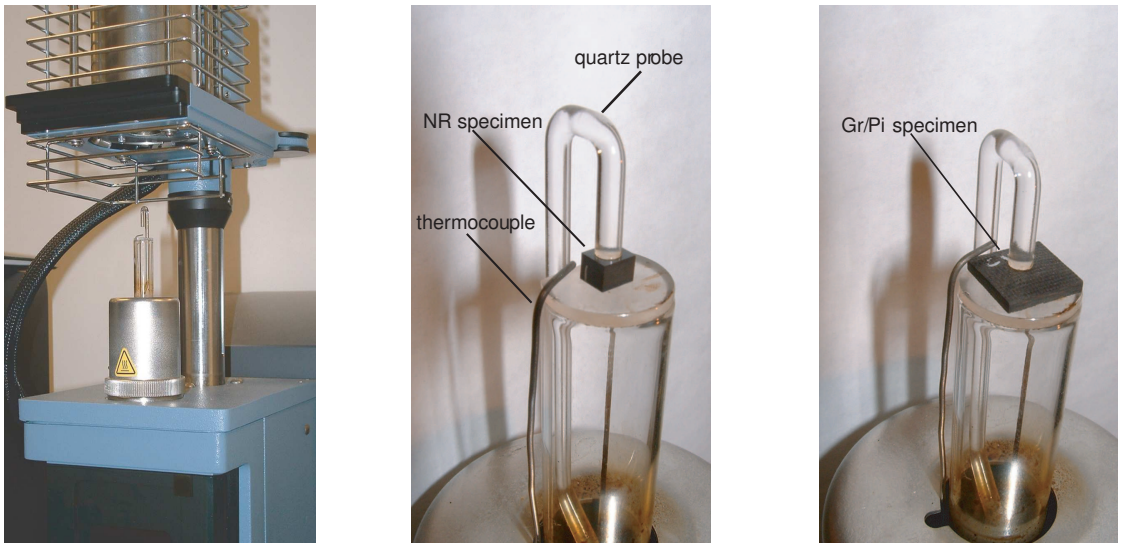

(a) Q400 TMA (b) NR specimen (c) Gr/Pi specimen

Figure 2.4: TMA test chamber and test specimens.

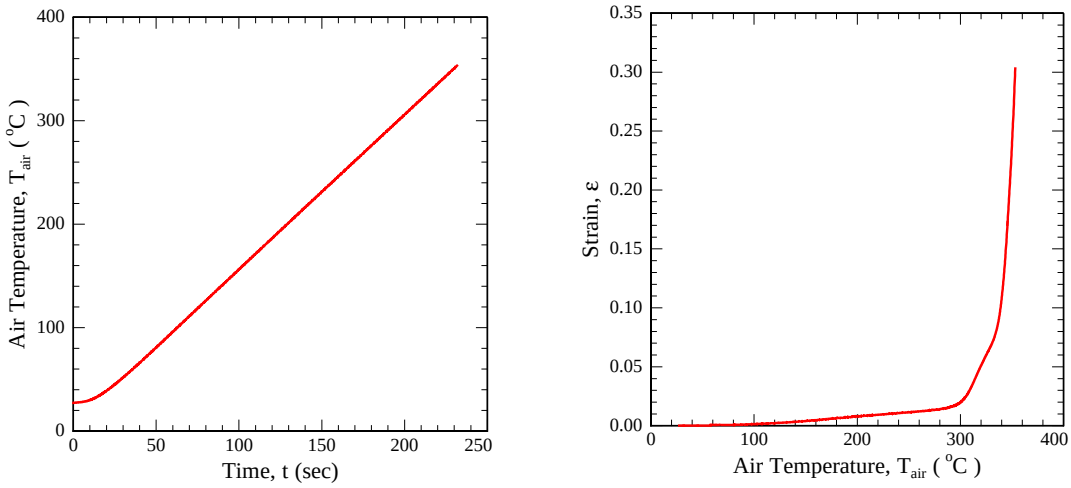

(a) Air temperature ramp (b) Specimen's transverse strain

Figure 2.5: TMA test data - neat resin ($\dot{T}$ = 1.5 °C/s).

Given the air temperature and strain data, the objective is to compute the maximum internal steam pressure up to the onset of blistering. Here, the air temperature profile obtained from the TMA is substituted into Equation (2.6)

and used to compute the temperature and moisture concentration distribution within the specimen using Equations (2.3) and (2.4). In order to apply the convection boundary condition Equation (2.6), a calibration was performed to estimate the convection coefficient, h. For each material, a 10×10 mm specimen was embedded with a 0.8 mm K-type thermocouple, such that the bead was located in the center of the specimen. The thermocouple was fixed in place with M-Bond 610 high-temperature epoxy adhesive. Each specimen was then placed inside the TMA chamber and tested at three different heating rates up to a temperature of 380 °C. Using the air temperature data from the TMA in Equation (2.6), a FD scheme was used to iterate on h until the numerical output matched the data collected by the embedded thermocouple. For each material, the convection coefficient did not change with increasing temperature, but increased linearly with the heating rate. The approximate expression for the convection coefficient is given by

$$h = 0.4\dot{T} + 0.42, \tag{2.10}$$

where $\dot{T}$ has units of °C/s and h has units of W/m^2°C.

With the temperature and moisture-concentration fields, the internal steam pressure is computed using Equation (2.1). The final step is to determine which point on the strain-temperature curve corresponds to onset of blistering and what are the corresponding critical blister pressure, P_{blist} and blister temperature, T_{blist}. The method for identifying the onset of blistering for a given strain-temperature profile is addressed in the results section.

2.4 Results

2.4.1 Exploratory Tests

The first set of experiments was performed to explore the general trends in the data obtained at different heating rates. For these tests the specimens were saturated at 95% RH, corresponding to moisture content of 3.23% wt. for NR and 1.47% wt. for Gr/Pi. Each material was tested at heating rates ranging from 0.166 °C/s to 2.5 °C/s. At four of the heating rates (0.5, 1.0, 1.5, 2.0 °C/s) four specimens were tested per rate to ensure repeatability of the experiments. Figures 2.6a-b show sample neat resin and laminate strain-temperature data in cases where steam-induced damage was observed. In each figure, strain is plotted against the calculated temperature in the center of the specimen, T_c. The thermal strain of a dry specimen (dashed line) is shown for comparison.

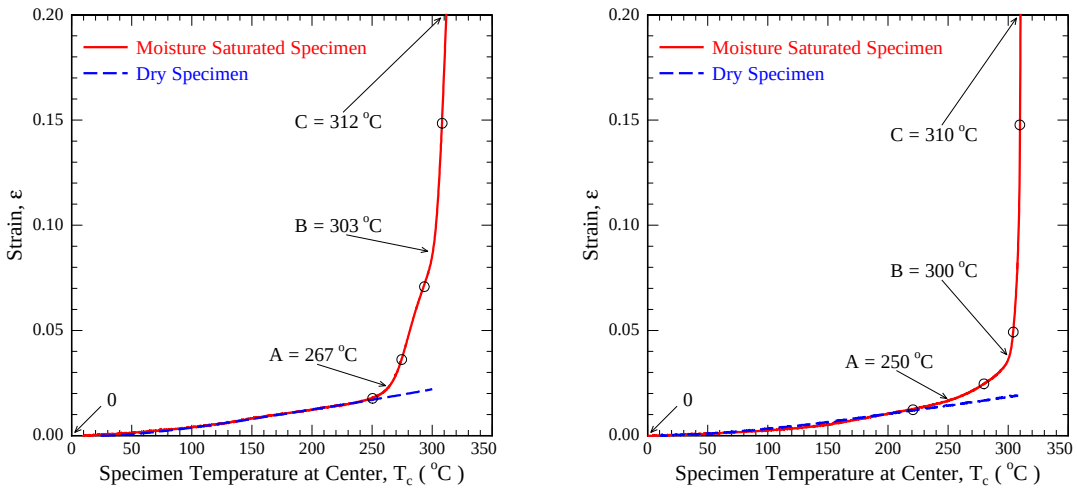

(a) Neat resin

(b) Graphite/polyimide

Figure 2.6: Strain versus temperature response ($\dot{T}$ = 1.5 °C/s). The circular marks indicate approximate termination of the RQ tests.

After examining the initial set of data for each material, we observed a distinct transition between heating rates for which specimens developed damage and heating rates for which specimens simply dried out. For the NR specimens that developed damage, the strain initially followed the thermal expansion curve, but then deviated from that curve with a sudden change in strain at two distinct points A and B (Figure 2.6a). The Gr/Pi specimens also initially followed the thermal expansion curve; however, the departure from this curve (point A) during the test was not as distinct. For the Gr/Pi specimens that developed damage, the only distinct change in strain occurred at point B (Figure 2.6b). For both materials, the very sharp increase in strain from points B to C leads to extensive blistering (NR) and delamination (Gr/Pi) of specimens.

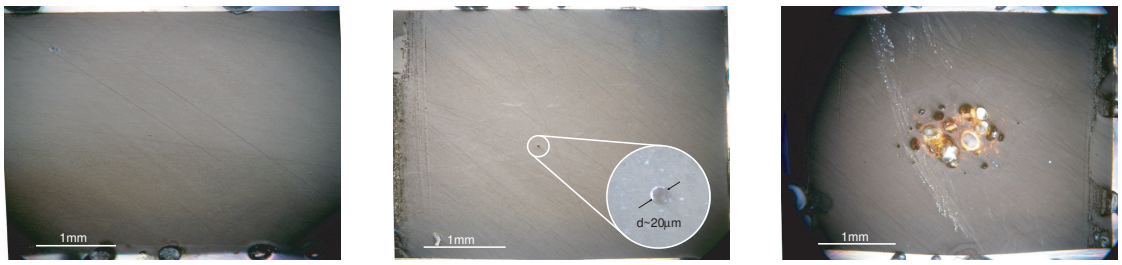

(a) $T_c \simeq 250, 280°C$ (b) $T_c \simeq 295°C$ (c) $T_c \simeq 315°C$

Figure 2.7: Microscopy - neat resin ($\dot{T}$ = 1.5 °C/s).

The next set of experiments was intended to directly investigate the state and progression of damage within specimens during temperature ramps. To ensure that sufficient moisture was available to cause steam-induced damage, all specimens were saturated at 95% RH and tested at a rate of 1.5 °C/s. In these tests, instead of performing a full temperature ramp to point C, (Figure 2.6a), each new test was stopped at a different location along the strain-temperature curve. Termination of each test is indicated by the circular marks in Figures 2.6a-b. Upon reaching the desired temperature each specimen was quickly re-

moved from the TMA and quenched in water to prevent further void growth. All specimens were then cut into equal halves and polished. The void content and blistering are recorded after examination with an optical microscope (Figure 2.7, 2.8). We will refer to this type of test as a ramp-quench (RQ) test in all subsequent sections of this paper. The RQ test is designed to, as much as possible, freeze in the state of damage at a particular temperature.

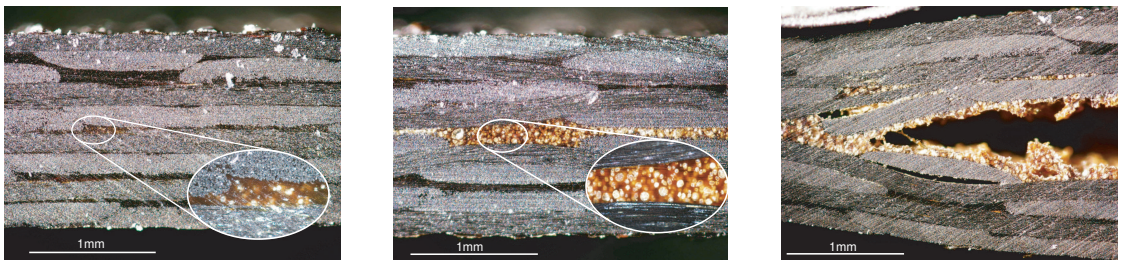

(a) $T_c \simeq 290°C$ (b) $T_c \simeq 305°C$ (c) $T_c \simeq 310°C$

Figure 2.8: Microscopy - graphite/polyimide ($\dot{T}$ = 1.5 °C/s).

From the RQ tests of NR, the micrographs revealed no visible damage in the specimens tested at temperatures just above and below point A ($T_c \simeq 250$, 275 °C). At 50X magnification the surface quality was identical to the surface of an untested specimen (Figure 2.7a). In the specimen tested to temperature below point B ($T_c \simeq 290$ °C), a single spherical void with diameter of ~20 μm was detected, located approximately in the center of the specimen (Figure 2.7b). A specimen quenched at a temperature above point B ($T_c \simeq 315$ °C) revealed a coalescence of several spherical voids (diameter ≃ 50-250 μm) into a large damage zone of approximately 1.25 mm in diameter (Figure 2.7c). Based on these results, we can conclude that void nucleation begins at around point A in Figure 2.6a. Following nucleation, the few initial voids slowly grow in size, resulting in the steady change in strain between points A and B. Beyond point B, additional voids nucleate away from the specimen's center, and begin to coalesce into a

network of voids. This coalescence weakens the material to the point where void growth becomes unstable, resulting in a rapid increase in strain between points B and C.

The RQ tests of the Gr/Pi revealed no damage in the matrix or in the fibers for a specimen tested to a temperature below point A ($T_c \simeq 220$ °C). However, a specimen tested to a temperature below point B ($T_c \simeq 280$ °C) revealed the presence of several spherical voids in the pocket of resin between the midplane layers of the laminate (Figure 2.8a). These voids were approximately 5-20 μm in diameter. In the specimen tested to temperature above point B ($T_c \simeq 305$ °C) the resin between the midplane plies was entirely filled with voids, and some void formation was observed in the resin above and below the midplane. Interestingly, this significant void formation appears only as a very subtle change in strain between points A and B, possibly due to the stiff carbon fibers shielding the strain resulting from the evolving voids. As described previously, the TMA detects void formation by measuring the deformation of the top surface of the specimen. For this formation to be detected, the expanding voids in the midplane must apply enough pressure on the surrounding fibers to overcome their stiffness and cause deformation. As the pressure increases, the continuous coalescence of voids weakens the bond between the midplane plies until the specimen delaminates. The delamination of the specimen is clearly seen in Figure 2.8c and is represented by the large increase in strain between points B and C in Figure 2.6b.

To substantiate the above results, we performed another set of experiments. In these experiments, we determine if it is possible to nucleate voids at temperatures below point A of NR data (Figure 2.6a). These experiments are di-

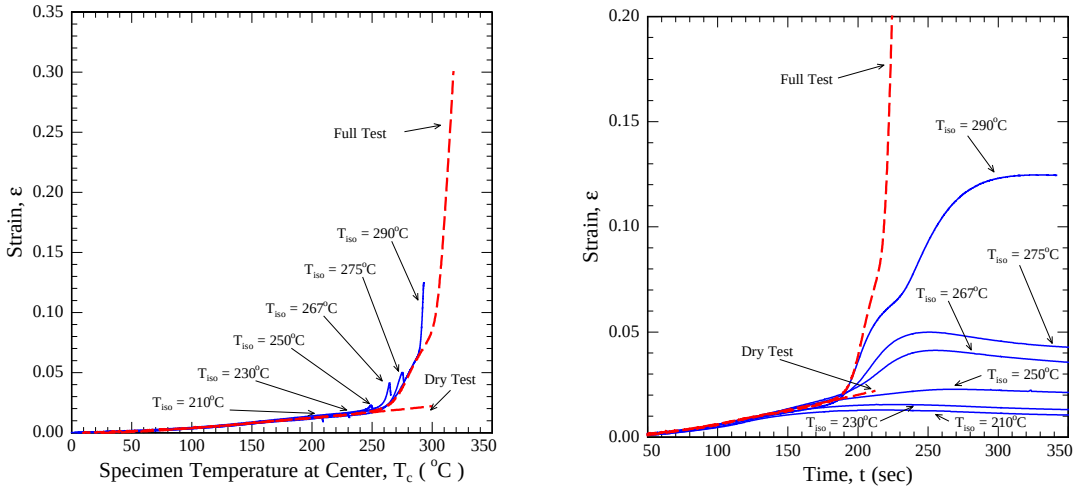

(a) Strain vs temperature at center

(b) Strain vs time

Figure 2.9: Ramp-isothermal test - neat resin ($\dot{T}$ = 1.5 °C/s).

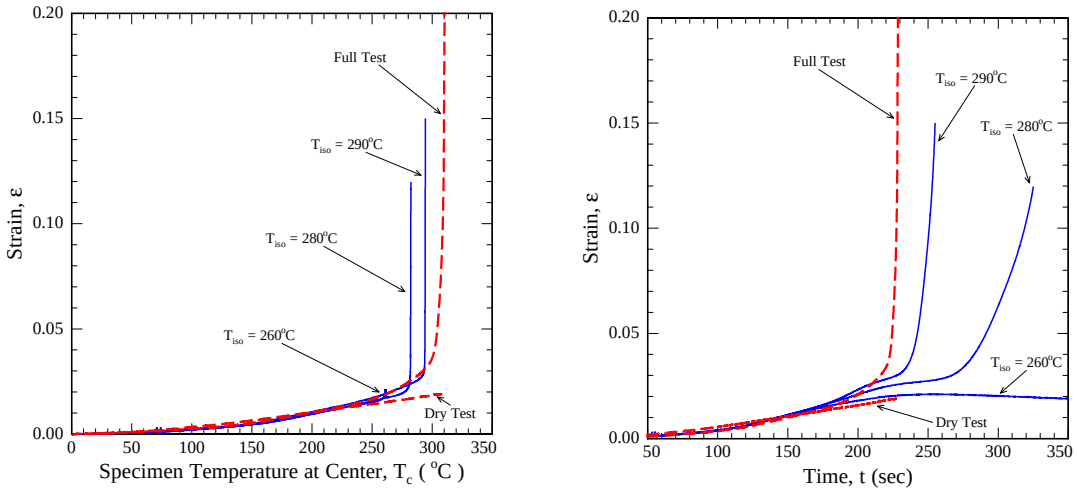

(a) Strain vs temperature at center

(b) Strain vs time

Figure 2.10: Ramp-isothermal test - graphite/polyimide ($\dot{T}$ = 1.5 °C/s).

rectly motivated by the time dependent response of HFPE-II-52 resin at high temperatures [20]. For specimens tested at high heating rates to point A, numerical calculations of the moisture content show that the available moisture

in the center of the specimen is typically near 100% of the maximum moisture content. Equation (2.1) shows that this result corresponds to an exponential increase in the internal steam pressure. We investigate whether the high rate of pressure build-up results in a stiffer material response, resulting in the suppression of void nucleation below point A in constant heating rate tests. To explore this potential phenomenon, we performed a series of ramp-isothermal (RI) tests. Here, in contrast to the RQ tests, the air temperature inside of the TMA is held constant for several minutes upon reaching the desired location on the strain-temperature curve. Holding the temperature constant forces the pressure to remain constant or decrease. This sudden drop in the rate of loading will result in a lower strain rate and cause softer response of the material, and perhaps void nucleation prior to point A.

The results of the RI tests for NR ($\dot{T}$ = 1.5 °C/s) are presented in Figures 2.9a-b. Figure 2.9a plots the specimen's strain as a function of the calculated temperature in the specimen's center, and Figure 2.9b plots strain as a function of time. In the first three tests, the specimens were equilibrated at temperatures below point A, at T_{iso} = 210, 230, and 250 °C. In each test, the strain follows the thermal expansion curve up to point A and then the strain remains constant or decreases. The microscopy of these specimens revealed no visible damage anywhere in the cross-section. These results imply that for temperatures below point A, there is no damage from void initiation and growth. For each test, the magnitude of pressure was not enough to overcome the resin stiffness and cause void formation. To confirm that point A is the threshold for void nucleation, we repeated the isothermal tests for three temperatures, in between points A and B (T_{iso} = 267, 275, 290 °C). For all three, beyond point A there is a clear departure from the thermal expansion curve. In contrast to the full-ramp test, the increase

in strain is stable. In the first two tests, the strain reaches a peak value and then begins to decay. In the last tests the strain reaches a plateau then remains constant with time. In the specimens held at 267 and 275 °C, microscopy revealed voids of 5-20 μm in diameter scattered across the cross-section of the specimen. The microscopy of the last specimen (T_{iso} = 290 °C) showed damage similar to that seen in Figure 2.7, but on a smaller scale. Based on these last three tests, we can conclude that for temperature immediately above point A, voids can nucleate and grow; however, the available steam pressure is insufficient to cause an unstable growth. Additionally, the strain decay observed in two of the tests may suggest that the material retains enough of its stiffness so that as pressure decreases the voids begin to collapse. For the test closest to point B (T_{iso} = 290 °C), the magnitude of the available steam pressure, combined with the decrease in the resin's stiffness and coalescence of voids results in an increased instability. From this we conclude that the region between points A and B is where void growth transitions from stable to unstable.

The RI tests for the Gr/Pi (Figure 2.10a-b) revealed similar results to the neat resin. For the test where temperature was held below point A of NR (T_{iso} = 260 °C), the strain remained on the thermal expansion curve and microscopy showed no damage in either the matrix or the fibers. As before, prior to A the available steam pressure was not enough to cause nucleation of voids in the resin. In the next two tests, which were held at temperatures between points A and B (T_{iso} = 280, 290 °C) we see a more dramatic change in the specimen's response. For the first of the two tests, the strain beyond point A initially stabilized to an approximately constant value, but then it began to increase in an unstable manner. The last test was similar, but the strain remained constant for a much shorter time period before it rapidly increased. The rapid increase in

strain for both tests is a result of delamination.

Given all of the above results, we propose a method for predicting the onset of steam-induced blistering of Gr/Pi laminates. Based on microscopy of tested Gr/Pi laminates we conclude that for all blistered/delaminated specimens, the damage always initiated in the resin, and not in the fibers or the voids. We also determined that the presence of carbon fibers around the sites of void nucleation prevented the TMA from accurately detecting the initiation of damage. The only distinct evidence of damage evolution measured by the TMA was the point of the specimen's delamination. Without prior knowledge of the thermal expansion curve for each individual specimen, it is unlikely that initiation of steam-induced damage in laminates can be accurately determined from this type of test. In contrast to the Gr/Pi tests, in TMA tests of the NR specimens, void nucleation coincides with the point of divergence of the hygrothermal expansion curve from the thermal expansion curve. When testing NR with the TMA, this divergence appears clearly on the strain-temperature curve, and is represented by the first distinct change in its slope. Prior knowledge of the thermal expansion curve is therefore unnecessary for this type of test. These results suggest that since damage in the laminates initiates and evolves in the resin, the NR tests will produce the most accurate lower bound of the damage threshold.

2.4.2 Onset of Blistering - Definition

Having decided to use the NR tests to predict the onset of blistering, we require a consistent method for locating point A on the strain-temperature curve. To find point A, we perform a linear fit to the data on each side of this point.

For example, using Figure 2.11, we fit a straight line between points O and A, and between point A and B. We locate the points where the experimental data diverges from each of the straight lines, and define these points T_{min} and T_{max}. Assuming that the voids nucleate somewhere between these two points, we define the temperature at the onset of blistering, T_{blist} as the average of T_{min} and T_{max}. Alternatively, to get a more conservative estimate one could use the T_{min} value.

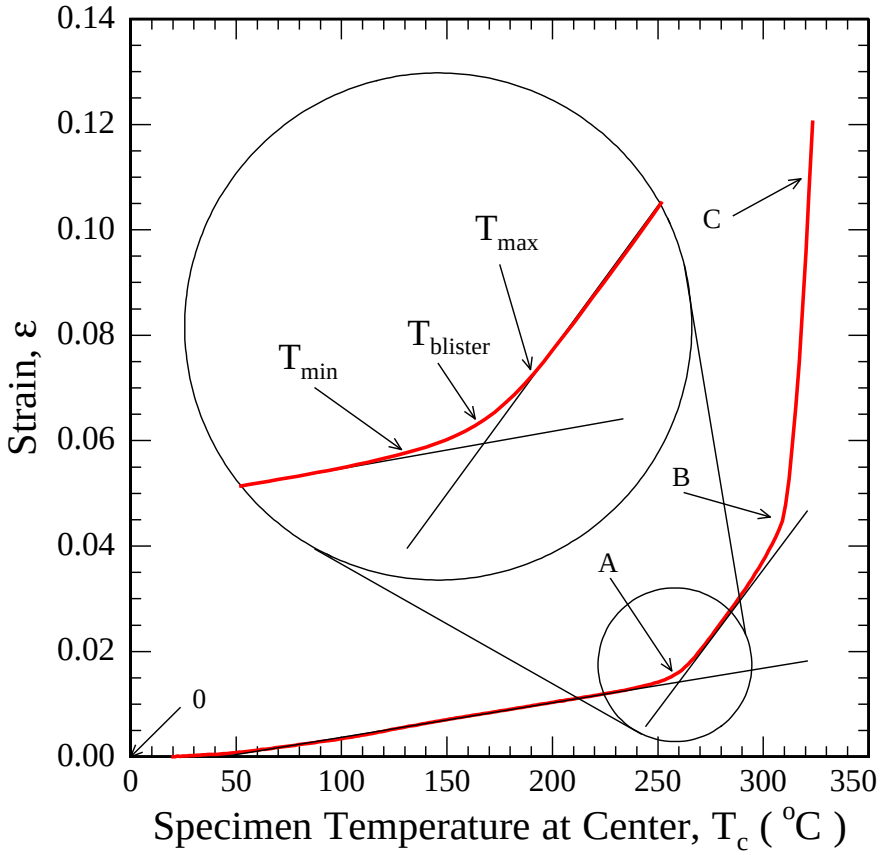

Figure 2.11: Onset of blistering - definition.

2.4.3 Pressure-Temperature Envelope

The final step in this study was to test NR specimens over a range of moisture content levels. The heating rate for which blistering was no longer observed was determined for each saturation level. Above this rate the effect of heating rate on blistering temperature was determined. With this data a critical pressure/temperature envelope for blistering is constructed.

All specimens were tested over a range of heating rates starting with 2.5 °C/s down to rates below which blistering was no longer observed. Two specimens were tested per rate. Tests were repeated at five moisture content levels obtained at 20, 40, 60, 80, 95% RH. Each tested specimen was cut into equal halves and examined under a microscope for damage. The data for specimens saturated at 20% RH is not presented. At this saturation level, for all heating rates, blistering was observed only above the glass transition temperature of the resin.

For all blistered specimens, the onset of damage was determined based on point A, and used to determine the corresponding blister pressure and temperature. The reduced data are presented in Figure 2.12. In this figure, the solid line represents the saturation pressure of steam as a function of temperature. Based on Equation (2.1), the calculated blister pressure for all specimens must always fall on or below this line. Data obtained for each moisture content are marked using distinct symbols. To show how the increase in heating rate changes the onset of blistering, several heating rates are marked on the leftmost set of points. The solid symbols represent rates below which no blistering was observed. The dashed line connecting the solid symbols represents the threshold for blistering.

Examining Figure 2.12 several trends are observed. At each moisture satu-

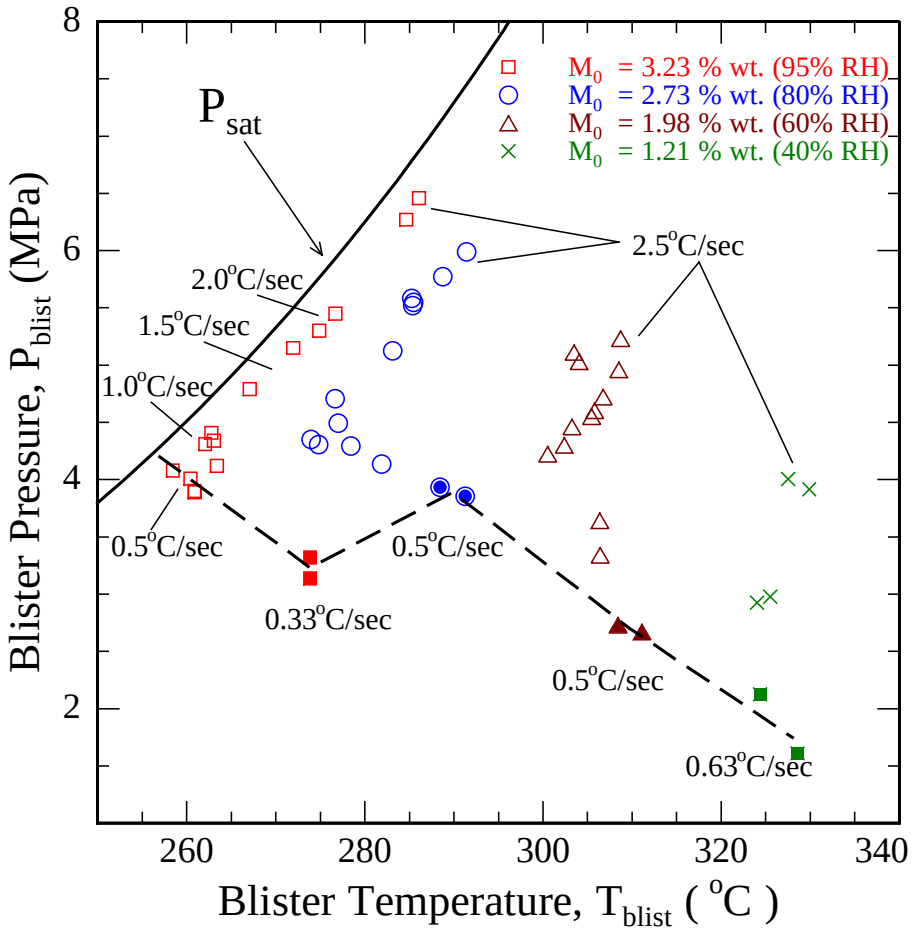

Figure 2.12: Critical pressure-temperature envelope: neat resin.

ration level there is a heating rate below which blistering never occurs. In such cases the sample is able to dry without incurring hight vapor pressures that lead to blistering. As the initial moisture saturation level increases the blistering temperatures decreases while the minimum safe blister pressure decreases. This is to be expected since at higher temperatures the material is softer and thus able to sustain lower pressures.

For a given initial moisture content the blister temperature is not monotonic

with heating rate. Starting from the lowest heating rates the blister temperature initially decreases, but then increases as heating rate is increased. As heating rates increase from the threshold for blistering, the remaining moisture content and hence vapor pressure at a given temperature will increase. The combination of reaching higher pressure for the same temperature and the decrease in the material's stiffness at higher temperatures causes the blister temperature to decrease with increasing heating rate. However, above a certain heating rate virtually no moisture diffuses from the sample during the duration of the test. In that case the pressure-temperature curve essentially follows the saturation pressure curve. The high rate of heating also causes the internal steam pressure to increase faster. This fast pressure build up results in increased strain rate and hence a stiffer material response, which in turn delays void nucleation and increases the blister temperature.

2.4.4 TGA-FTIR Results

Results of the TGA measurements for dry and moisture saturated NR and Gr/Pi samples are shown in Figure 2.13. The data show that the dry samples lose very little weight, less than 0.2% at 350 °C, (T_g), while the moisture saturated samples lose considerable weight, 1.0% for Gr/Pi and 3.2% for NR. The total weight loss is very close to the starting moisture contents of 1.47% and 3.23% for the Gr/Pi and NR respectively. The TGA results indicate that the principal weight loss is due to the vaporization of absorbed water in the NR and Gr/Pi samples.

The FTIR data allow us to further explore the above conclusion. FTIR absorbance data are collected at intervals as the samples are heated for the TGA

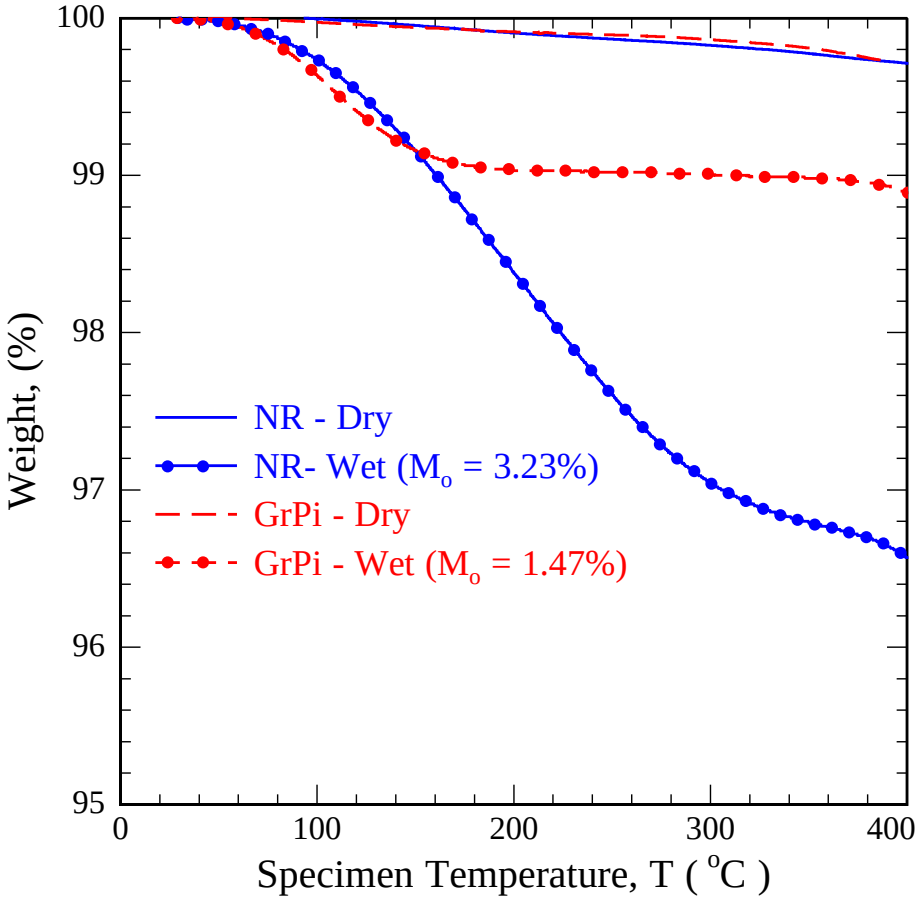

Figure 2.13: NR and Gr/Pi weight loss measurements using TGA.

measurements. The absorbance of IR radiation at specific wavenumbers is used to identify the gas species emitted by the sample as it is heated. A sample result is shown in Figure 2.14 for a moisture saturated Gr/Pi sample at temperatures of 43, 133, and 405 °C. At 133 °C considerable water is present and a very small amount of CO_2. The water has largely boiled off by 403 °C as seen by the lower plot in Figure 2.14. Data for dry Gr/Pi samples is similar but the absorbance of water is much lower due to the low moisture content of the samples. Note that the process of post-curing for 20 hours at a temperature of 370 °C has largely removed any volatile compounds including fiber sizing.

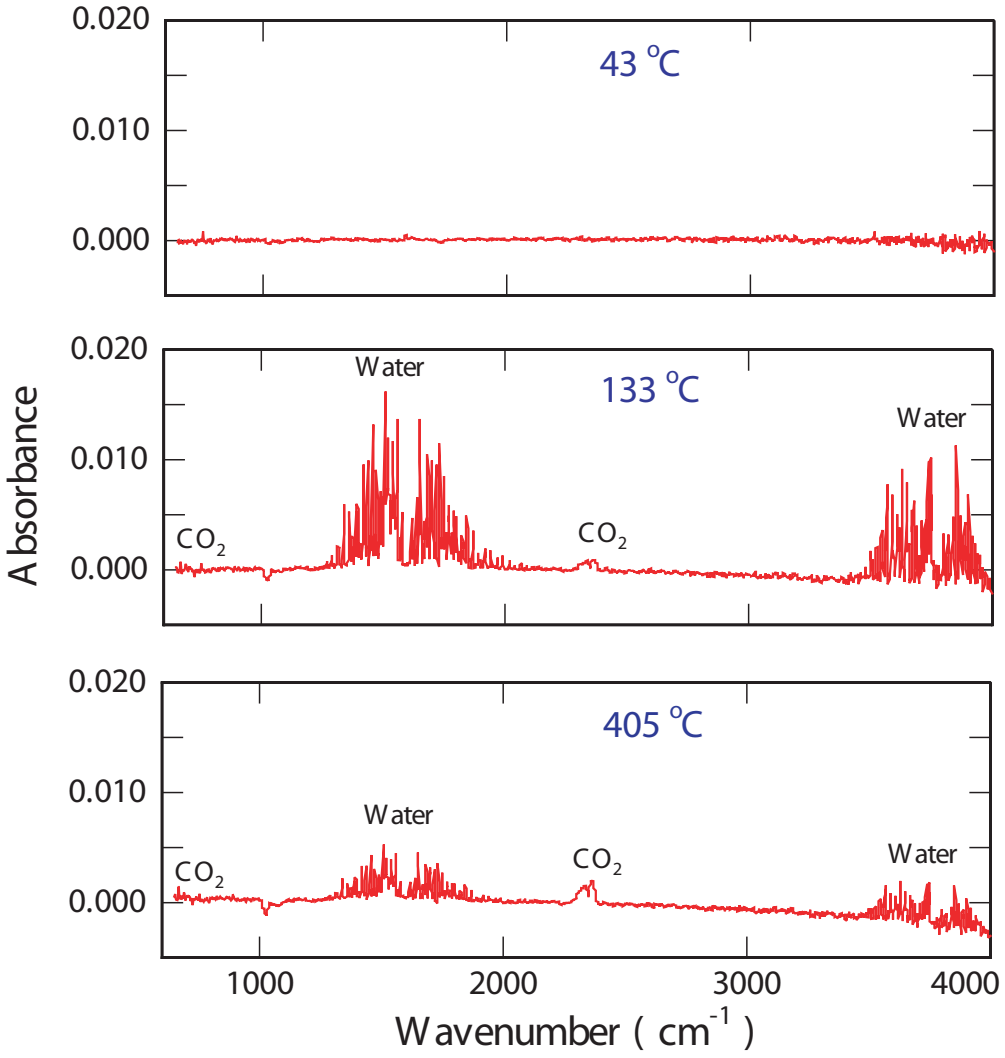

Figure 2.14: Moisture saturated Gr/Pi FTIR measurements.

The absence of anything but water below the critical blistering temperatures indicates that the primary gas coming out of the samples is water vapor and hence that the assumption that the blistering pressure is due solely to water vapor is valid.

2.5 Discussion

2.5.1 Application to Design and Life Prediction

In the initial stages of design using Gr/Pi, it is unlikely that the hygro-thermal profile for a given structure will be known in advance. As a *simple* design rule, to prevent blistering without considering actual heating rates or saturation levels, the designed structure must remain at temperatures below the lowest temperature for which blistering was observed. Examining Figure 2.12, in the case of T650-35/HFPE-II-52 this temperature is roughly 260 °C. Such a conservative approach however, may not allow the Gr/Pi material to be used to its full potential.

As an intermediate step in design, the data in Figure 2.12 can be used in a way similar to the method presented in the CMH-17 handbook, although in more general sense. The approach is to examine Figure 2.12 and from data at each moisture content, determine the lowest temperature for which blistering was observed. As an example, for NR specimens saturated at 95% RH to a moisture content of M_0=2.73% wt. the lowest temperature for which blistering was observed is 260 °C. For specimens saturated at 80% RH to a moisture content of M_0=2.73% wt. this temperature increases to roughly 275 °C. Repeating this for all moisture contents we can then construct the blister-temperature/initial-moisture-content envelope, such as seen in Figure 2.15.

Contrary to the MIL-17 Handbook approach, this envelope is not specific to a laminate geometry or heating profile, and depends only on the initial moisture content. The dependence on the laminate thickness is removed by the fact that

the temperatures in Figure 2.15 are computed at the location of void nucleation, and are not taken as the temperatures applied at the boundary. The dependence on heating rate is removed by the fact that all temperatures in Figure 2.15 were obtained from tests done at fast heating rates, where the moisture content remained unchanged in the center of specimen. From the point of view of pressure build-up, these rates can be thought of as being infinitely fast, and give the most conservative estimate of blister temperature. Below the effective infinite heating rate, re-examining Figure 2.12, it is seen that the critical temperature increases as heating rate is reduced. Therefore, for any geometry and heating profile, as long as the maximum material temperature is accurately computed and remains below the solid line in Figure 2.15, the structure will not experience steam-induced damage.

In order to fully exploit the critical pressure-temperature envelope and to further extend the application of Gr/Pi, a more detailed approach is necessary. This approach is applicable in the advanced stages of design or life prediction. Here, we assume that the designer has prior knowledge of the geometry of the structure, the moisture and temperature diffusion properties, and the hygrothermal profile. With this knowledge, one can use a custom or commercially-available finite-difference or finite-element code to compute the temperature/internal-steam-pressure fields during the mission. To prevent the onset of blistering in the structure, one must simply ensure that the computed internal steam pressure and temperature anywhere within the structure always remains below the dashed line in Figure 2.12.

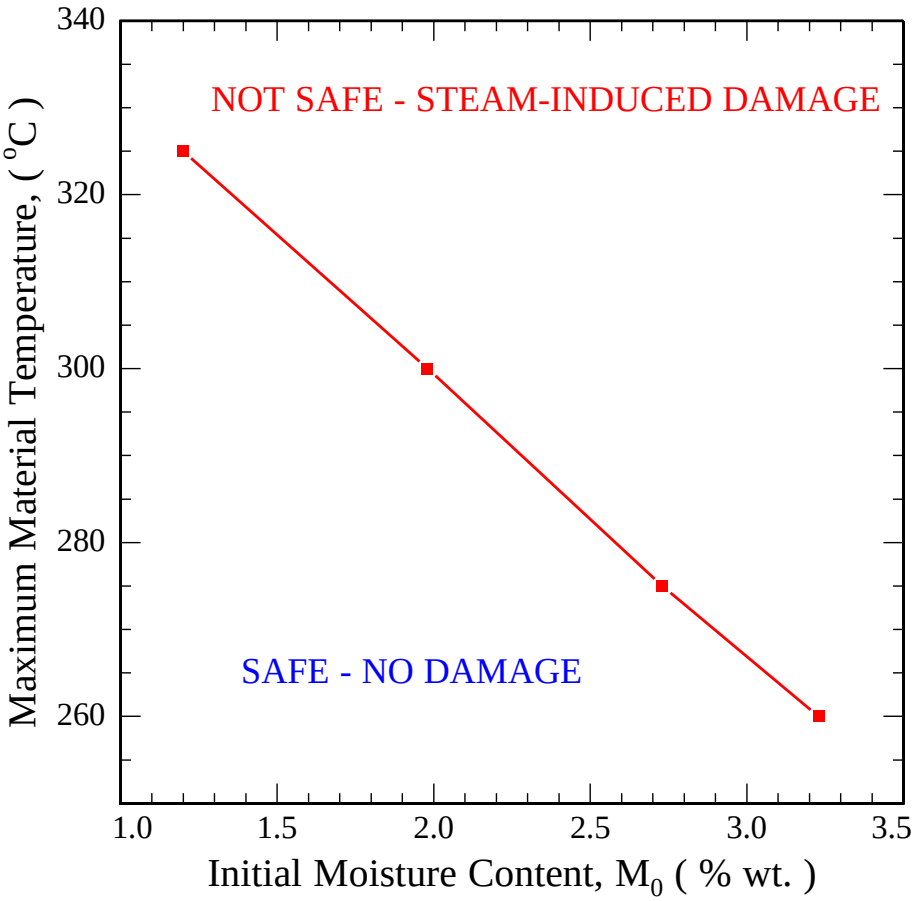

Figure 2.15: Blistering envelope for NR in terms of maximum material temperature vs. initial moisture content for infinite heating rate.

2.5.2 Recommendations

As previously stated, the most accurate method of predicting blister initiation in Gr/Pi laminates involves using data obtained from NR testing. However, it is unlikely that an engineer studying a new material system will have access to neat resin as readily as we did in this study. Therefore, for most practical purposes the onset of void initiation must be determined using laminate samples alone. Motivated by this scenario, attempts to predict damage onset in lam-

inates are discussed, followed by a recommendation for a test method using laminate samples only.

Re-examining the exploratory data for Gr/Pi specimens, it appeared that one method to determine void initiation is to find the point of divergence of strain caused by hygrothermal loading from that caused purely by thermal expansion. This comparison can be accomplished by comparing the hygrothermal and thermal curves obtained from a single specimen. Alternatively, an average thermal expansion curve can be generated for several specimens, and compared to the hygrothermal curve from previously untested specimen.

Exploring both possibilities, we found that each produces erroneous results. In the first approach, the procedure is to first fully dry a specimen and then obtain its thermal expansion curve at the desired heating rate. The test is run to temperatures that are several degrees below the glass transition temperature of the resin. This is done to ensure that the laminate is not damaged, and that the thermal and moisture diffusion properties remain unaltered. The specimen is then saturated to a desired moisture content, and tested until it fully blisters. Overlaying the strain-temperature curves from both tests and finding the point where they diverge indicates the onset of blistering. Performing this type of test at rates of 0.33, 1.0, 2.0 °C/s, we found that thermal and hygrothermal curves match up to temperatures at around 120-150 °C, and then begin to diverge. Since these temperatures are too low cause any type of damage, we conclude that this method will provide unrealistic results.

In the second approach, we found it difficult to obtain an average thermal expansion curve that can be reliably compared to data from a hygrothermal test. Comparing the thermal expansion data generated for several specimens at

a fixed heating rate, we found scatter in the shape and magnitude of the strain curves. Similar scatter was found in the moisture saturated specimens. For example, at a heating rate of 1.5 °C/s and a temperature rage of 150-250 °C the coefficient of thermal expansion for dry specimens deviated from the mean by 3-4%, and 9-10% for the moisture saturated specimens.

The reason for this large scatter can be explained by the complicated structure of a laminate specimen made out of woven fabric, and the way in which the TMA measures the specimen expansion. The TMA's probe is only 2 mm in diameter and during each new test it can measure extension at the location of the warp fibers, fill fibers, combination of both, or in the region of large resin concentration. We believe that these locations can experience different extension during heat-up, and hence cause large scatter in the data. To alleviate this problem one can perhaps use a probe with much larger diameter to get a more averaged extension measurement.

Given the above, we recommend that to accurately determine point of void initiation from a laminate specimen, one should employ a method similar to the RI test method presented in the exploratory test section. Here, for a given heating rate and moisture content, a full-ramp test is first performed and used to locate point B (Figure 2.6b) on the strain-temperature curve. Next, a series of RI tests are performed for a range of isothermal temperatures below point B. As a general rule, once the temperature that corresponds to point B is determined, a sequence of RI tests are performed with the isothermal temperatures decreasing by 5-10 °C. To define the point of void initiation, we suggest taking the average of the isothermal temperatures where the strain transitions from following the thermal expansion curve to a strain curve that indicates damage.

As an example, referring back to Gr/Pi data in Figure 2.10b, at the heating rate of 1.5 °C/s this transition occurs in between 260 and 280 °C. This correlates well with the NR data, where at the same heating rate void nucleation was observed at around 270 °C. In order not to rely on the strain data alone, all specimens should be examined under microscope for presence of voids. To obtain statistically reliable data we recommend repeating this procedure at least three times for a given hygrothermal condition. This method may appear more time and material consuming, however it should provide results that are as accurate as these obtained from NR tests. Note as well that the sample size needed in the TMA is small and that each test takes but a few minutes, thus many repeats can be performed with a modest investment of time and material.

2.6 Conclusions

In this study, a new test method to predict initiation of steam-induced damage for rapidly heated moisture saturated composite has been developed. This method entails comparing the calculated, available steam pressure within the laminate to an experimentally determined critical pressure-temperature envelope. Results from experiments performed in a thermo-mechanical analyzer were used to show that the onset of steam-induced damage can be detected by measuring the expansion of moisture-saturated specimens subjected to rapid temperature ramp. TGA-FTIR measurements support the assumption that this internal damage is solely due to water vapor pressure. Using optical microscopy of damaged laminate specimens, it has been established that steam-induced damage is a process that initiates and evolves in the resin. Comparing the data obtained from testing neat resin and laminate samples it has been shown

that initiation of steam-induced damage is more accurately detected with neat resin samples. For laminate samples, initiation and evolution of damage within the resin is constrained by the surrounding fibers and is undetectable by the TMA. Given this, data obtained from tests on neat resin performed over a range of heating rates and initial moisture saturations are used to develop a critical pressure-temperature envelope. With this envelope it is shown that the initiation of steam-induced damage is delayed when the initial moisture content is decreased and rate of heating increased. The applicability of such envelope is presented for various stages of design and life prediction. It is recommended that to prevent nucleation of voids, the internal pressure in a laminate must remain below this critical envelope. Repeated exposure of an undamaged composite to a hygrothermal cycle that exceeds this envelope may result in accumulation of voids, increase the moisture intake, and eventually result in an interlaminar delamination.

CHAPTER 3

DELAMINATION OF MOISTURE SATURATED GRAPHITE/POLYIMDE COMPOSITES DUE TO RAPID HEATING*

*M.W. Czabaj, A.T. Zehnder, and C.Y. Hui. Delamination of Moisture Saturated Graphite/Polyimde Composites Due to Rapid Heating. *Composites: Part B*, Article in Press

3.1 Introduction

Due to their high thermal resistance, specific strength and specific stiffness, polyimide-matrix composites (PiMC's) extend the application of composite materials into extreme temperature environments. Due to their excellent properties, PiMC's can be utilized in the next-generation space propulsion systems, rocket engine and missile components, and advanced turbine blades [1,2]. Employed in these structures, PiMC laminates are expected to withstand very high rates of heating and prolonged service at temperatures in vicinity of their glass transition temperature, T_g. Increased understanding of the high temperature performance of PiMC's is therefore crucial to adopting them in real-world applications.

Among the concerns surrounding the use of PiMC's is that they are prone to absorption of moisture, typically up to 1-1.5% by weight in extended exposure to high humidity environments. When moisture-saturated laminates are heated too quickly for the absorbed moisture to escape, large internal water vapor pressures can develop, leading to plasticization and hydrolysis of the matrix [3,4], void nucleation and instability, interlaminar delamination, propagation of preexisting flaws, and in worst case global failure of the structure [1,3,5,21].

To-date, the majority of research has focused on initiation and progression of the steam-induced damage in initially undamaged composites. More specifically, in most investigations, the moisture-saturated laminates contain no significant internal flaws prior to rapid heat-up and any accumulated damage is the result of the internal steam pressure. Based on experiments performed on moisture-saturated samples of polyimide neat resin, the authors of [1,3,21] con-

cluded that at high enough heating rates, internal steam pressure will lead to nucleation of internal damage in form of voids. Additionally, it was determined that initiation and evolution of steam-induced damage in moisture-saturated laminates will occur primarily in the regions of high resin concentration, i.e. between the plies of the laminate [21]. Continued heating of laminates containing internal blisters may result in further damage and weakening of the bond between plies, eventually leading to interlaminar delamination.

An additional mode in which PiMC's can fail during a severe hygrothermal cycle involves laminates containing pre-existing flaws. Such flaws, mainly in the form of interlaminar delaminations, may result from fabrication defects, impact damage or an earlier hygrothermal cycle. When rapidly heated, the moisture trapped within a laminate containing a delamination flaw will pressurize the delamination, potentially leading to delamination fracture.

Under different conditions one of these failure modes will be favored over the other. For example, in a relatively thick laminate containing a delamination in the midplane, one may expect that blistering will occur prior to delamination growth. Here, the material surrounding the delamination is relatively stiff which will suppress delamination. However, in a thin laminate, the material surrounding a large flaw will be relatively compliant and an increase in internal pressure will cause significant deformation, which may eventually supply enough energy to cause fracture. To explore the interaction between these two failure modes, parameters such as initial moisture concentration, heating rate, laminate geometry and quality, presence of internal flaws, their shape, size and location must be considered.

The aim of the present work is to develop the experimental and theoretical

basis needed to understand and predict steam-induced delamination. An experimental setup was built that allows for rapid and uniform heat-up of moisture-saturated laminates containing delaminations. The experiments are performed on T650-35/HFPE-II-52 graphite/polyimide (gr/pi) laminates, pre-implanted in the midplane with circular starter cracks. The deformation of these flaws and any subsequent delamination growth is measured locally using custom designed transverse extensometers. A theoretical model for calculation of internal steam pressure within a deforming circular cavity is derived. For each specimen tested, a linear elastic fracture mechanics (LEFM) approach is adopted to predict the conditions necessary for delamination fracture.

In what follows an experimental and analytical investigation in steam-induced delamination of gr/pi's is presented. The theoretical model is first derived, followed by a description of specimen fabrication and of the experimental setup. Next, the experimental results are presented and compared to the theoretical predictions.

3.2 Theory

A complete theory for the prediction of vapor pressure in a deforming cavity and for the deformation and fracture of a circular flaw in laminate is presented here. Circular flaw geometry was selected to simplify the analysis; however, the general approach presented here can be extended to arbitrarily shaped flaws. The theory starts with computing the amount of moisture that diffuses from the surrounding material into the cavity [6,8,9] and relating that to the steam pressure using the ideal gas law. Next the deformation of a circular delamination

flaw under pressure is calculated using shear deformable plate theory. Based on the deformation, the energy release rate available for fracture is computed and a tensile mode fracture criterion is developed based on exceeding a critical energy release rate.

3.2.1 Vapor Pressure Calculation

To calculate the vapor pressure, consider the problem depicted in Figs. 3.1 and 3.2. The laminate has a width and length L and thickness $2h$. The delamination has an initial height of $2h_c$, radius of a_0, and its origin is placed in the midplane of the laminate. Generally, $L >> h$, $a_0 >> h$, and $h >> h_c$. Due to mid-plane symmetry of the problem only half of the geometry is considered.

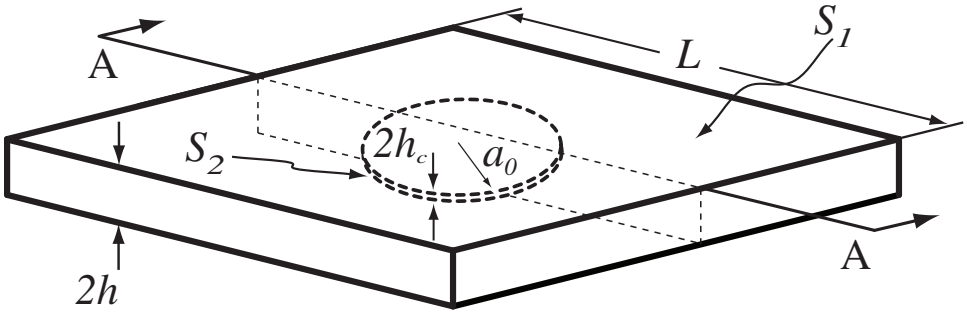

Figure 3.1: 3-D sketch of the initial model geometry.

Initially the laminate has a moisture content of M_0, and temperature T_0. The moisture content is defined as weight percent of moisture gained during saturation [17]. The delamination has an initial volume, $V_0 = \pi a^2 h_c$. Substituting V_0 into the ideal gas law,

$$P(t) = \frac{n(t)RT(t)}{V(t)}, \tag{3.1}$$

where $P(t)$ is the partial steam pressure, $n(t)$ is the number of water molecules in the cavity, R is the universal gas constant, $T(t)$ is the temperature, and $V(t)$ is the cavity volume, and assuming that at $t = 0$ the partial pressure of water in the cavity equals the saturation pressure, the initial number of water molecules in the cavity is

$$n_0 = \frac{P_{sat}(T_0)\pi a^2 h_c}{RT_0}. \tag{3.2}$$

The applicability and limitation of the ideal gas law assumption is discussed in detail in [6,8,9].

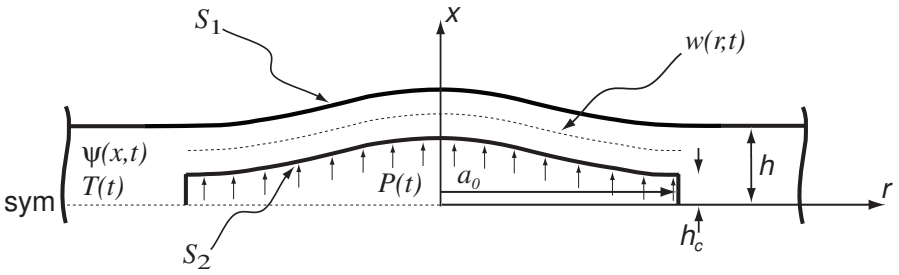

Figure 3.2: Cross-section (AA) of the laminate delamination in the deformed configuration.

In the experiments, the laminate temperature changes at a constant rate,

$$T(t) = T_0 + \dot{T}t, \tag{3.3}$$

where $\dot{T}$ is the heating rate. Generally, temperature will vary spatially, however, due to the small laminate thickness and due to heating rates that are low relative to the time required for thermal equilibrium [21] the temperature is approximately constant across the thickness.

Further, since $L >> h$, the diffusion of moisture is assumed to be one-dimensional and governed by Fick's law,

$$\frac{\partial \psi}{\partial t} = D(T)\frac{\partial^2 \psi}{\partial x^2}, \tag{3.4}$$

where ψ is the moisture concentration, $D(T)$ is the diffusivity of water in the thickness direction defined as

$$D(T) = D_0 e^{\frac{-E_a}{RT}}, \tag{3.5}$$

where D_0 is the pre-exponential factor and E_a is the activation energy. In (3.4), ψ is defined as the mass of water per unit volume of composite. In the above, equation (3.4) ignores the pressure driven diffusion which is significant for porous materials or severely damaged laminates with an inter-connected network of voids [7]. Moreover, based on an approximation of internal bending stresses in the laminate across a range of expected internal pressures, the effect of state of stress on moisture diffusivity [22] was ignored in (3.5).

Since $L - a_0 >> h$, the deformation of the material surrounding the delamination is described using shear deformable plate theory. The material above and below the delamination is modeled as a clamped circular plate under constantly-distributed pressure loading. The displacement field is

$$w(r,t) = \frac{a^4 P(t)}{64 D_x}\Big(1 - \frac{r^2}{a^2}\Big)^2 + \frac{a^2 P(t)}{4 K_s G h}\Big(1 - \frac{r^2}{a^2}\Big), \tag{3.6}$$

where r is the radial coordinate from the center of the delamination, D_x is the bending rigidity of the composite, K_s is the shear correction factor taken as 5/6, and G is the transverse shear modulus [23].

Describing the boundary conditions that drive moisture diffusion, it is first assumed that the moisture concentration on S_1 (see Fig. 3.2) equals the concentration of the surrounding air,

$$\psi(x = h, t) = \psi_\infty. \tag{3.7}$$

The main difficulty lies in defining the boundary condition on S_2, the laminate/cavity boundary. In the deforming cavity, moisture concentration varies

not only with the flux of moisture across the boundary, but also with changing cavity volume. The derivation begins by invoking the local equilibrium of chemical potential on the laminate-cavity boundary [8, 24], where the chemical potential of water in the laminate (μ_l) and cavity (μ_c) is continuous across the interface,

$$\mu_l(x = h_c^+) = \mu_c(x = h_c^-). \tag{3.8}$$

Following the approach presented in [8], the chemical potential of water in the composite is a function of the time and position; while in the cavity the chemical potential of water in the air is spatially uniform, and depends only on the relative humidity, χ, and the temperature, i.e.

$$\mu_c = \mu_0(T) + RT \ln \chi, \tag{3.9}$$

where μ_0 is the chemical potential of pure water at temperature T, and R is the universal gas constant. The relative humidity inside the cavity is expressed as

$$\chi = \frac{P(t)}{P_{sat}(T)}, \tag{3.10}$$

where $P(t)$ is the partial pressure of water vapor in the cavity and P_{sat} is the saturation vapor pressure of pure water at temperature T. The chemical potential of water in the composite can be expressed in terms of the activity of the water, a, as

$$\mu_l = \mu_0(T) + RT \ln a. \tag{3.11}$$

Assuming that the water and the polymer composite can be treated as a binary mixture [8, 24], for sufficiently small concentrations, Henry's Law is valid [25], and

$$a = k(T)\psi(x, t), \tag{3.12}$$

where $k(T)$ is the Henry's constant. Based on observation of weight gain experiments it can be shown that $k(T)$ is insensitive to temperature [8], and

$$k(T) = k(T_0) = 1/\psi_{max}. \tag{3.13}$$

where ψ_{max} is the maximum possible moisture concentration in the laminate.

Substituting (3.9-3.13) into (3.8) implies that the boundary condition for ψ at the laminate/cavity interface is

$$\psi(x = h_c^+) = \psi_{max}\frac{P(t)}{P_{sat}(T)}. \tag{3.14}$$

The flux of moisture across the interfaces is driven by the gradient of the chemical potential of water, μ, and is calculated by

$$J = -M_w\psi\nabla\mu = -D(T)\frac{\partial\psi}{\partial x} \tag{3.15}$$

where ψ is the moisture concentration at the laminate/cavity boundary, and M_w is the molecular weight of water. The cavity volume,

$$V(t) = V_0 + \Delta V(t), \tag{3.16}$$

is a function of time and changes as

$$\Delta V(t) = \int_A w(r,t)dA = \frac{\pi P(t)a^6}{192D_x} + \frac{\pi P(t)a^4}{8K_sGh}, \tag{3.17}$$

where A is the delamination surface. Furthermore, in (3.1) the change in number of moles is defined as

$$n(t) = \frac{P_{sat}(T_0)\pi a^2 h_c}{RT_0} - \frac{A}{M_w}\int_0^t J(t')dt', \tag{3.18}$$

where the first term is the initial number of moles, and the second term defines the flux of moisture into the cavity as defined by (3.15).

Substituting (3.1), (3.16), and (3.18) into (3.14) and making the following change of variables:

$$\eta \equiv \frac{x}{h}, \quad \phi \equiv \frac{\psi}{\psi_{max}}, \quad \tau \equiv \frac{D(T)t}{L^2}, \tag{3.19}$$

we obtain the non-linear boundary condition on S_2

$$\phi(\eta = h_c/h, \tau) = \frac{\alpha_1}{\alpha_2 + \alpha_3\phi(\eta = h_c/h, \tau)}\Big[\alpha_2 + \alpha_4 \int_0^\tau \frac{\partial\phi}{\partial\eta}(\eta = h_c/h, \tau')d\tau'\Big], \tag{3.20}$$

where

$$\alpha_1 = \frac{T}{T_0}\frac{P_{sat}(T_0)}{P_{sat}(T)}, \quad \alpha_2 = \frac{h_c}{a}, \quad \alpha_3 = \frac{a^3 P_{sat}(T)}{192 D_x}, \quad \alpha_4 = \frac{RT_0 h\psi_{max}}{P_{sat}(T_0)aM_w}. \tag{3.21}$$

The outside boundary condition (3.7) on S_1 becomes

$$\phi(\eta = 1, \tau) = \frac{\psi_\infty}{\psi_{max}} = 0. \tag{3.22}$$

which assumes that the surrounding air is dry relative to the specimen. The initial moisture condition in the laminate $\phi_0 \equiv \phi(\eta, \tau = 0)$ ranges from 0 to 1 depending on the relative humidity at which the specimen was saturated.

With the above, the internal steam pressure can now be obtained by solving the non-dimensional diffusion equation:

$$\frac{\partial\phi}{\partial\tau} = \frac{\partial^2\phi}{\partial\eta^2}, \tag{3.23}$$

subject to boundary conditions (3.22), (3.20) and initial condition $\phi(0) = \phi_0$. The solution to (3.23) is obtained using an implicit, backward Euler, finite-difference (FD) scheme [11, 12].

3.2.2 Energy Release Rate

Given the capability of computing the internal steam pressure within a circular delamination, it is now possible to calculate the energy release rate, G, available

for delamination growth.

The laminate is approximated as isotropic, and due to the mid-plane symmetry and uniformly distributed pressure loading, the crack tip stresses are primarily tensile, or mode-I. Despite the possible existence of a zone of non-linear deformation at the crack tip, it is assumed that deformation is globally elastic, and that G can be computed using linear elastic fracture mechanics,

$$G = -\frac{\partial \Pi}{\partial A} = -\frac{\partial}{\partial A}(U - W), \tag{3.24}$$

where Π is the potential energy of the system, U the strain energy, W the external work from the applied loads, and ∂A is the new surface created during crack growth.

For a clamped circular plate under constant pressure loading, the strain energy is [26]

$$U = \int_V \sigma_{ij}\epsilon_{ij} dV = \frac{\pi P(t)^2 a^6}{384 D_x} + \frac{\pi P(t)^2 a^4}{16 K_s G h}, \tag{3.25}$$

and the external work is

$$W = \int_A P(t) w(r,t) dA = \frac{\pi P(t)^2 a^6}{192 D_x} + \frac{\pi P(t)^2 a^4}{8 K_s G h}. \tag{3.26}$$

Substituting (3.25) and (3.26) into (3.24), and multiplying Π by a factor of 2 to include the energy contribution from the material above and below the delamination, the energy release rate is

$$G = \frac{\partial}{\partial A}\Big(\frac{\pi P(t)^2 a^6}{384 D_x} + \frac{\pi P(t)^2 a^4}{16 K_s G h}\Big). \tag{3.27}$$

Finally, assuming $\partial A = 2\pi a da$ yields

$$G = \frac{P(t)^2 a^4}{64 D_x} + \frac{P(t)^2 a^2}{4 K_s G h}. \tag{3.28}$$

The values computed using (3.28) can now be compared to the mode-I fracture toughness, G_c, of the material. Delamination fracture is predicted to occur when the available energy release rate exceeds the temperature dependent fracture toughness, i.e. $G \geq G_c(T)$.

3.3 Experimental Procedures

3.3.1 Specimen Fabrication

The gr/pi fracture samples were manufactured using a T650-35/HFPE-II-52, eight-harness satin weave, UC309 epoxy sizing, fabric prepreg. A four-ply, $[0°/90°]_s$ layup was employed where the 0° orientation corresponds to the fill direction of the woven fabric. Two laminates with dimensions of 304×304 mm were compression-molded at a maximum temperature of 371 °C, 3.48 MPa part pressure, and 50 cm Hg vacuum. To increase resin crosslinking and facilitate outgassing of volatiles, each laminate was post-cured at 371 °C for 16 hours. The resulting laminates had an average thickness of 1.65 mm. To evaluate the quality of the cure, the laminates were visually and ultrasonically inspected for areas of large porosity, surface flaws, and dry spots. Additional details regarding the cure of T650-35/HFPE-II-52 can be found in [13–15, 21, 27].

In all fracture specimens, the circular starter cracks were created using two layers of 50 μm thick Kapton film placed between the mid-plane plies of the laminate as shown in Figure 3.3. During the cure, the two pieces of Kapton film fuse with the laminate, but develop only a weak bond with each other. In order to create a fully separated delamination a "pre-cracking" step was added prior

to the fracture test, and will be addressed in a subsequent section.

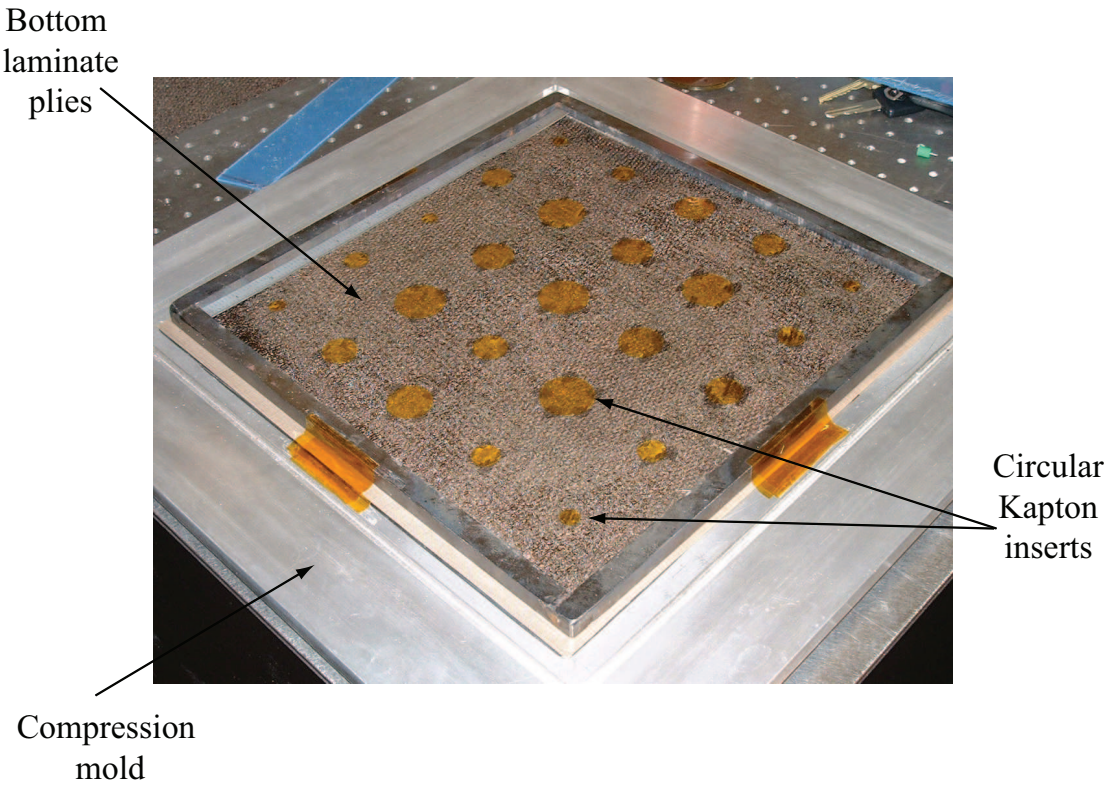

Figure 3.3: The compression mold containing bottom two plies of the laminate and Kapton starter crack inserts.

The first laminate, denoted here as "*A*", contained 25 delaminations, with radii of 5, 7.5, 10, 12.5 and 15 mm. The second laminate, *B*, contained twenty five, 10mm radius delaminations. In each case, the delaminations were equally spaced across the area of the laminate, resulting in fracture specimens with dimensions of 60×60 mm. After water-jet cutting, all specimens were vacuum dried for 4 days at 70 °C, and weighed.

3.3.2 Test Setup

The development of the experimental setup included design of a furnace and high temperature measuring devices for detection of delamination deformation and propagation. The furnace design was primarily driven by a need for relatively rapid heating rates and uniform specimen heat-up. The measuring devices were required to withstand temperatures up to 375 °C, and remain highly accurate throughout the heat-up.

Considering the relatively large specimen size, specimen heat-up was performed using the custom built radiant heating furnace depicted in Fig. 3.4. The fracture test specimen, suspended in the middle of a ceramic test chamber, was heated using four (two on each side) infrared Model 5209 Hi-TempIR heaters. The distance between the heaters and the test specimen was approximately 18 cm. Each heater, individually air and water cooled, contains six, 40 cm long, 19.2 kW quartz halogen lamps. The temperature ramp was controlled using a control thermocouple embedded in a 'dummy' specimen located immediately below the test specimen and a closed loop, Model 930 ControlIR^{TM} power control system. The gr/pi control specimen was partially split on its midplane and embedded with two 0.8 mm dia., K-type thermocouples, then glued back together using M-Bond 610 high-temperature epoxy adhesive. The first thermocouple was used for control and the second for data acquisition.

During heat-up, the out-of-plane deflection of the delamination was measured using a custom-built transverse extensometer. The extensometer depicted in Fig. 3.5 consists of two 120 mm long, spring-loaded, stainless steel arms; and 4 mm dia. 70 mm long L-shaped quartz extension rods. As seen in the figure, the extensometer arms are connected using ball bearings at the opposite end

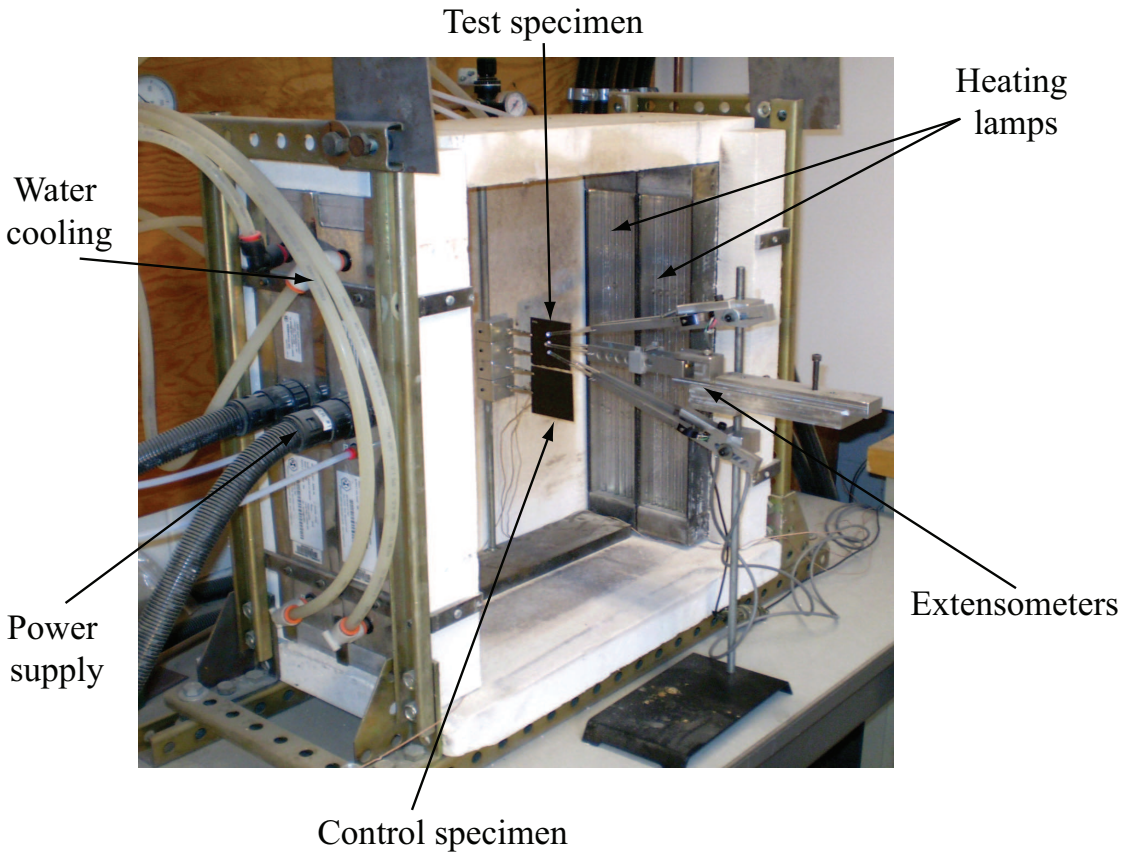

Figure 3.4: Image of the experimental setup depicting the test and control specimens enclosed in a ceramic test chamber. The heat-up is performed using water-cooled quartz heating lamps. Specimen deformation and delamination is measured using horizontally mounted extensometers.

of the quartz rods, giving the extensometer an effective measuring range of 15 mm. The extension range is kept large to prevent any damage to the quartz rods by an excessively deforming specimen. During a test, the extension is measured using a linear variable differential transformer (LVDT), which is housed on the "cool" side of the stainless steel arms. The extensometer is suspended horizontally in the middle of the test chamber and can be adjusted to clip around the test specimen in the center of the delamination. The extensometer was calibrated at room temperature using a modified Boeckeler micrometer-head to an effective

resolution of 0.01 mm.

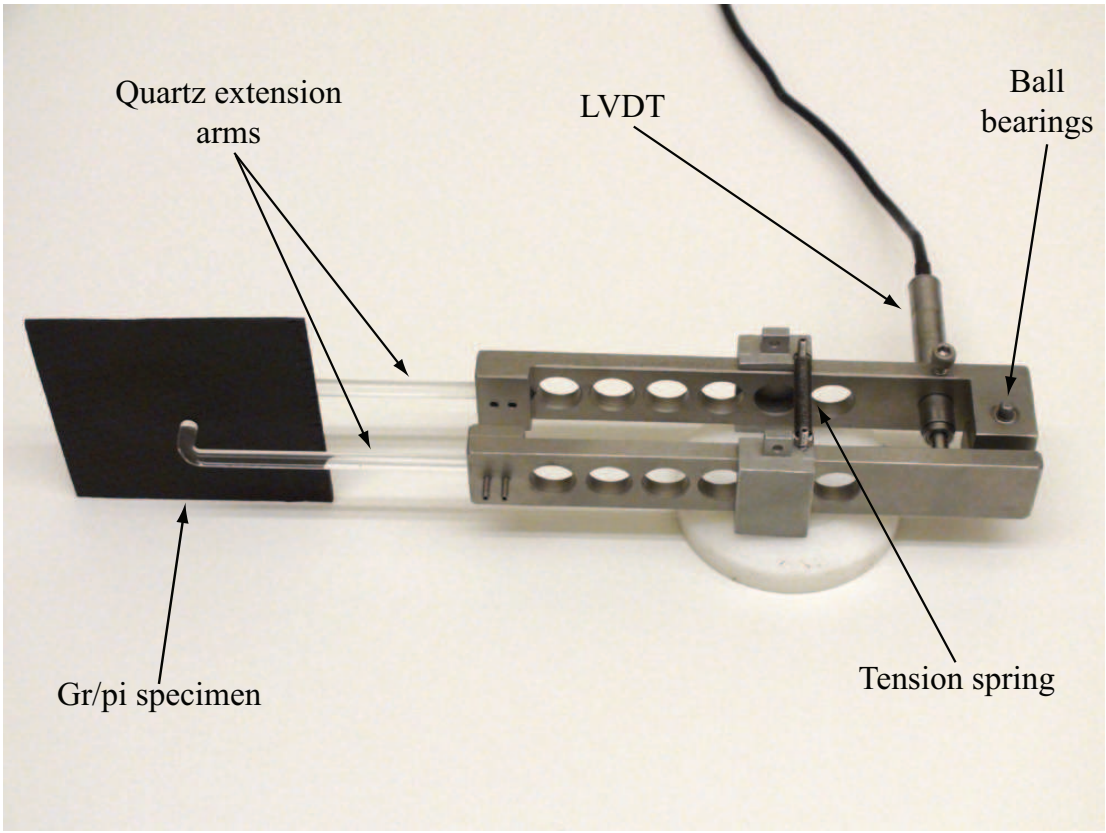

Figure 3.5: The close-up of the transverse extensometer.

Similarly, the onset of delamination growth was determined using two transverse extensometers located just at the edge of the delamination as shown in Figure 3.6. In preliminary testing it was observed that the delamination growth initiated and propagated along the 0° or 'fill' direction of this laminate. The preferred direction of growth is likely due to higher stiffness and lower fracture toughness of the composite in the fill direction relative to the warp direction [28]. Therefore the onset of growth can be captured by measuring deformation of the laminate just outside of the initial delamination along the 'fill' axis. That is, when placed just outside of the delaminated region, the delamination-

onset extensometers initially measure no change in the laminate thickness. As the condition for delamination growth is reached, the crack front propagates forward, changing the laminate thickness underneath the two extensometers, hence indicating growth.

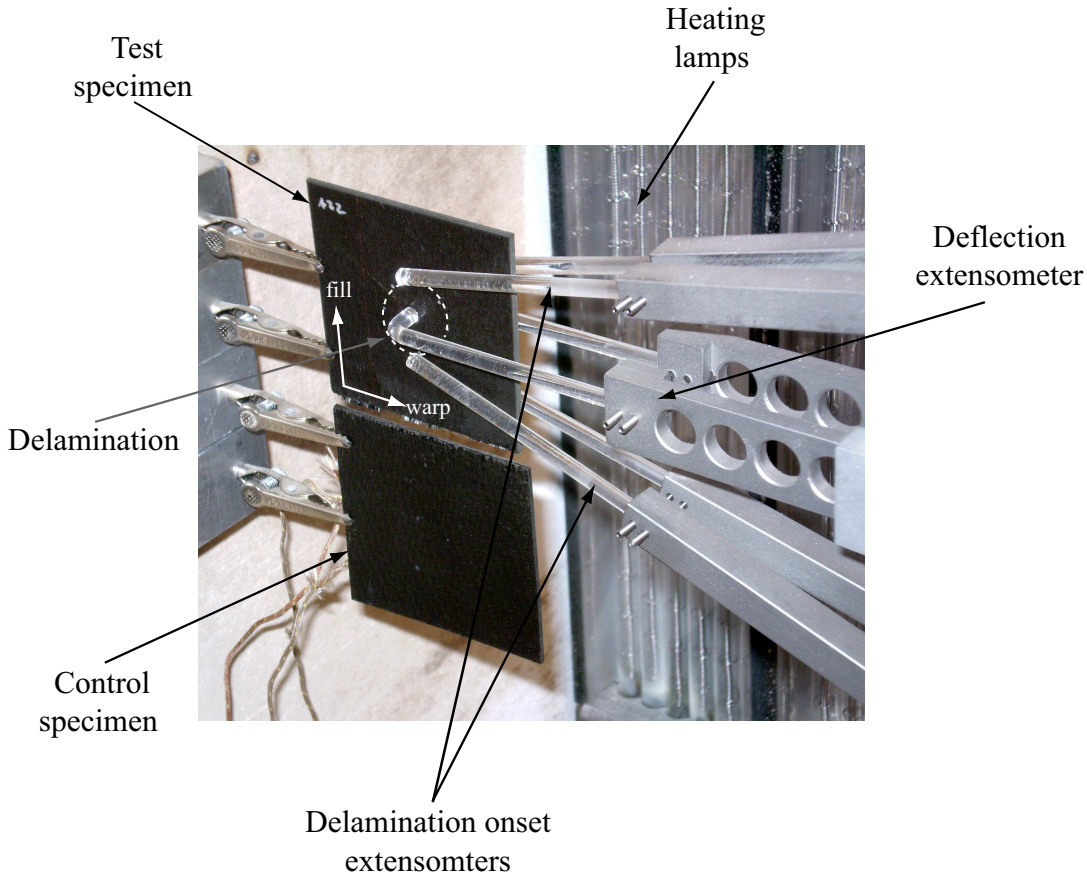

Figure 3.6: Close-up of gr/pi fracture specimen and the extensometers. The delamination onset extensometers are placed outside the approximate location of the delamination marked with a white dashed circle.

For all tests, the temperature and extension data was recorded at a rate of 2 data sets per second using a Keithley Model 7700 multiplexing digital volt meter interfaced to a computer using Keithley's ExcelLINX data acquisition software.

3.3.3 Calibration

During a fracture test, the deflection extensometer casts a shadow on the sample giving rise to a possible non-uniform temperature distribution across the delamination. Using a specimen instrumented with two thermocouples, the uniformity of temperature in the presence of the transverse extensometer was measured at heating rates from 0.5 to 2.0 °C/s. One thermocouple was placed directly underneath the deflection extensometer and one was placed in a region of un-obstructed heating. Comparing the temperature at these two locations, the temperature difference increased with increasing heating rate and ranged between 7-12 °C. For each heating rate considered here, the specimen temperature was corrected using the weighted average (proportional to the shadowed area) of the two measurements.

The final calibration of the experimental setup involved assessing the deflection caused by bending of the extensometer arms. From initial exploratory tests it was found that during temperature heat-up the thermal gradient in the extensometer arms and the force in the tensioning spring caused the arms to bend slightly outward. To quantify the extent of this bending, the gr/pi sample was replaced with a 1.5 mm thick piece of 302 stainless steel with a known coefficient of thermal expansion and tested at several different heating rates. From several test runs it was discovered that to consistently obtain a calibration curve for the extensometer, the entire setup had to be allowed to cool to room temperature after each run. As the calibration was slightly different for different heating rates, the calibration was repeated for all heating rates considered in this study. Next, each measurement of extensometer deflection versus specimen temperature was fit with a 5th degree polynomial for each heating

rate. This deflection was subtracted from the measured test data to obtain the true delamination deformation. As an example, a typical correction for the total extensometer deflection at 250° C was in the range of 0.25-0.3 mm.

3.3.4 Precracking

Plate *A*, the first to be fabricated, was used for a series of exploratory tests. Specimens from this test were initially saturated to 95% RH and were tested at 1 °C/s. A typical result was that the delamination would show no opening until a critical temperature was reached, at which point the delamination would suddenly deform and fail by dynamically propagating the crack front to the edge of the sample. This behavior was a result of the previously mentioned bond between the two Kapton layers used to create the delamination. To create an open starter crack that better simulates delamination damage in a laminate, the two bonded layers of Kapton had to be first disbonded.

The most reliable procedure found was to heat the saturated sample at a moderately low rate, 0.5 °C/s. While monitoring the experiment, at the first moment that debonding of the fused crack surfaces was detected, the IR lamp power is switched off. The lamps respond within 1 s, halting any further temperature increase, and hence pressure increase and crack propagation. It must be noted that for most samples the Kapton separation test was terminated at temperatures of 190 to 210 °C, below the minimum temperature required for onset of blistering [21].

To verify the success of this process, selected samples were sectioned and examined in an optical microscope after pre-cracking. No blistering of the matrix

was observed and in worst case instances the delamination crack was found to have grown no more than 1-1.5mm beyond the Kapton insert. To nondestructively qualify that pre-cracked samples were not damaged, the sample thickness and equilibrium moisture concentration after pre-cracking were measured. Any sample whose residual thickness has increased by more than 5% or whose moisture absorption had increased by more than 10% was rejected from subsequent testing.

One consequence of this approach and relatively low sample size is the fact that only certain size delaminations could be accurately pre-cracked this way. The smaller 5 and 7.5mm radius delaminations retained a large amount of permanent deformation. These small radii delaminations were harder to separate and needed to be heated up to much higher temperatures, which in turn weakened the matrix to the point of irreversible deformation. With the larger size delaminations, once the Kapton layers debonded, the delamination growth became unstable, propagating dynamically out to the edges of the specimen.

Furthermore, for many specimens in this study, the above procedure either did not disbond the Kapton or the samples did not fail during subsequent testing. This behavior may be related to porosity in the fabricated specimens, and their low thickness. That is, since only two plies of the woven fabric surround the cavity on each side, there exists a possibility of voids in the laminate that can channel moisture away from the cavity and into the surrounding air, preventing pressurization of the cavity.

3.3.5 Material Properties

The model requires knowledge of the moisture diffusion properties, laminate bending and shear stiffness, and fracture toughness of gr/pi over the range of temperatures considered in this study.

The experimentally determined, through-thickness, temperature dependent moisture diffusion properties of gr/pi can be found in [21]. The average initial moisture content for specimens saturated at 80 and 90% RH after Kapton separation are listed in Table 3.1.

The temperature dependent stiffness was measured using three point bend samples in a TA Instruments Q800 dynamic mechanical analyzer (DMA). For this purpose, a region of laminate "B" was imbedded with two pieces of square Kapton film between the second and third ply. The resulting region was split in half and cut along the fill and warp axis of the fabric to provide 50×9×0.83 mm DMA samples. The specimens were tested at temperatures ranging from 20 °C to 370 °C in 20°C increments. Over this range, the laminate stiffness in the fill direction was approximately 6% greater than in the warp direction. In both cases the material stiffness remained approximately constant up to temperatures of about 350 °C. The shear modulus of the laminate was estimated from composite laminate theory [29] using the known properties of the polyimide resin [14, 15] and the graphite fibers. Resin volume fraction was measured using resin digestion technique and reported in [21]. Given that on average steam-induced blistering occurred at temperatures in vicinity of 250 °C, the stiffness values at that temperature were used in analysis and are reported in Table 3.1.

Finally, the fracture toughness of gr/pi laminate at 20 °C and 350 °C were

Table 3.1: Gr/Pi laminate - material properties

Average Laminate Thickness, $2h$ (mm)	1.65
Assumed Initial Delamination Height, $2h_c$ (mm)	0.1
Average Initial Moisture Content at 80% RH, M_0 (%)	1.17
Average Initial Moisture Content at 95% RH, M_0 (%)	1.59
Fill Flexural Modulus 250°C, E_{1f}^{f} (GPa)	49.57
Shear Modulus 250°C, G (GPa)	1.74

measured using a double cantilever beam (DCB) test and reported in [30]. The variation in fracture toughness between 20 and 350 °C was assumed to be linear and approximated with the following expression

$$G_c = 2.1T + 862.2. \tag{3.29}$$

where T is the material temperature in °C and the mode-I fracture toughness, G_c, is expressed in N/m. It must be noted that all mechanical properties were measured using dry samples. Currently there exist no reliable ways of measuring stiffness or toughness of composites at such high temperatures in presence of moisture.

3.4 Experimental Results

A series of experiments were performed on specimens containing 10 mm radius Kapton inserts. Specimens were saturated at 80 and 95% RH, and were tested at heating rates ranging from 0.2 to 1.0 °C/s. Typical data for an experiment performed at 1 °C/s. are shown in Figure 3.7. The upper curve, ob-

tained from the deflection extensometer, corresponds to one-half of the center-point deflection of the circular cavity. The bottom two curves, measured using the two delamination-onset extensometers describe the change in thickness of the laminate immediately outside of the initial delamination area, along the fill axis of the laminate. The onset of delamination curves are expressed in volts as they are meant to show a relative change in thickness and not exact measurements. In this figure, the pre-cracked delamination begins to open as soon as the sample heats up, while the delamination-onset extensometers record zero thickness change. At approximately 226°C the bottom of the two extensometers detects the onset of delamination growth, which at the same time corresponds to a change in slope of the delamination center-point deflection curve. As the temperature is increased beyond 226 °C, the delamination propagates along the fill direction until the edge of the specimen is reached, causing de-pressurization of the cavity, and a sudden decrease in its height.

Repeating such experiments, the critical temperature at the onset of delamination fracture was measured and is plotted in Figure 3.8 as a function of the heating rate for the two initial moisture saturation levels considered. The dashed lines designate hypothetical trend curves only and are used to highlight the data. The solid curves and shaded regions give the model predictions discussed in the next section. At each saturation level, the critical rate at which specimens did not delaminate was 0.125 °C/s (95% RH) and 0.25°C/s (80% RH). At such low heating rates the moisture in the laminate has enough time to diffuse out and dry the sample without critically pressurizing the delamination. Additional tests were repeated at these rates to ensure that absence of delamination growth was not due to porosity in the laminate. Examining Figure 3.8 further, at any given heating rate the delamination temperature is higher for

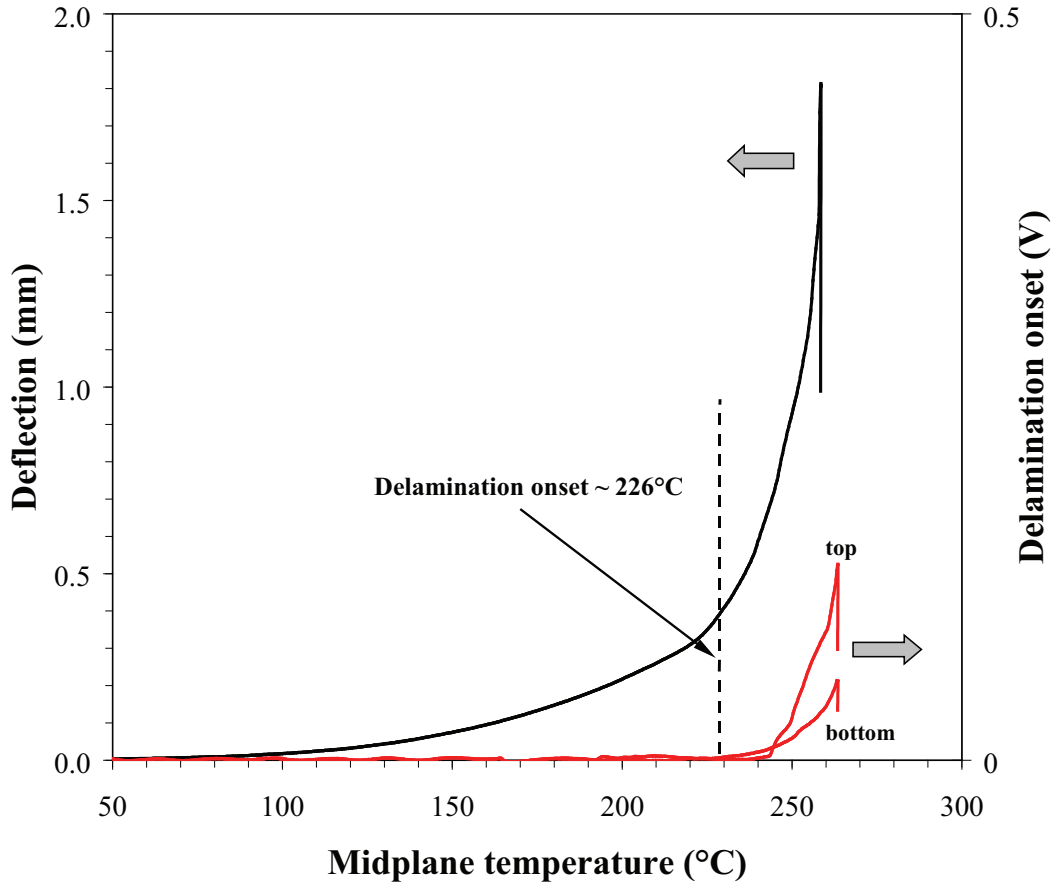

Figure 3.7: Example of experimental data, cavity deformation (one-half center point deformation) and onset of delamination. Specimen saturated at 95% RH and heated at 1.0 °C/s. Gray arrows point to respective y-axis of the curves shown.

lower initial moisture saturation. This is also expected. The ratio $P/P_{sat}(T)$ is proportional to the amount of water available in the cavity, thus to reach the same pressure higher temperatures must be applied for lower moisture concentrations. Additionally, the experimentally measured delamination temperatures generally trend upwards with increasing heating rate. The reasons for this trend are unclear, but it can be speculated that it arises from an interaction of rate dependent fracture toughness [31] and of hydrolytic degradation of the matrix

material under moist, high temperature conditions. That is, samples heated at slow rates remain at relatively high temperatures for long periods of time, and are hence expected to experience higher material degradation effectively decreasing fracture toughness and hence delamination temperature.

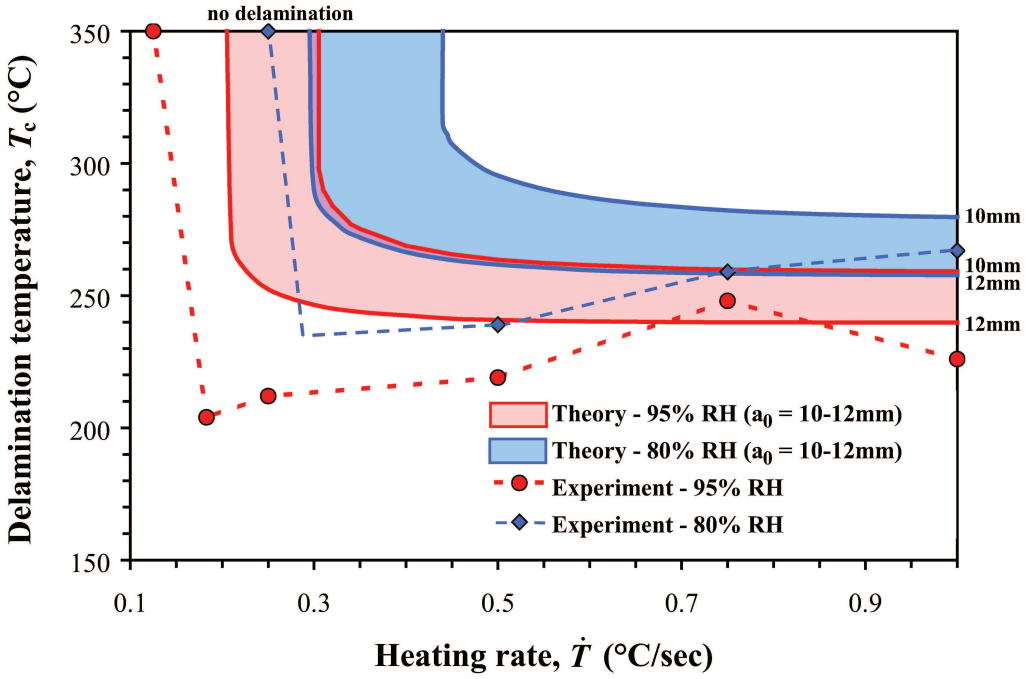

Figure 3.8: Delamination temperature versus heating rate - experimental results and model predictions. The dashed lines represent hypothetical trends and are used to highlight the experimental data.

3.5 Discussion

3.5.1 Comparison of Theory and Experimental Data

The previously presented theoretical model provides a complete framework for the prediction of moisture driven delamination given the thermal history, initial moisture concentration, moisture diffusivity, laminate stiffness and interlaminar fracture toughness. Based on the aforementioned properties, the theoretical model was used to calculate the pressure history in the cavity, the deflection, and the available energy release rate, G. Delamination growth is predicted to occur when $G \geq G_c(T)$.

An example comparison between the theoretical model and the experimental data is presented in Figure 3.9. In this figure an experimentally measured center-point deflection of a 10 mm radius circular cavity is compared to the theoretical prediction calculated using equation (3.6). As seen in the figure, for the 10 mm delamination size the model under-predicts the deformation by roughly a factor of two. This discrepancy can be explained by re-examining the assumption about the initial delamination size and the delamination acting as a perfectly clamped circular plate.

As described in the previous section, in most cases the process of Kapton debonding results in a slight extension of the crack beyond its original shape. Examining equation (3.6) the cavity deflection is proportional to a^4, making the calculation highly sensitive to the delamination size. Additionally, given the low ratio of shear modulus relative to flexural modulus of the laminate, there exists a possibility for a finite rotation of the material at the cavity boundary.

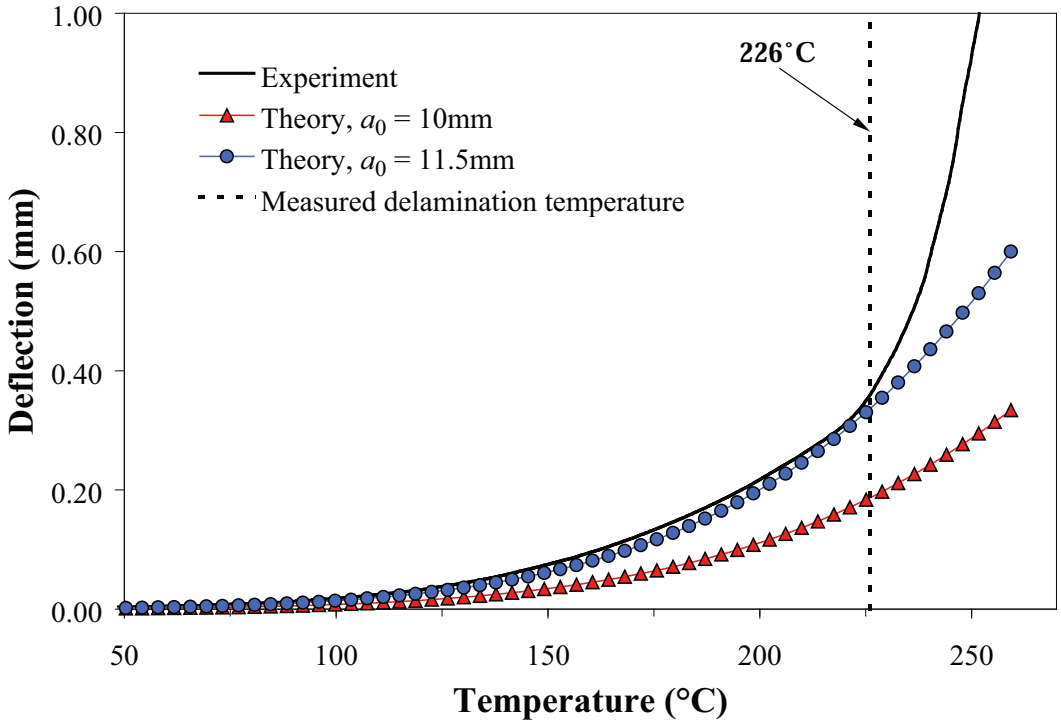

Figure 3.9: Calculated versus measured cavity deformation ($\psi_0 = 1.74 \times 10^{-5} g/mm^3$, $\dot{T}$=1.0 °C/s).

Hence, the initial delamination size and the assumption of clamped circular plate can over-predict the actual cavity stiffness.

Without means to non-destructively measure the delamination size of each sample and of correcting the boundary conditions, the existing deformation model had to be calibrated with the experimental data to obtain the correct cavity stiffness. This was achieved by re-calculating equation (3.6) with an increased delamination radius to match the measured deflection. As shown in Figure 3.9 a good agreement was achieved when the delamination radius was increased by 1.5 mm, which is the range of 1-1.5 mm radius increase during Kapton debonding measured by destructive inspection. It must be noted that a similar type of approach has been effective in correcting experimental results

for fracture of laminate composites [32], and has been accepted in standard practice [33].

Using a new radius of 11.5 mm the energy release rate, G, is calculated and plotted in Figure 3.10 versus temperature. The measured fracture toughness as a function of temperature is also shown in the figure. The condition for initiation of delamination growth is predicted when the toughness curve, G_c intersects the available energy release rate curve. For the experiment simulated in Figure 3.10, fracture is predicted to occur at 244 °C, 18 °C higher than the measured critical temperature.

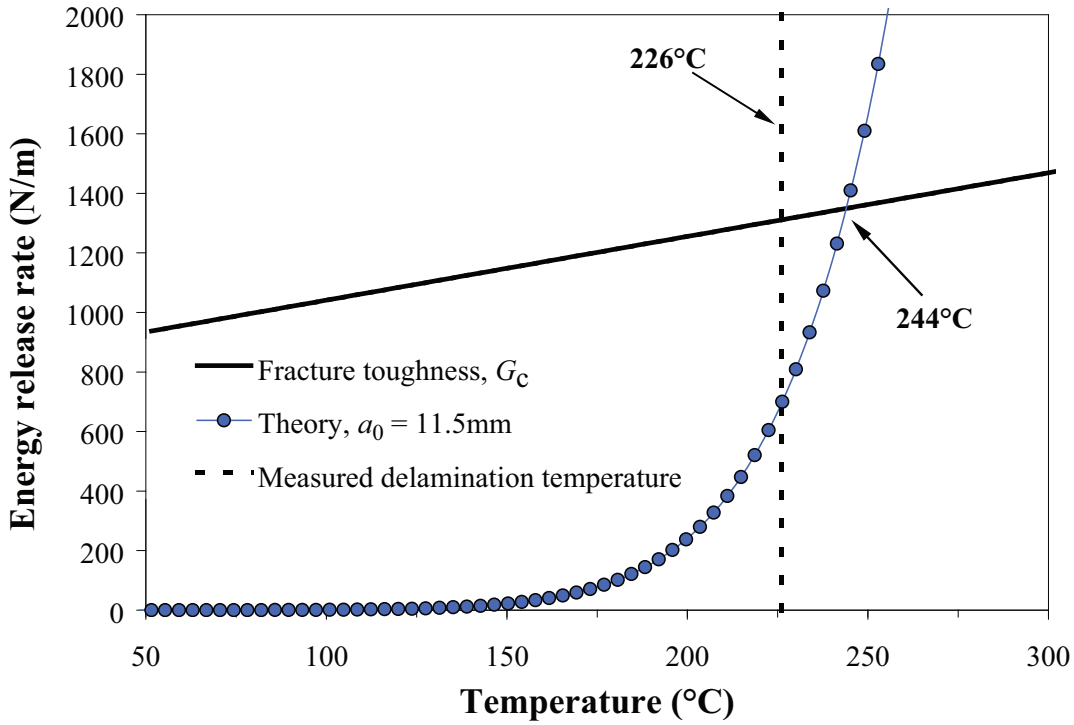

Figure 3.10: Plot of computed energy release rate and measured fracture toughness. Intersection of both curves gives a condition for delamination growth. (a_0=11.5 mm, $\psi_0 = 1.74 \times 10^{-5} g/mm^3$, $\dot{T}$=1.0 °C/s).

Using this approach, the predicted delamination fracture temperature for flaws between 10 and 12 mm in radius is plotted in Figure 3.8 (shaded regions) as a function of heating rate. The numerical data is presented this way as there does not exist a unique radius increment that can accurately calibrate all experimental results. Therefore, the theoretical predictions shown in Fig. 3.8 are used to make a qualitative comparisons with the experimental data. Examining the figure, the predicted delamination temperature decreases with an increase in moisture content. Additionally, for each moisture content there exists a heating rate below which the specimens dry out without delamination. This observation is consistent with the experimental data. A major difference between the theory and experimental results is that theory predicts the delamination temperature to decrease with increasing heating rate while the experimental data show it increasing with heating rate. As mentioned in the experimental results section, the difference between the model predictions and measured data may arise from rate dependence of fracture toughness and hydrolytic degradation of the matrix. The toughness data are obtained from elevated temperature, quasi-static DCB tests on dry samples. The HFPE-II-52 matrix exhibits significant creep at high stresses and temperatures [20], thus the delamination fracture toughness is expected to be rate sensitive. Faster rates of heating correspond to faster crack tip loading rates. An additional and possibly more important factor is hydrolytic degradation of the polyimide matrix due to moisture at high temperatures. The lower heating rate tests expose the matrix to moist, high temperature conditions for a longer duration prior to fracture, allowing for more bond breakage, which weakens the matrix, reduces fracture toughness and hence leads to lower vapor pressure and temperature for fracture.

3.5.2 Model Based Parametric Study

As mentioned, the critical temperature for fracture depends on several factors, among them fracture toughness, flaw size and initial moisture content. The dependance of delamination temperature on heating rate is summarized in Figure 3.8. To explore the effects of toughness and flaw size a parametric study is performed using the theory. From equation (3.28) the pressure at fracture scales as

$$P_c(T) \sim \frac{\sqrt{G_c(T)E(T)h^3}}{a_0^2}. \tag{3.30}$$

Knowing that pressure is approximately exponential with temperature, we expect the critical fracture temperature to increase with increasing G_c and to decrease with increasing a_0.

Holding the laminate properties and geometry constant, and fixing the initial moisture saturation at 95% RH and the heating rate at 1 °C/s. the toughness and initial flaw size are varied and the predicted temperature for delamination fracture calculated. Figure 3.11 shows the predicted delamination fracture temperature as a function of the square root of the scaled fracture toughness, $G_{sim}(T)/G_c(T)$, where the simulated toughness, $G_{sim}(T)$ is simply a multiple of the measured toughness, $G_c(T)$, i.e. $G_{sim}(T)/G_c(T)$ = constant. As expected the delamination temperature increases approximately linearly with increase in fracture toughness. This result supports the experimental data presented in Fig. 3.8. It is likely that the specimens heated at slower heating rates experience higher degradation of the fracture toughness, and lower toughness will lead to lower delamination temperatures.

Furthermore, the effects of flaw size on delamination temperature are simulated by varying the delamination radius, a_0 from 5.6 to 40 mm. The results

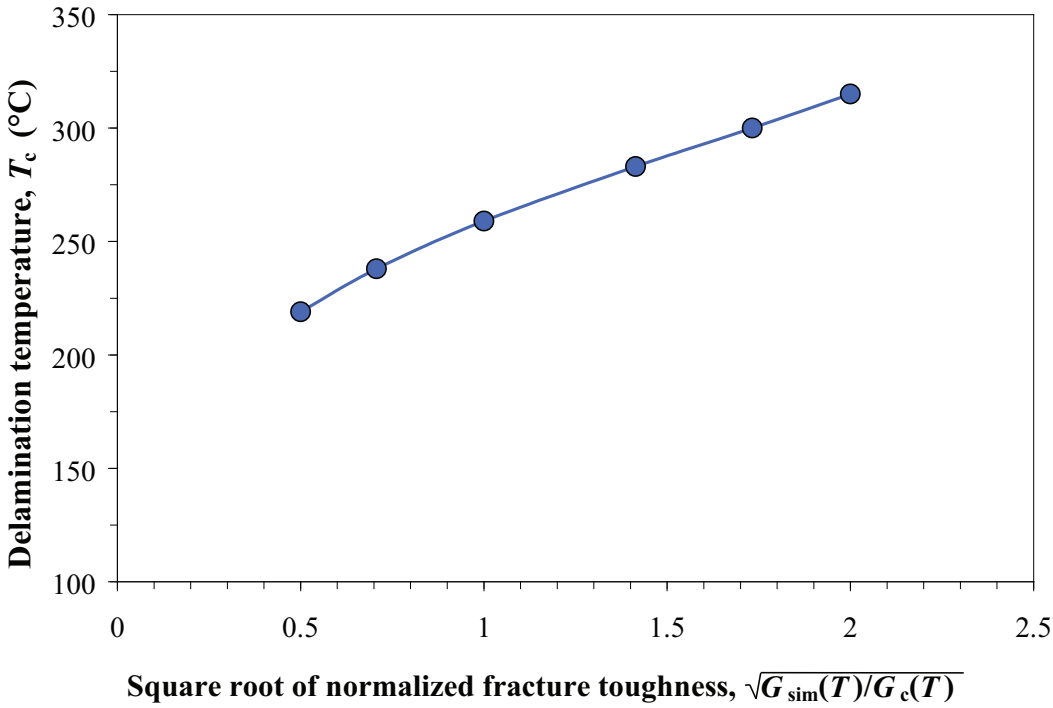

Figure 3.11: Predicted delamination temperature vs. fracture toughness (a_0=10 mm, $\psi_0 = 1.74 \times 10^{-5} g/mm^3$, $\dot{T}$=1.0 °C/s).

are shown in Figure 3.12. As expected the delamination temperature decreases with an increase in delamination size. At a fixed moisture concentration and heating rate, smaller delaminations require much greater internal pressures and hence higher temperatures to overcome the material resistance to delamination growth. As the delamination size increases the critical temperature decreases rapidly.

Finally, the effects of initial moisture content are explored in Figure 3.13. Here, the predicted delamination temperature is plotted as a function of initial normalized moisture concentration for three different flaw sizes. As seen in the figure, for each flaw size there exists a moisture content below which delamination growth will not occur below $350°C$, the T_g of the laminate.

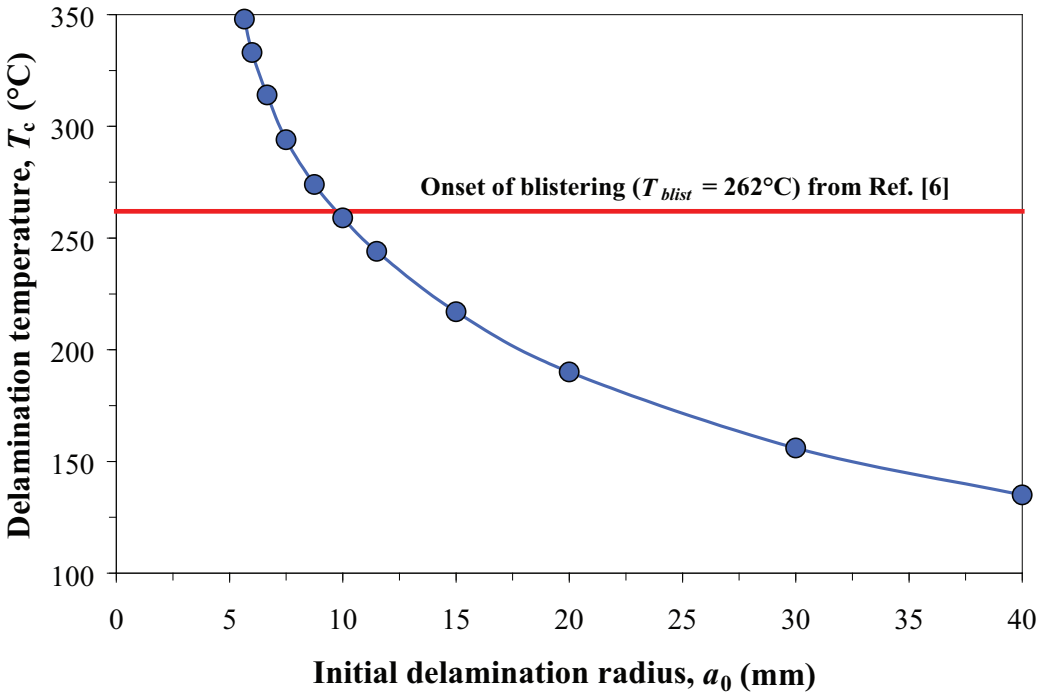

Figure 3.12: Predicted delamination temperature vs. flaw size ($\psi_0 = 1.74 \times 10^{-5} g/mm^3$, $\dot{T}$=1.0 °C/s).

3.5.3 Cross-over between blistering and delamination

Since there exist two possible steam pressure driven failure modes, it is important to study the interaction between blistering and delamination. One way to explore this interaction is by re-examining the effect of flaw size on critical delamination temperature. Here, a solid horizontal line was added to the numerical data presented in Fig 3.12, representing the experimentally measured temperature at which one would expect the onset of steam-induced blistering for an undamaged 1.56 mm, gr/pi laminate saturated at 95% RH and heated at 1.0 °C/s [21]. The intersection of the two curves corresponds to a hypothetical cross-over between the two failure modes. That is, for the set of conditions

considered here, flaws with a radius greater than approximately 9-10 mm are expected to delaminate, while flaws below that size are more likely to blister.

To further explore the interaction between the two failure modes, the measured blister temperature data from specimens heated at 1.0 °C/s at four initial moisture contents was added to the numerical data presented in Figure 3.13. This comparison further supports the fact that below a flaw size of roughly 9-10 mm in radius, one is to expect blistering, while large flaws are expected to delaminate.

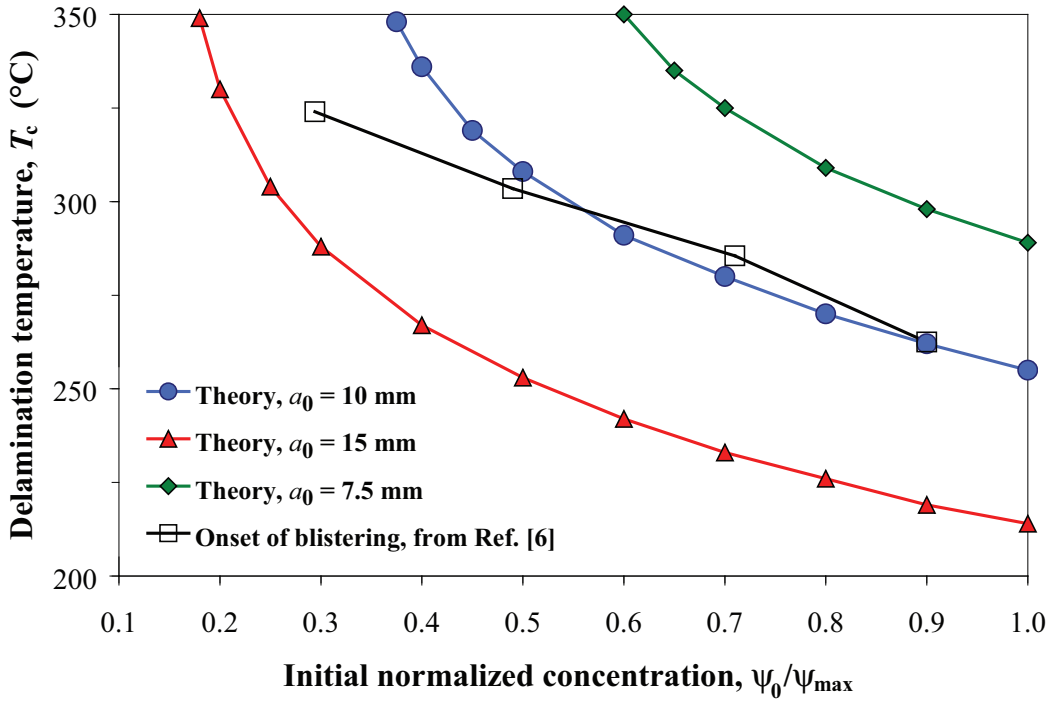

Figure 3.13: Predicted delamination temperature vs. initial concentration ($\dot{T}$=1.0 °C/sec), for various initial flaw sizes.

Additionally, one can expect that there exists a combination of hygrothermal conditions and laminate/flaw geometry such that blistering and delamination will occur concurrently. In this situation, blistering of the resin will not only

cause extensive void formation, but it will also weaken the interlaminar toughness of the material, promoting delamination.

3.6 Summary and Conclusions

In this study, experimental tests methods and a theoretical model were developed with aim of understanding and predicting the onset of steam-induced delamination. Experiments were performed by rapid heat-up of moisture saturated T650-35/HFPE-II-52 graphite/polyimide laminates, pre-implanted in the midplane with circular starter cracks. The deformation of these flaws and subsequent delamination growth was measured using custom designed, transverse extensometers. Furthermore, a theoretical model for calculation of internal steam pressure within a deforming circular cavity was derived, and combined with a linear elastic fracture mechanics approach to predict the conditions necessary for delamination growth.

The experimental results showed for a given flaw size the onset of delamination depends on the heating rate and the initial moisture content of the laminate. As expected a decrease in initial moisture content corresponded to an increase in the critical delamination temperature. Surprisingly, the delamination temperature decreased with decreasing rate of heating. This behavior may be related to a prolonged exposure of the laminate specimens to severe hygrothermal conditions. In addition, it was determined that at low enough rates of heating and/or moisture content, specimens simply dry out and do not develop high enough internal pressure to cause delamination.

The modeling efforts provided a relatively good agreement with the exper-

imental results; however, some level of calibration was required in order to account for the assumptions made with regards to specimen geometry and mechanical behavior at elevated temperatures. The theoretical model was used to highlight the effects of initial moisture content, fracture toughness and initial delamination size on the critical delamination temperature. In addition, the numerical results were used to explore the interaction between the onset of steam-induced blistering and delamination. It was shown that for a given combination of initial conditions there exists a critical flaw size below which blistering will be favored, and above which delamination growth will be more likely to occur.

The exploratory nature of this work should motivate further research. One of the major issues to be addressed is the creation of higher quality starter cracks without introducing an intermediate de-bonding processes prior to fracture test. Use of thicker laminates may lower the negative effects of high laminate porosity, provide higher yield of quality specimens, and improve non-destructive evaluation. Finally, the effect of hydrolytic degradation of the polyimide resin on mechanical properties of the laminate should be fully characterized.

CHAPTER 4

COMPRESSION AFTER IMPACT OF SANDWICH COMPOSITE STRUCTURES: EXPERIMENTS AND MODELING

4.1 Introduction

Sandwich structures consisting of composite laminate face sheets bonded to light weight core materials provide an increased bending stiffness relative to monolithic composites without significant increase in structural weight. In addition, the design and fabrication of sandwich composites is straightforward relative to other stiffened skin structures, and as a result, sandwich composite structures are widely applied in aerospace systems. One example is the use of graphite/epoxy laminate face sheets bonded to aluminum honeycomb core for construction of a prototype crew vehicle for NASA's Project Constellation [34, 35].

One of the key issues associated with use of sandwich composites is their damage resistance and tolerance. Of particular interest is the resistance of thin-skinned sandwich structures to low energy impact and post impact-damage compressive response. For such structures, numerous studies report that a low energy impact event may result in a dent that is undetectable or barely detectable by visual inspection, and yet causes extensive internal damage in the form of matrix cracking, fiber damage, face sheet debonding and delamination, and core crushing [36–41]. If undetected, the presence of such damage in load carrying components may lead to structural failure at a fraction of design load through a combination of mechanisms including unstable dent growth, face sheet kink band formation and propagation, delamination buckling, and fiber failure [40–47]. The extent of internal damage and occurrence of a particular failure mode is generally dependent on factors including face sheet layup configuration and thickness, core material, core density and thickness, interface properties between face sheet and core, impact severity, and impactor geome-

try [40].

Given the number of variables affecting evolution and interaction of failure mechanisms, the task of predicting post-impact residual strength of sandwich structures is difficult. Due to an inherent complexity of the problem, damage tolerance is generally determined for a specific panel configuration and impact damage using empirical or numerical/analytical models.

One example of a study employing an empirical modeling approach to predict damage tolerance was presented in [48]. In this study, two types of graphite/epoxy face sheet and aluminum core sandwich panels were subjected to increasing levels of impact energy and subsequently tested in compression to determine their residual strength. For each panel type, a large number of specimens tested (appx. 35-40 per panel type) did not allow for a methodical examination of the arising failure modes during compression, and hence these were ignored. The resulting strength values were represented as a function of damage severity parameters including impact energy, residual dent depth or dent area, and were used to construct A- and B-basis design allowables. The design allowable curves were employed to highlight the differences in damage resistance and tolerance between the two panel types; but ultimately all were intended as robust tools for full component design and optimization.

An alternative way of determining damage tolerance involves a less intensive testing of impact-damaged coupons that is generally aimed at revealing the underlying failure mechanisms during compression. Testing is generally limited to a specific sandwich geometry and severity of impact damage, and is intended to provide sufficiently accurate data to guide and validate the development of analytical, semi-analytical, and numerical predictive models.

Examples of some of the early efforts employing this type of approach have been reviewed in a study conducted for the U.S. Department of Transportation and the Federal Aviation Administration [40]. In recent years, a number of new experimental and modeling techniques have been proposed, the majority of which have focused on damage tolerance of thin-skinned composite sandwich panels with barely visible impact damage (BVID). Studies presented in [46, 47, 49] focused on examining the effects of low-velocity impact damage on compressive strength of sandwich panels with thin, carbon-epoxy face sheets and Nomex or aluminum honeycomb core. In each investigation, compression testing of sandwich specimens with BVID revealed three distinct modes of failure. In a number of specimens containing nominal thickness face sheets (2 plies of $0/90^{\circ}$ woven fabric), failure occurred due to progressive core crushing followed by unstable dent growth [47, 49], or due to kink band formation and propagation [46]. Kink banding is best described as localized and gradual out-of-plane buckling of the load-direction fibers near the dent boundary, which results in a band of fractured fibers that propagates perpendicular to the load direction. Additionally, panels containing marginally thicker face sheets (3 plies of $0/90^{\circ}$ woven fabric) exhibited compressive face sheet fracture [49].

Motivated by the experimental observations, a relatively straightforward semi-analytical model for simulation of unstable dent growth was developed in [49] and extended to a finite element (FE) model in [47]. In both models, the indented face sheet was modeled as a linear elastic plate, while the core was represented with a set of non-linear elastic springs. In both studies, the indentation damage was represented explicitly by changing face sheet geometry to represent the shape of a residual dent and by defining the compressive response of the non-linear springs to represent distinct regions of undamaged and crushed

honeycomb core. The response of an undamaged and crushed honeycomb was measured using a flatwise compression test [50], and dent shape was determined using a dial gauge. The results obtained from each analysis appeared to agree well with the experimental data in prediction of residual strength and dent growth failure mode; however, each model exhibited some extent of sensitivity to the honeycomb core model input parameters.

Simulation of the kink band failure mode was done in closed-form by considering the impacted sandwich panel as a plate with an open hole subjected to compression [46]. In this analysis, a stable kink band growth was obtained with a plate theory computation, while unstable growth was simulated using linear elastic fracture mechanics. The criterion for onset of unstable band growth was developed based on testing fracture specimens that were deliberately designed to exhibit kink-banding. The analysis provided good agreement with the experimentally determined strength data, showing low sensitivity to the critical modeling parameters.

A study analogous to [47, 49] was presented in [51, 52] which focused on compression testing and modeling of sandwich panels with 2-6 ply, $0/90^{\circ}$, plain weave, carbon-epoxy face sheets; Nomex honeycomb core; and low velocity impact damage. In this study, the experimental data revealed essentially two distinct failure modes, where panels with four and six ply face sheets failed due to unstable dent growth, and panels with two ply face sheets failed due to compressive fiber fracture. Unlike the approaches presented in [46,47,49], evolution and competition between the two failure modes was modeled using a single finite element model. In this model, the core damage resulting from impact and damage evolution during compression was simulated using a non-linear,

orthotropic, continuum constitutive model. The face sheet compressive failure was simulated by employing a first-ply failure degradation model based on the maximum stress and Tsai-Wu failure theory. As in previously mentioned approaches, the extent of impact damage was explicitly represented in the model by modifying the geometry and properties of the damaged face sheet and core. The numerical results provided an accurate measure of residual strength for panels with thicker face sheets or minimal face sheet damage. For thin-skinned panels with moderate face sheet damage, the numerical model failed to accurately predict residual strength. Additionally, for some geometries, the model failed to predict the correct mode of failure.

The aforementioned examples illustrate current state-of-the-art for damage tolerance prediction of impact-damaged structures. To date, the experimental techniques and empirical models developed for assessing strength of impacted specimens can be regarded as well established and require little attention. Conversely, only few detailed investigations have been performed to analytically or numerically predict damage tolerance of impact damaged panels. In addition, a significant limitation of present methods is that damage tolerance predictions assume an initial damage state due to impact. Because characterization of the initial impact damage state is limited by the currently available non-destructive and destructive evaluation capabilities, representation of initial damage requires assumptions regarding mechanical properties and geometrical features of the impacted regions. Damage tolerance cannot be predicted in a general and robust manner without representing accurately the complexities of damage due to impact.

With this in mind, the aim of this combined experimental and numeri-

cal study is to extend the current damage tolerance prediction capabilities of impact-damaged sandwich panels by moving towards increased fidelity predictive tools. The study seeks to provide relevant data and design guidelines by examining materials and sandwich panel geometries that are under consideration for NASA's next generation reusable launch vehicles. In particular, this study investigates the effects of BVID on compressive behavior of sandwich panels with thin-skin, quasi-isotropic, carbon/epoxy face sheets and low density aluminum cores. The following sections provide detailed descriptions of the experimental and numerical efforts. The first part of this study begins with preparation of the impact-damaged test specimens, development of the experimental test facilities and procedures for compression testing. The compression test results are presented next, along with their interpretation and applicability. The second part of this study begins with an overview of the modeling philosophy and a description of the supporting material testing needed for model development. A detailed description of the model is presented, followed by numerical results and comparison to experimental data.

4.2 Experimental Testing

4.2.1 Overview

The study begins with experimental testing of impact-damaged sandwich composite specimens to assess their damage tolerance in compression. To reveal the underlying damage mechanisms and highlight competition between possible modes of failure, a broad range of panel geometries was considered. For

each panel geometry, the BVID damage was obtained by performing quasi-static indentation (QSI) using 25.4 and 76.2 mm dia. spherical indentors. Each indented specimen was non-destructively evaluated to assess the extent of internal and external damage and subsequently tested to failure using a compression after impact (CAI) test. The CAI test incorporated a shadow Moiré setup to visualize and record the evolution of indentation damage and to determine the ultimate mode of specimen failure. For each specimen tested, the resulting CAI strength was normalized by the undamaged strength, determined from an edgewise compression (EC) test. The normalized value is referred to as the residual strength. The strength and residual strength data were examined as a function of panel geometry, extent of impact damage and failure mode to highlight mechanistic differences among panel configurations and to provide guidelines and "rules-of-thumb" for damage tolerant design.

4.2.2 Material System and Specimen Fabrication

Sandwich panels were fabricated by co-curing HexPly® IM7/8552 carbon/epoxy face sheets to HexWeb® CR-III, 3.2 mm cell size, 5052-H39 aluminum honeycomb core. All face sheets were hand-laid according to the quasi-isotropic layup sequences listed in Table 4.1 using eight plies of uni-directional pre-preg tape. The Q1 layup was selected as a baseline face sheet, while Q2 was selected to examine effects of the 90 degree angle change between adjacent plies. The Q3 and Q4 layups resulted from mistakes during layup. Three core geometries listed in Table 4.1 were selected to examine the effects of core thickness (C1 vs. C2) and core density (C1 vs. C3). During fabrication each core was oriented such that the core ribbon direction was aligned with the face sheet 0°

plies. The ribbon direction defines the direction in which the corrugated sheets of aluminum foil are aligned and adhered to produce the hexagonal cell pattern.

Table 4.1: Summary of face sheet layups and honeycomb cores considered

Layup - stacking sequence	**Core type - density, thickness**
Q1 - $[45/0/\text{-}45/90]_s$	C1 - 49.7 kg/m^3, t = 25.4 mm
Q2 - $[45/\text{-}45/0/90]_s$	C2 - 49.7 kg/m^3, t = 16.5 mm
Q3 - $[\text{-}45/45/90/0]_s$	C3 - 72.1 kg/m^3, t = 25.4 mm
Q4 - $[45/90/\text{-}45/0]_s$	

Prior to cure, each honeycomb core was degreased in a methanol bath and coated with three layers of 3M^{TM} EW-5000 primer to facilitate improved bonding with face sheets. Additionally, each core was filled with a 3M^{TM} EC-3524 B/A potting compound along three strips, 25.4 mm wide, running perpendicular to the loading direction (gray regions in Fig. 4.1). After panel trimming, the potting compound reinforces the loading edges of compression specimens, facilitating a uniform load distribution during compression.

The panel cure was performed in an autoclave based on a recommended cure cycle of the pre-preg material [53]. A total of thirteen, 38.1×38.1 cm panels were fabricated. Each panel was trimmed using a Norton 1A1R 203×1.14×31.8 mm, water cooled diamond wheel at 750 RPM with a feed rate of 5 cm/min. Depending on a specific need and cure quality, each panel was trimmed to produce one of the following: 17.8×15.2 cm CAI specimens, 17.8×5.1 cm EC specimens, 2.5×12.7 cm face sheet flexure specimens (debonded from the core), or a series of small square specimens for QSI evaluation tests. A schematic of a typical panel trimming layout is provided in Figure 4.1. All compression specimens were ground flat and square using a water cooled, 8000 RPM surface grinder. An ex-

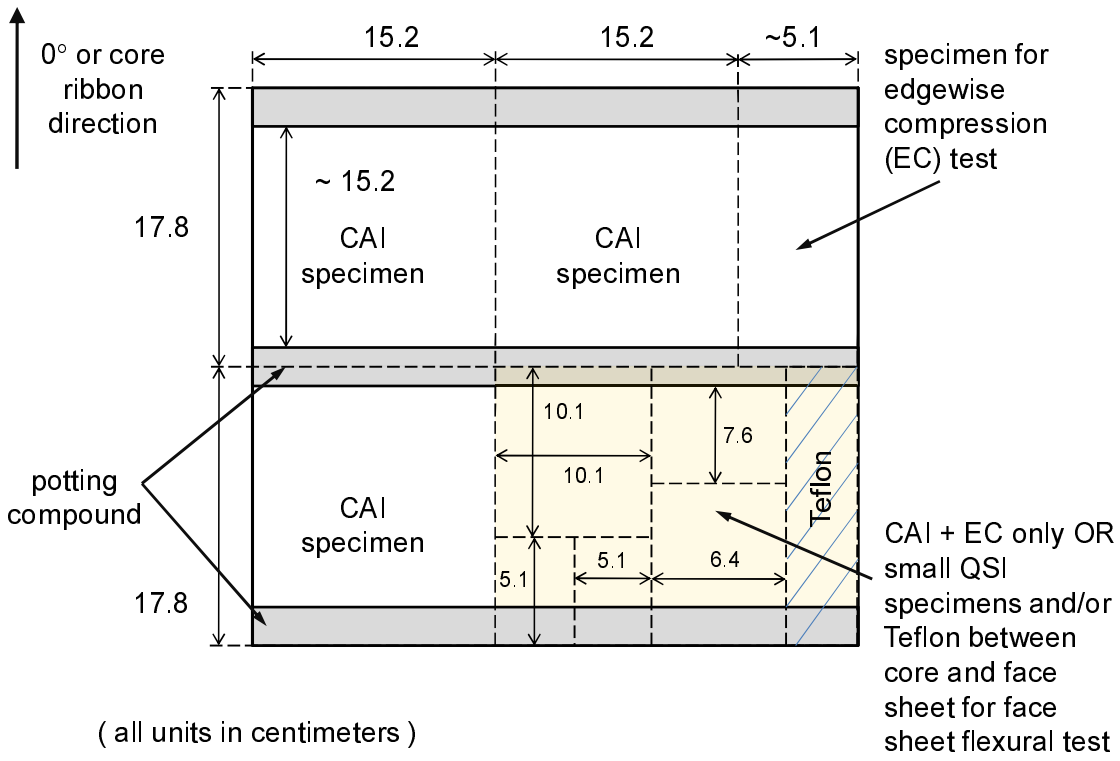

Figure 4.1: Typical trimming layout of a 38.1×38.1 cm sandwich panel (plan view). The 0° or core ribbon direction corresponds to loading direction during compression.

ample of an un-cut 38.1×38.1 cm panel and the resulting EC and CAI specimens are presented in Figure 4.2.

A summary of panel manufacturing and the resulting EC and CAI specimens is presented in Table 4.2. The first column represents the layup-core configuration, followed by the total number of 38.1×38.1 cm panels fabricated. The next three columns give the total number of undamaged and CAI specimens tested. The CAI specimens are subdivided into two columns based on the indentor diameter used to create the indentation damage.

It must be noted that for the first four geometries in Table 4.2, multiple panels were fabricated, allowing for the inter- and intra-panel comparison of undam-

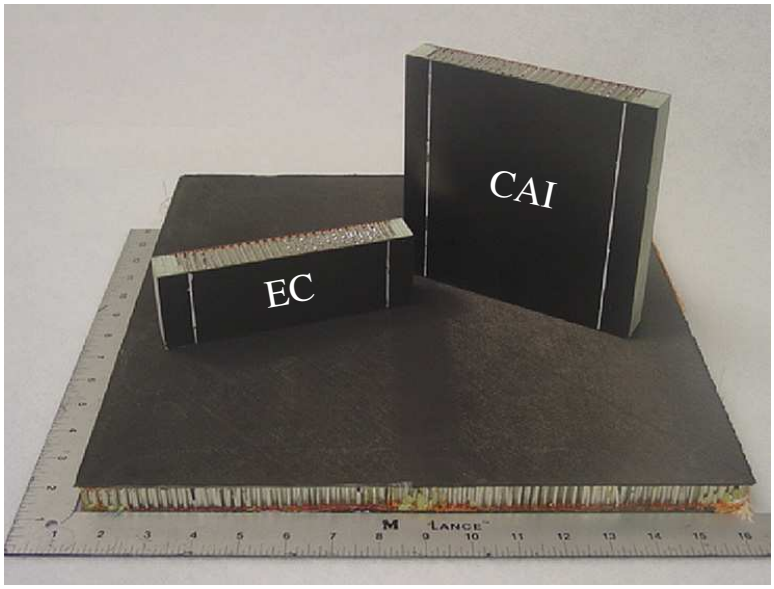

Figure 4.2: A 38.1×38.1 cm sandwich panel prior to trimming (bottom), EC specimen (left), and CAI specimen (right).

Table 4.2: Summary of panel and specimen fabrication

Specimen type	**Number of 38.1 x 38.1 cm panels manufactured**	**Number of undamaged tests**	**Number of CAI tests - 25.4 mm dia. indentor**	**Number of CAI tests - 76.2 mm dia. indentor**
Q1-C1	3	3	3	2
Q1-C2	2	4	3	3
Q1-C3	2	4	3	3
Q2-C1	3	3	5	6
Q3-C1	1	1	1	2
Q4-C2	1	2	2	1
Q4-C3	1	1	2	1
Total	**13**	**18**	**19**	**18**

aged and CAI strengths.

4.2.3 Quasi-Static Indentation Test

The final step of CAI specimen preparation was creation of indentation damage representative of low velocity impact damage at the threshold of visual detectability. Generally, such damage can be replicated with a drop test using a rigid impactor released from a pre-determined height. For a given impactor and specimen geometry, the drop height that results in BVID is typically determined by trial and error. Despite its simplicity, dynamic impact is inherently unreliable in generating consistent levels of damage across various panel configurations, and hence it did not qualify as a viable test for this study.

An alternative means of creating low velocity impact damage is quasi-static indentation (QSI). In a QSI test, a rigid indentor is statically pressed into a specimen allowing for precise control over load and final dent profile. Experimentally, it has been shown that for thin-skin sandwich panels, the QSI test reproduces the extent of internal damage from an impact event, provided that the maximum force during indentation equals the maximum force measured during impact [54–57].

A series of exploratory QSI tests were performed on small sandwich specimens to define indentation levels that correspond to BVID [58]. The indentation was performed using spherical steel indentors with diameters of 25.4 and 76.2 mm as depicted in Figures 4.3 and 4.4. In each test, the sandwich specimen was placed on top of a rigid platen and secured using two spring clamps. The indentation was performed in displacement control at a rate of 0.05 mm/s to a

desired load level. In case of the 25.4 mm dia. indentor, BVID was defined to occur at a residual dent depth of approximately 0.5 mm, which corresponded to an average indentation load of 1300 N. For the 76.2 mm dia. indentor, the BVID threshold was defined to occur at a residual dent depth of 1.0 mm, corresponding to an indentation load of 2800 N. To account for the increased stiffness of specimens with the C3 core (see Table 4.1), the indentation loads were increased to 1650 and 3500 N for the 25.4 and 76.2 mm dia. indentors, respectively. The indentation loads and target dent depths established in the preliminary study were used for all subsequent CAI specimens tested with the exception of a few specimens indented to slightly higher loads to examine the effect of increased dent depth on strength. Note that BVID dent depths for each indentor type were determined qualitatively by consensus of our research group. Thus the BVID depth is somewhat subjective. Although, others may define it differently, slightly different dent depths are not expected to dramatically affect the results.

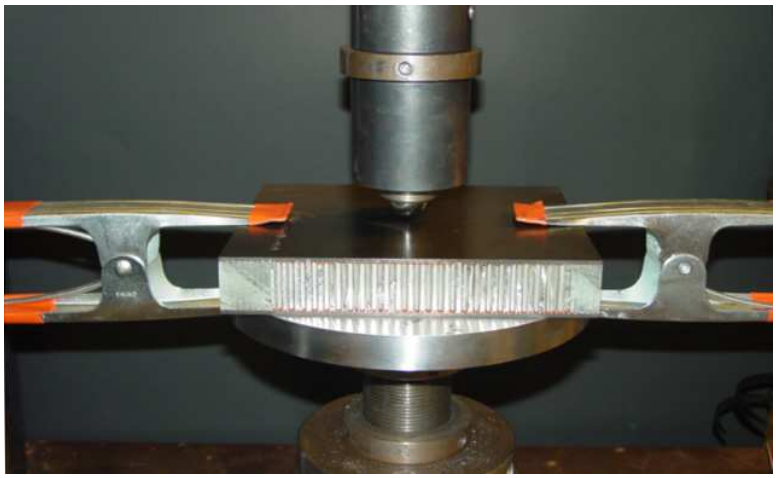

Figure 4.3: The quasi-static indentation test setup - 25.4 mm dia. indentor.

An example of load-displacement data from the two types of QSI tests is presented in Figure 4.5. Generally, each QSI curve can be characterized as having

Figure 4.4: The quasi-static indentation test setup - 76.2 mm dia. indentor.

an initially linear region followed by a region of gradual non-linear softening as the core crushes and damage initiates and evolves in the face sheet. The un-loading is highly non-linear and is caused by the rebounding face sheet and the resulting tensile un-folding of the crushed honeycomb. In Figure 4.5 the indentor displacement at the end of un-loading is indicative of the permanent dent depth, though it does not provide the exact measure due to fixture compliance.

A precise residual dent measurement for each specimen was done ultrasonically using a 50 MHz pulse-echo transducer with a 500 MHz transient waveform digitizer. The measurement was based on a time of flight between the transducer's pulse and the first wave reflection from specimens surface [58]. An example of ultrasonically measured dent profiles taken through specimen center along the 0° and 90° directions is shown in Figure 4.6. In the figure, the small differences between the 0° and 90° direction profiles for each specimen suggests that the resulting dents are not exactly circular, but are slightly elliptical.

In addition to ultrasonic measurements, each specimen was c-scanned using

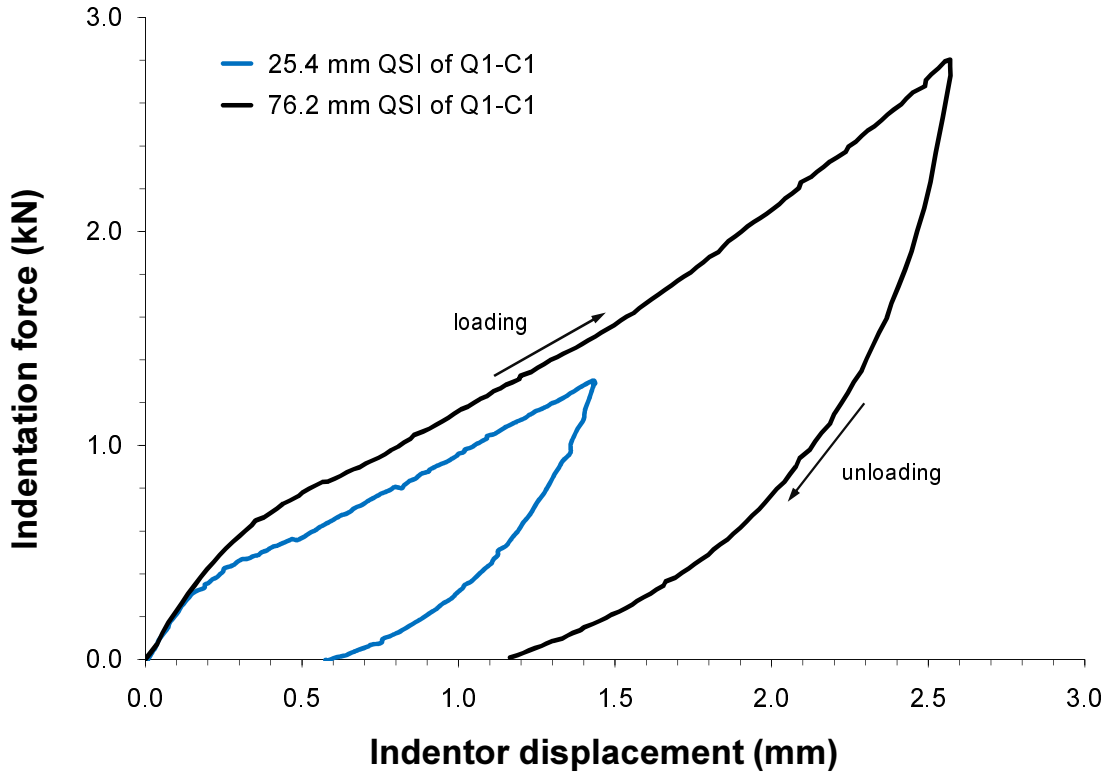

Figure 4.5: Test data from quasi-static indentation using 25.4 and 76.2 mm dia. indentors - Q1-C1 panel geometry.

the same 50 MHz pulse-echo transducer to non-destructively evaluate the extent of internal damage. For specimens indented with the 25.4 mm dia. indentor, the use of c-scan provided information on interlaminar delamination location, area, and orientation. For specimens indented with the 76.2 mm dia. indentor, large curvature of the dent surface prevented some of the same measurements; however, information on the internal damage from the inner portions of the dent were sufficient to ascertain that the delaminations in these specimens were larger than those in the specimens indented with the 25.4 mm dia. indentor, and that the pattern of the delaminations was essentially the same [58]. A complete summary of the QSI test data is presented in Tables B.1 and B.2 of the Appendix.

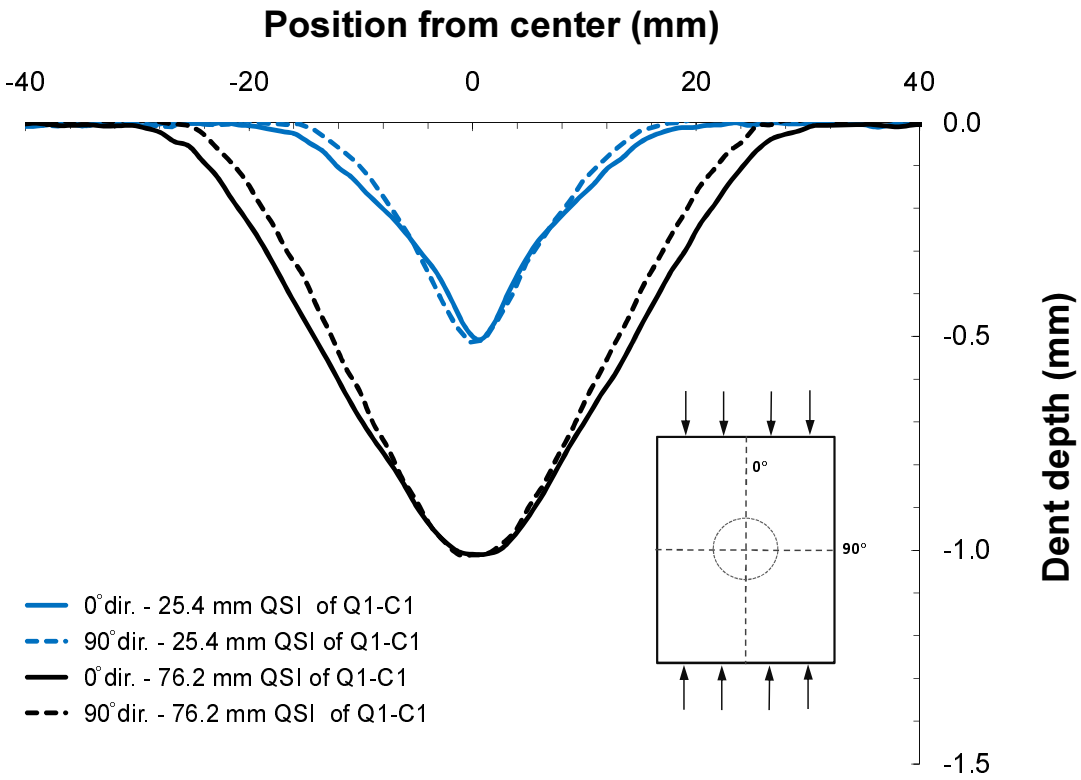

Figure 4.6: Ultrasonically measured dent profiles resulting from QSI using 25.4 and 76.2 mm dia. indentors - Q1-C1 panel geometry.

4.2.4 Compression Test Fixture

Development of the compression test setup for the EC and CAI tests was based on the designs presented in [59, 60]. A primary requirement for the new test fixture was an ability to accommodate panels with 8-16 plies per face sheet and adaptability to the available servo-hydraulic load frame. Although not explicitly considered in this study, the requirement to accommodate the 16-ply face sheets was necessary to support future experimental efforts. Furthermore, the fixture was required to provide simple yet effective alignment of test specimens prior to a compression testing. Considering that most compression tests are highly sensitive to small levels of misalignment, a uniform strain field across

the width and thickness of specimens had to be readily achieved. Additional requirements included low fixture compliance, ease of use, and flexibility to future modifications.

Selection and design of all test fixture components was based on an estimate of a maximum expected load required for compression to failure of a 15.2 cm wide sandwich specimen with 16-ply face sheets. The estimate was based on a Tsai-Wu first-ply-failure criterion [61,62] and the elastic and strength data properties of the IM7/8552 face sheet material provided by the manufacturer [53]. Based on this calculation, the compression fixture was required to withstand loads of approximately 440 kN. Because this study focused primarily on testing specimens with 8 ply face sheets, the compression fixture was adapted to an Instron 8502 load frame with a capacity of 250 kN and a T-slotted table base.

An image of the compression setup fully assembled within the Instron 8502 load frame is presented in Figures 4.7 and 4.8. The two loading platens of the compression fixture were fabricated from 2.54×7.6×24.4 cm precision-ground 1018 carbon steel bars. The top platen was bolted directly to the load cell, while the lower platen was attached to a 2501-118 Instron spherical seat, which was in turn bolted to a 2.54 cm thick, steel, load frame base adapter. The spherical seat allowed for tilting of the lower platen about the two axes perpendicular to the loading direction, providing a simple yet effective way of specimen alignment. In the current setup, tilting was achieved by tightening or loosening the four adjustment bolts mounted in the front and back of the spherical seat and on the two sides of the bottom compression platen. To prevent any sudden out-of-plane motion of the specimen during testing, a set of 1.3×2.54 cm steel bars was used to clamp the specimen to the two compression platens. Using a simple

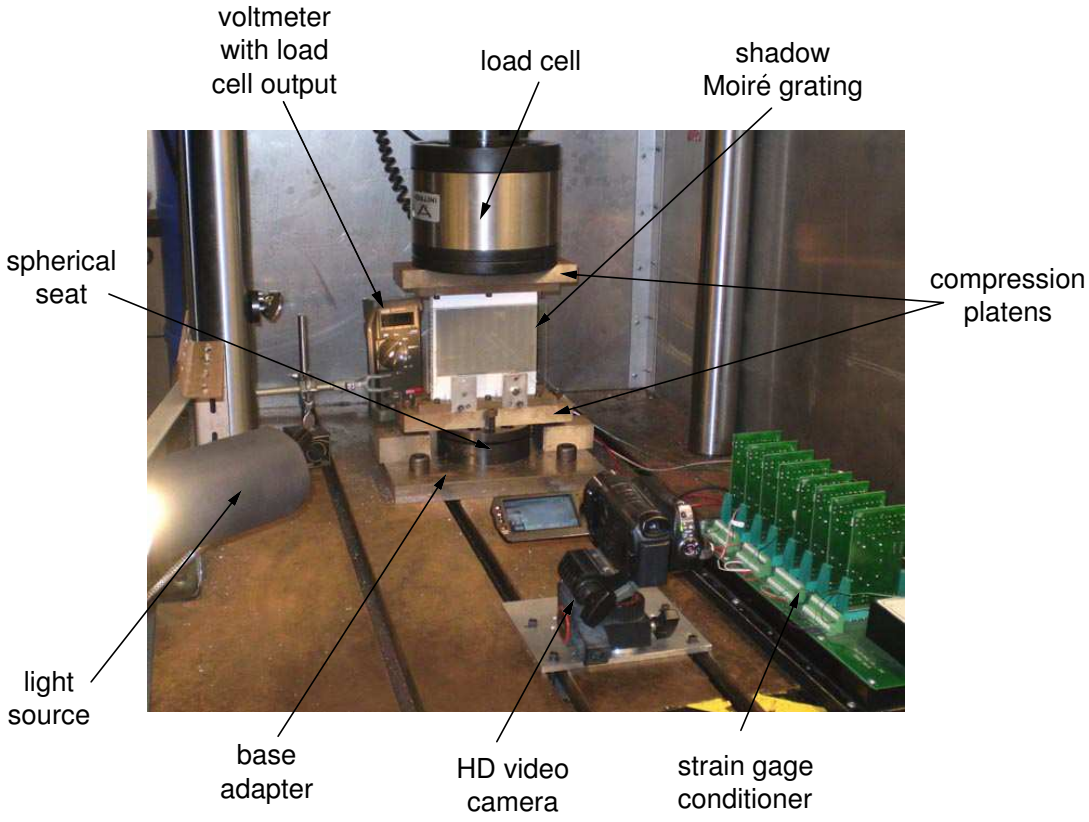

Figure 4.7: The compression test setup and the supporting data acquisition equipment.

strength of materials approximation, global buckling loads for panels considered in this study were approximately twice the expected compressive failure loads, and it was deemed unnecessary to include additional vertical constraints.

In the present setup, the horizonal constraint bars served a secondary purpose of locating each specimen in the exact middle of the compression platens. Precise specimen centering was necessary to prevent undesired global buckling (front-to-back misalignment) or localized fiber crushing (side-to-side misalignment). The centering procedure involved offsetting the rear constraint bars from fixture centerline by a distance of exactly one-half specimen's width. The exact

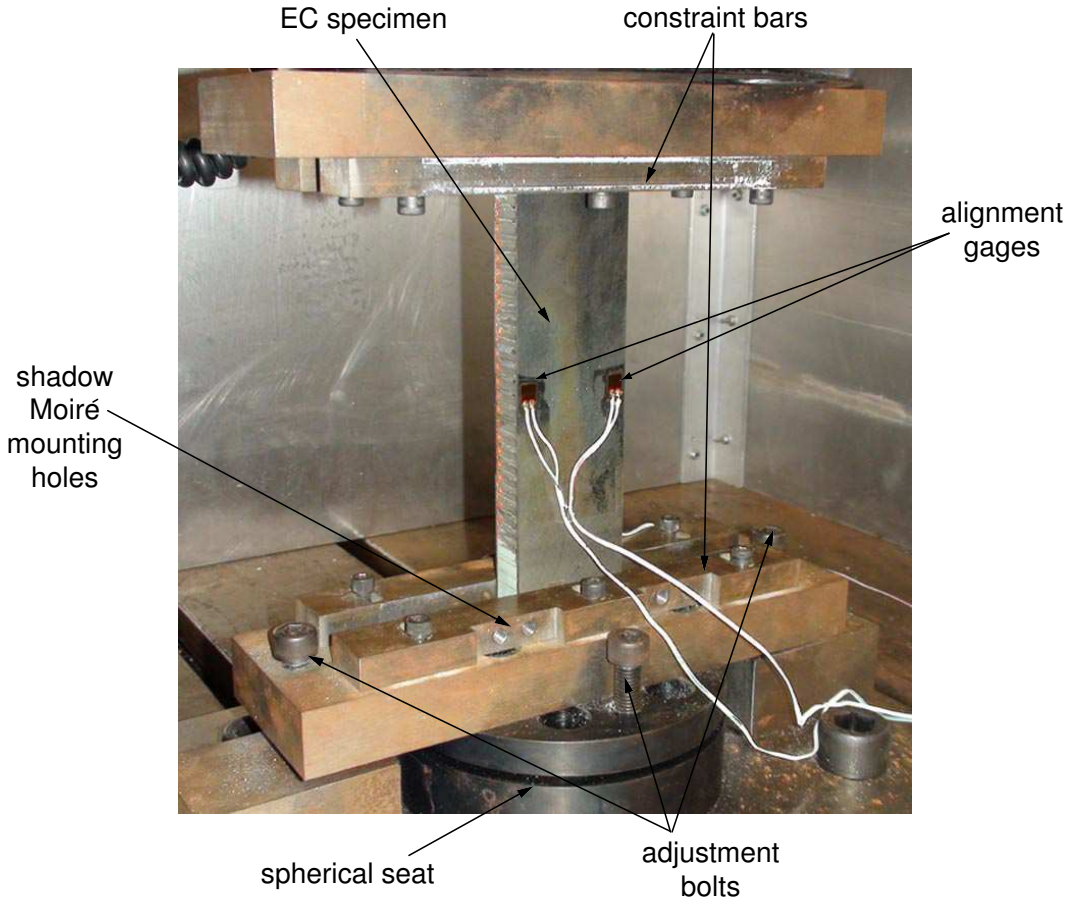

Figure 4.8: An EC specimen in the compression fixture.

placement location was determined with 18.0 or 26.9 mm wide (depending on panel thickness) alignment fixtures, and when necessary, additional set of steel shims.

As seen in Figure 4.9, an alignment fixture was first bolted in the exact center of the lower compression platen using the existing threaded holes for the left and right adjustment bolts. Next, the crosshead of the load frame was lowered until the upper compression platen made rigid contact with the top surface of the alignment fixture. The rear constraint bars were firmly pressed flush against the alignment fixture and bolted in place using three, 6.35 mm dia. Allen bolts.

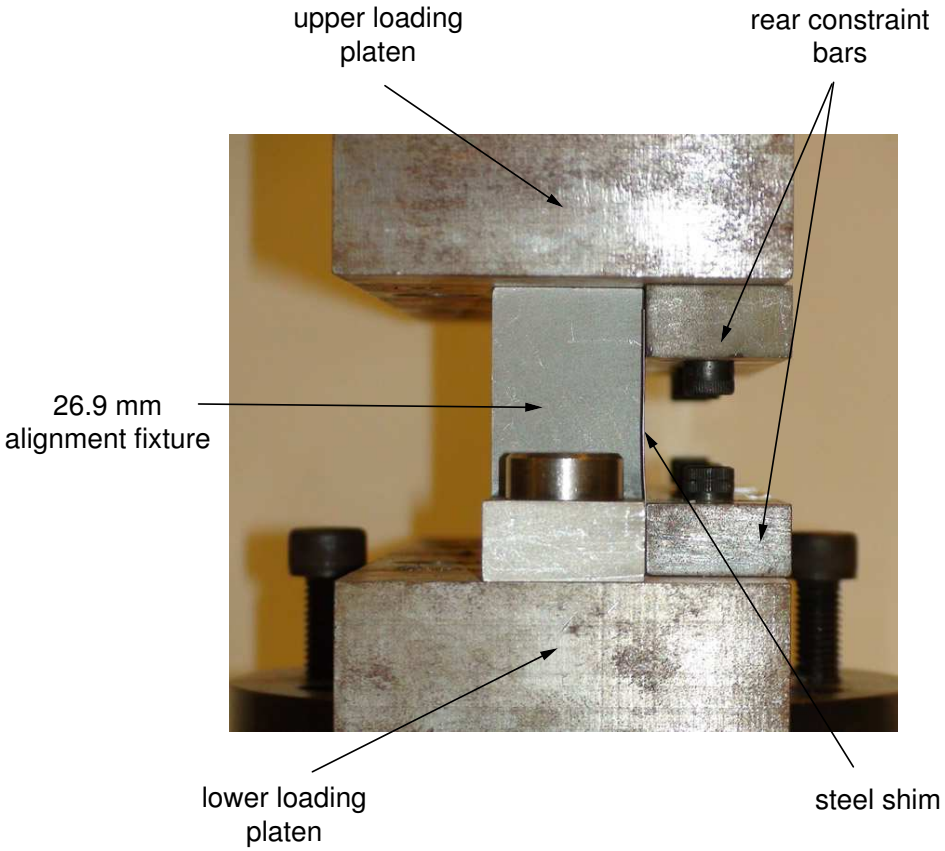

Figure 4.9: Side view of the specimen alignment fixture between the top and bottom compression platens.

In case a particular specimen was thicker than 18.0 or 26.9 mm (e.g. a 16 ply specimen) a set of steel shims was placed between the alignment fixture and the constraint bars to obtain the desired spacing. Once the rear constraint bars were securely fastened, the upper compression platen was raised, and the compression specimen was fixed inside of the fixture using front constraint bars.

4.2.5 Shadow Moiré

The evolution of the out-of-plane indentation damage during CAI was visualized using a shadow Moiré [63, 64]. As seen in Figures 4.7 and 4.10, the shadow Moiré setup consisted of a linear reference grating, a light source, and a high definition video camera. Three distinct reference gratings were used, all fabricated by Applied Image Inc. and printed on a 0.018 mm clear mylar film. The small diameter dents with depths of approximately 0.5 mm (25.4 mm dia. indentor QSI) were visualized using the 4.7 lines per mm (lpmm) grating, while dents with depths above 0.5 mm in depth (76.2 mm dia. indentor QSI) were visualized using the 2.4 or 3.5 lpmm grating.

Each reference grating was adhered to a 3.2 mm thick sheet of clear glass using a thin layer of distilled water. The glass sheet was designed to attach to the bottom-front constraint bar, placing the grating approximately 9.4 mm away from the indented surface of a CAI specimen. A high definition video camera (Sony HDR-SR11 - 10.2 mega pixels) was placed directly in front of the Moiré grating at a distance of approximately 63.5 cm. The light source, consisting of a 75 watt, clear incandescent, single filament, light bulb, was placed at a distance of 63.5 cm on a line perpendicular to the line of sight of the video camera. The 45 degree location of the light source to the Moiré grating resulted in a one-to-one relationship between the contour interval of the Moiré fringe pattern and the pitch of the reference grating [63, 64]. Prior to each test, the display of the shadow Moiré was nulled by aligning the surface of the Moiré grating with the undamaged regions of the indented face sheet.

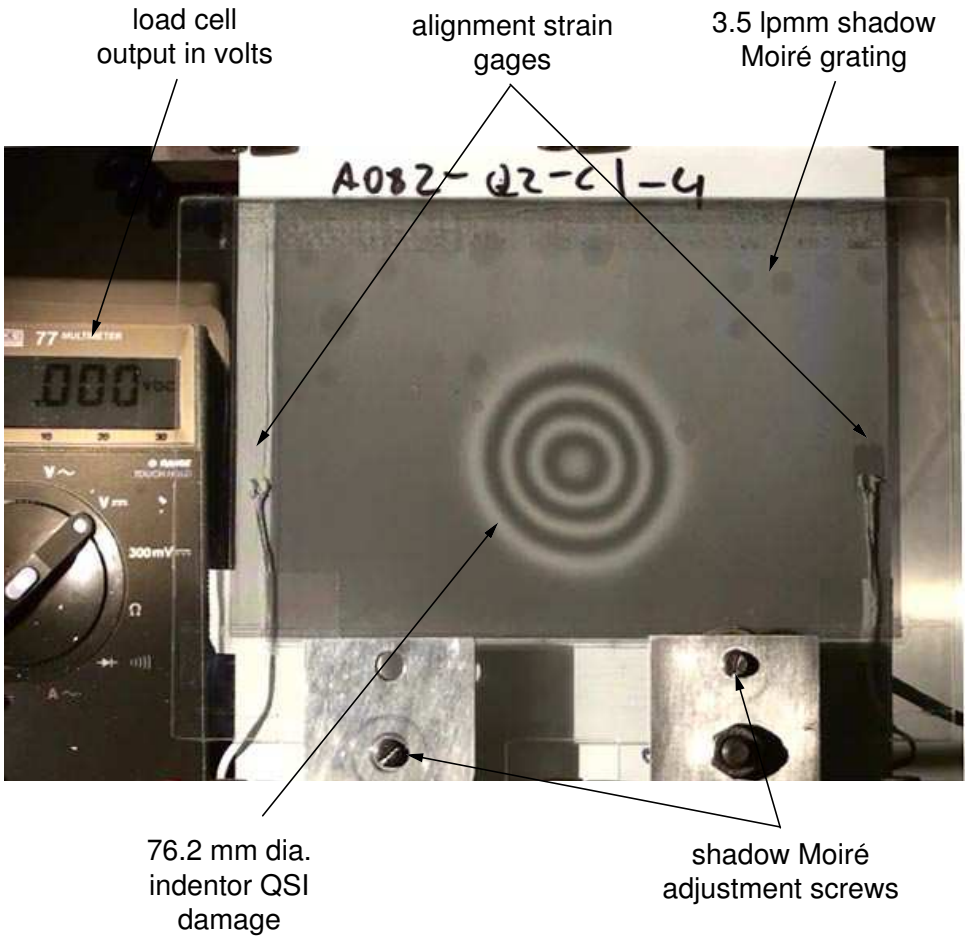

Figure 4.10: 3.5 lpmm shadow Moiré grating highlighting the QSI damage resulting from a 76.2 mm dia. indentor. Each pair of black and white fringes correspons to an out-of-plane displacement of 1/3.5 (0.28) mm.

4.2.6 Test Procedure

Prior to testing, all EC and CAI specimens were precisely measured to obtain their lengths, widths and thicknesses. The thickness measurements were performed in an un-potted region, at three different locations along each edge of the specimen. Each specimen was instrumented with four CAE-00-125UW-350,

350Ω, 3.2 mm gage length, Vishay Micro-Measurements strain gages. Two strain gages were mounted on each face sheet, midway between the loading edges, at a distance of 6.4 mm away from each free edge, and aligned with the loading direction (see Fig. 4.10) . All gages were adhered using Vishay's M-Bond 200 strain gage adhesive. The front face sheet of each CAI specimen was painted with several coats of flat white spray paint. For each test, the strain gages were shunt calibrated and zero-balanced using Calex MK 162 strain gage signal conditioners, and connected via Keithley Model 7700 multiplexing digital volt meter to Keithley's ExcelLINX data acquisition software. The data acquisition was performed by collecting signals from six channels (4 strain gages, cross-head position from a linear variable differential transformer (LVDT), and the load cell) at a rate of two data sets per second.

At the beginning of each EC or CAI test, the specimen was securely clamped inside of the test fixture, the spherical seat adjustment bolts loosened, and the upper platen manually lowered until it made contact with the upper part of the specimen. At that point, the data acquisition was initiated, and a steady compression force was applied to the specimen in displacement control at a rate of 0.005 mm/s to 2200-4400 N. Once this load range was obtained, the loading was halted, and the strain distribution in the face sheets (as indicated by four strain gages) was examined. In almost all instances, the settling of the specimen between the loading plates resulted in an uneven strain field. The four adjustment bolts were then appropriately tightened or loosened to equalize the strain readings. Once this was achieved, the specimen was further compressed to approximately double the previous load, and strain readings were once more equalized. The strain balancing was repeated once more, first by fully unloading the specimen, and then by compressing it for a third time to roughly 25-30

percent of the expected critical load.

At this point in the case of EC tests, once a uniform strain distribution was achieved, the specimen was again unloaded and the compression test was performed at a rate of 0.005 mm/s until failure. Failure was generally determined based on audible evidence or face sheet collapse and sudden drop in the applied compressive load.

In the CAI tests, before the specimen was unloaded from the third strain balancing step, a shadow Moiré grating was bolted to the bottom-front constraint bar, and the fringes nullified. The installation was done under load to prevent any potential misalignment of the specimen. The specimen was next unloaded, and then the compression test initiated at a rate of 0.005 mm/s. Once the compression load reached approximately 75 percent of the expected critical load, the load rate was reduced by a factor of four to 0.00125 mm/s. A slower loading rate allowed for improved observation of damage evolution prior to failure. A typical strain response of a CAI panel is presented in Figure 4.11, showing data from all four alignment gages. As seen in this figure, uniform strain distribution is maintained throughout the test.

4.2.7 Results

4.2.7.1 Undamaged Strength Results

The undamaged strength data were used to normalize the CAI results and determine the percentage strength reduction due to impact damage. The data were measured for each of the seven panel geometries using 17.8×5.1 cm EC speci-

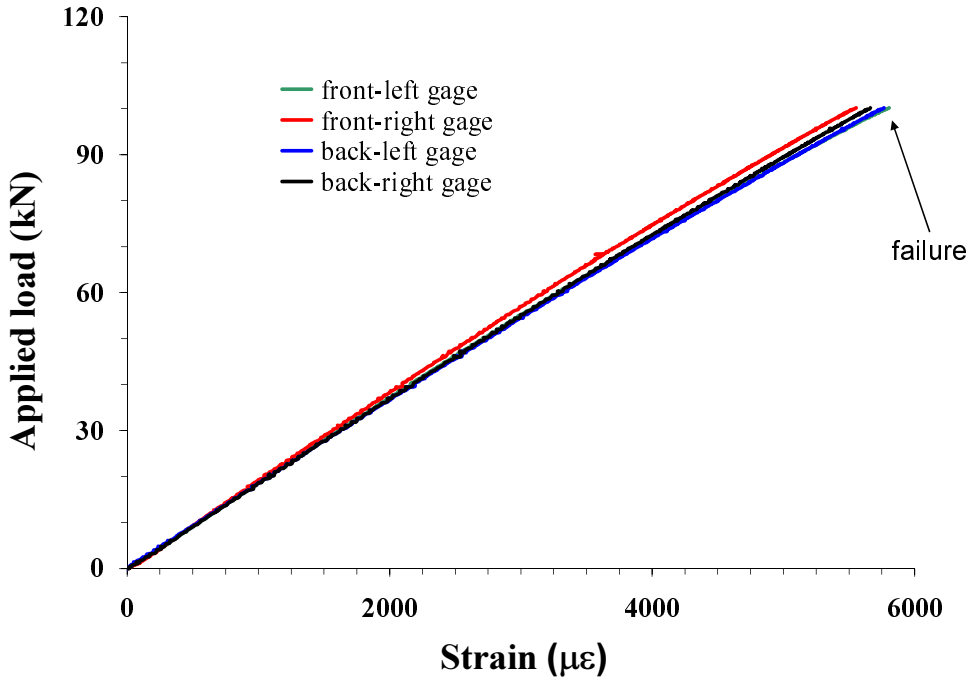

Figure 4.11: An example of CAI load versus strain data for Q1-C1 specimen indented with 76.2 mm dia. indentor.

mens. The small width specimens produced essentially the same results as the full size, 15.2 cm wide specimens, yet required less material.

For all compression tests, strength was defined as the applied compressive load at failure divided by the cross-sectional area of the two face sheets. To calculate the area, the width was measured directly. However, given the fabrication method and the final specimen geometry, the only viable way of determining total face sheet thickness was by measuring the total sandwich panel thickness and subtracting the core height. Examining this deduced thickness data for a series of specimens, a significant inter- and intra-panel thickness scatter was found. Without alternative means for a more accurate measure, it was determined that the best approach was to base the strength calculations for all specimens on a constant, double face sheet thickness of 2.032 mm, which is the

expected 16 ply thickness value provided by the pre-preg manufacturer [53]. Use of this single thickness value for all secimens removed a significant source of scatter and is equivalent to reporting failure in terms of face sheet edge load per unit width, (N_x).

Table 4.3: Summary of the undamaged compression strength data.

Layup-core	**Number of specimens tested**	**Average failure strength (MPa)**	**Range: Max-Min (MPa)**	**Variation: Range/Mean (%)**
Q1-C1	3	400	65.5	16.2
Q1-C2	4	348	29.0	8.4
Q1-C3	5	422	15.2	3.6
Q2-C1	3	444	11.0	25.0
Q3-C1	1	414	NA	NA
Q4-C2	1	436	NA	NA
Q4-C3	1	502	NA	NA

Results from the undamaged strength tests are summarized in Table 4.3 and detailed in Appendix A. In essentially all tests, failure initiated as a result of micro-buckling and/or shear failure of the load-bearing, 0° plies, followed by fracture of the remaining plies in the direction perpendicular to the loading direction [65]. Examining the data for any given specimen type, there is reasonably large specimen-to-specimen variation, which is observed to be larger when specimens come from different panels than when specimens are cut from the same panel. Thus, although the trends in Table 4.3 are expected to be qualitatively accurate, in view of the scatter and the small sample size, they must be considered as provisional. That is, any quantitative comparisons about the relative strengths of the various specimen types could vary with number of samples

tested and associated panel manufacturing.

Nonetheless, results in Table 4.3 indicate that the undamaged strength increases with increasing core density (Q1-C1 vs Q1-C3) and core thickness (Q1-C2 vs Q1-C1). The Q1 and Q3 layups have approximately the same strength (Q1-C1 and Q3-C1), and the Q2 and Q4 layups are slightly stronger. The results in Table 4.3 are somewhat surprising, because with all things being equal, one would expect the compressive strength to be independent of core type and layup. That is, in terms of the axial response, the Q1-Q4 layups have the same number of plies aligned with the 0/45/90 degree axis and are expected to behave identically.

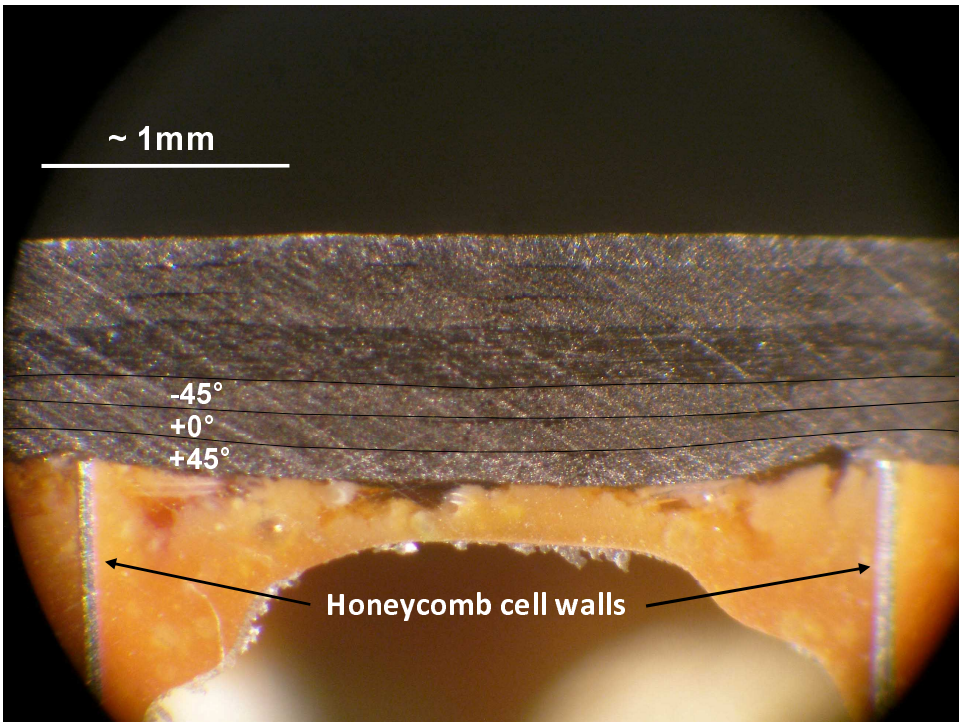

Figure 4.12: Cross-sectional view of the Q1 face sheet co-cured to C1 aluminum honeycomb core. The solid black lines are used to highlight the waviness of the bottom three plies.

Some of the observed differences are related to scatter and the inherent na-

ture of imperfection-sensitive compression testing. As an example, it is possible that panels with the thin, C2 core are increasingly susceptible to misalignment, and hence tend to fail at lower loads. Similarly, the significant difference between the Q1 and Q2-Q4 layups (Q1-C1 vs Q2-C1, Q1-C1 vs Q3-C1, Q1-C2 vs Q4-C2, and Q1-C3 vs Q4-C3) can be related to the stacking sequence and the sandwich panel fabrication method. As evident from Figure 4.12, which shows a typical cross-section view of a sandwich specimen, the co-curing method results in a significant waviness of the plies near the core/face-sheet interface. In the case of eight-ply face sheets, the fiber waviness extends into approximately 2-3 inner face sheet plies. Considering the stacking sequence of the Q1 layup, the fiber waviness affects one of the two load-bearing, 0° plies, perhaps initiating onset of fiber micro-buckling at lower loads.

4.2.7.2 Damage Tolerance Results

A complete description of the CAI data is presented in Tables C.1 and C.2 of the Appendix. The same data are summarized graphically in terms of strength and percent strength reduction in Figures 4.13-4.21. In Figures 4.13 and 4.14, strength and residual strength is presented as a function of QSI dent depth, and in Figures 4.20 and 4.21 as a function of planar delamination area. The planar delamination area in Figures 4.20 and 4.21 is defined as an overall projection area of all delaminations. As described previously, delamination area could not be accurately measured for dents from 76.2 mm dia. indentor, and hence this data was excluded from Figures 4.20 and 4.21. In each figure, the distinct symbol shapes represent each of the four face sheet layups, while the color scheme identifies the three core types.

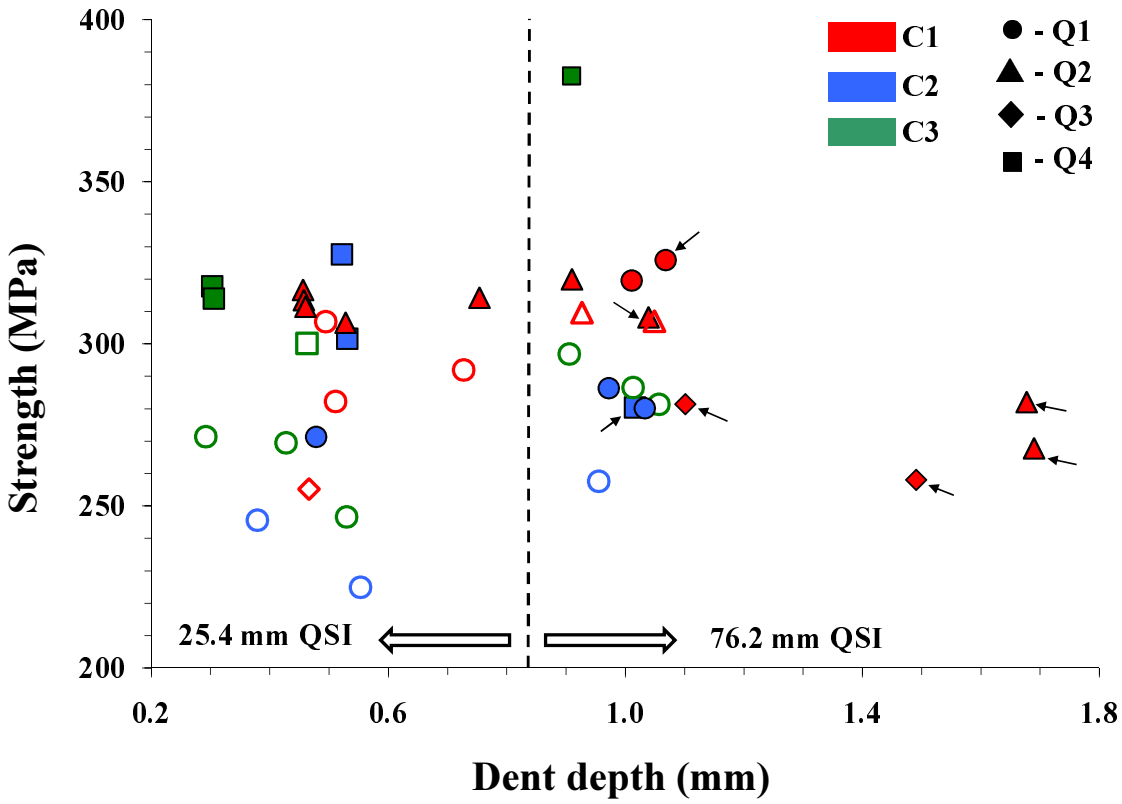

Figure 4.13: The CAI strength versus dent depth. The dashed horizontal line divides the 25.4 mm and 76.2 mm indentor dia. data. Solid symbols correspond to specimens failing due to fiber failure, open symbols correspond to specimens exhibiting delamination buckling, and arrows designate specimens failing due to unstable dent growth and global instability.

In addition to strength data, a sequence of photos captured using the shadow Moiré setup provided visual evidence of damage evolution during compression. Based on the image analysis, an example of which is shown in Figures 4.15-4.17), three distinct sequences of damage evolution and ultimate catastrophic failure modes were observed. For all specimens tested, regardless of panel type or initial dent size, evolution of damage during compression always initiated with progressive dent deepening as evident by an increase in the Moiré fringe count. For all subsequent discussion this process will be referred to as dent

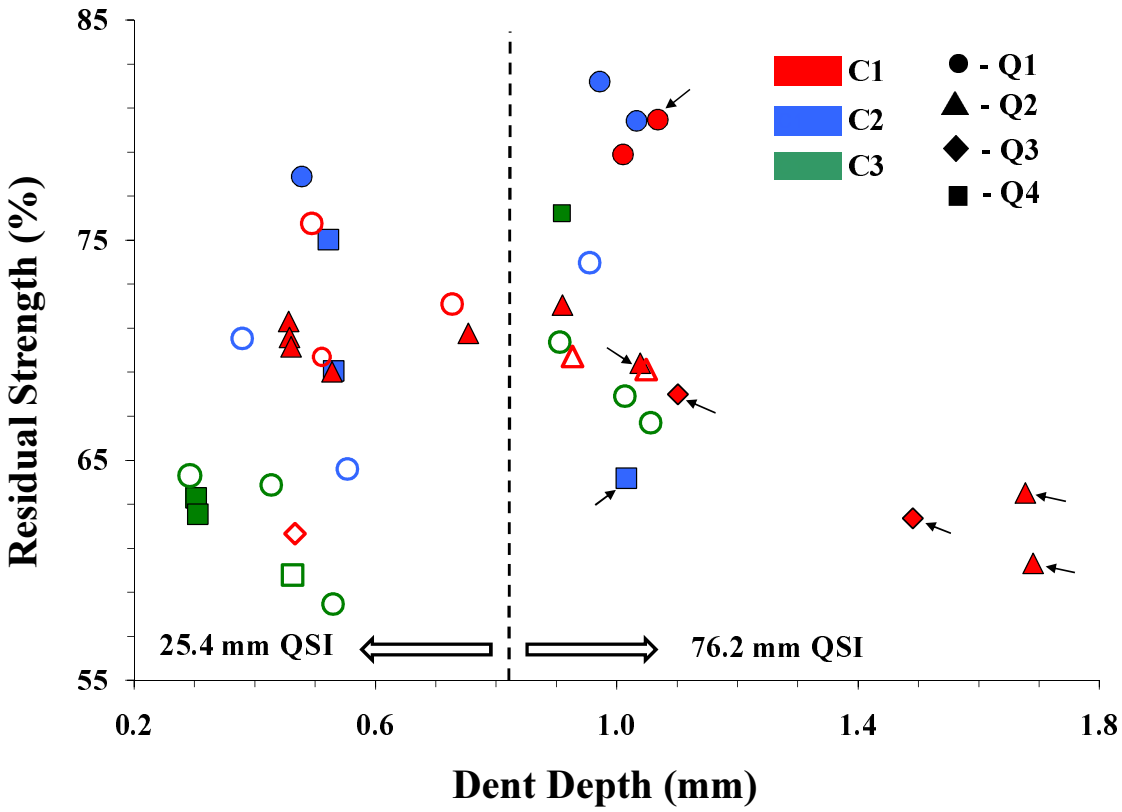

Figure 4.14: The CAI strength versus dent depth.

growth (DG).

In some specimens, the continuous DG lead to an increase in the face sheet bending stresses, promoting flexural microbuckling of the load carrying, 0° plies [65]. As the critical compressive load was approached, the low out-of-plane support from surrounding plies resulted in an unstable microbuckling of load carrying plies, causing a catastrophic compressive fiber failure (FF) (Figs. 4.15-4.16).

In a number of specimens, during DG, a progressive out-of-plane buckling of interlaminar delaminations was observed (Figs. 4.17 and 4.18). In all such cases, the buckled regions originated above or below the dent, becoming in-

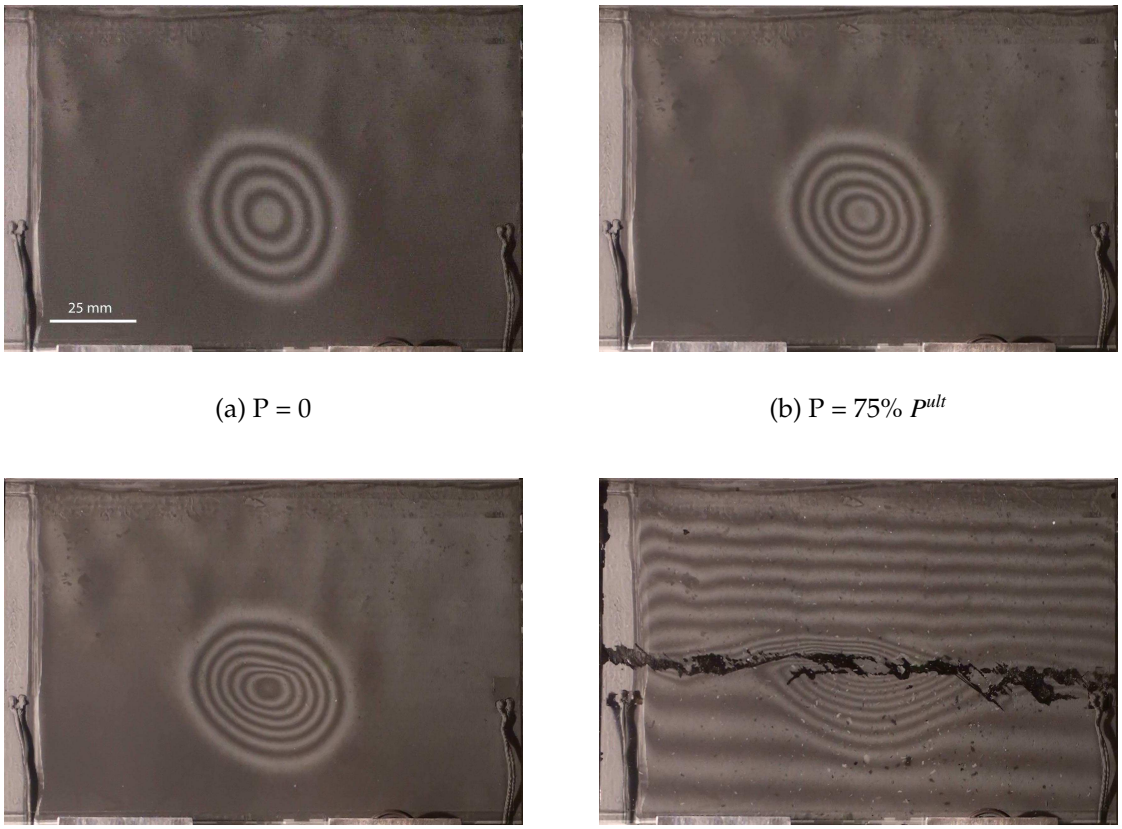

(a) P = 0

(b) P = 75% P^{ult}

(c) P = 99% P^{ult}

(d) failure

Figure 4.15: Example of dent growth and fiber failure during compression after impact of a Q1-C1 specimen with QSI damage from 76.2 mm dia. indentor (3.5 lpmm Shadow Moiré).

creasingly visible at high percentages of failure stress. The catastrophic failure of specimens exhibiting delamination buckling (DB) generally occurred due to the combined effects of DG, sudden increase in deflection of the delaminated region, unstable delamination growth, and fiber failure.

Finally, in specimens with relatively deep dents from QSI using the 76.2 mm dia. indentor, DG became gradually unstable, rapidly expanding as an elongated ellipse in the direction perpendicular to the load direction. Upon reaching the free edges of the specimen, the unstably growing dent caused global insta-

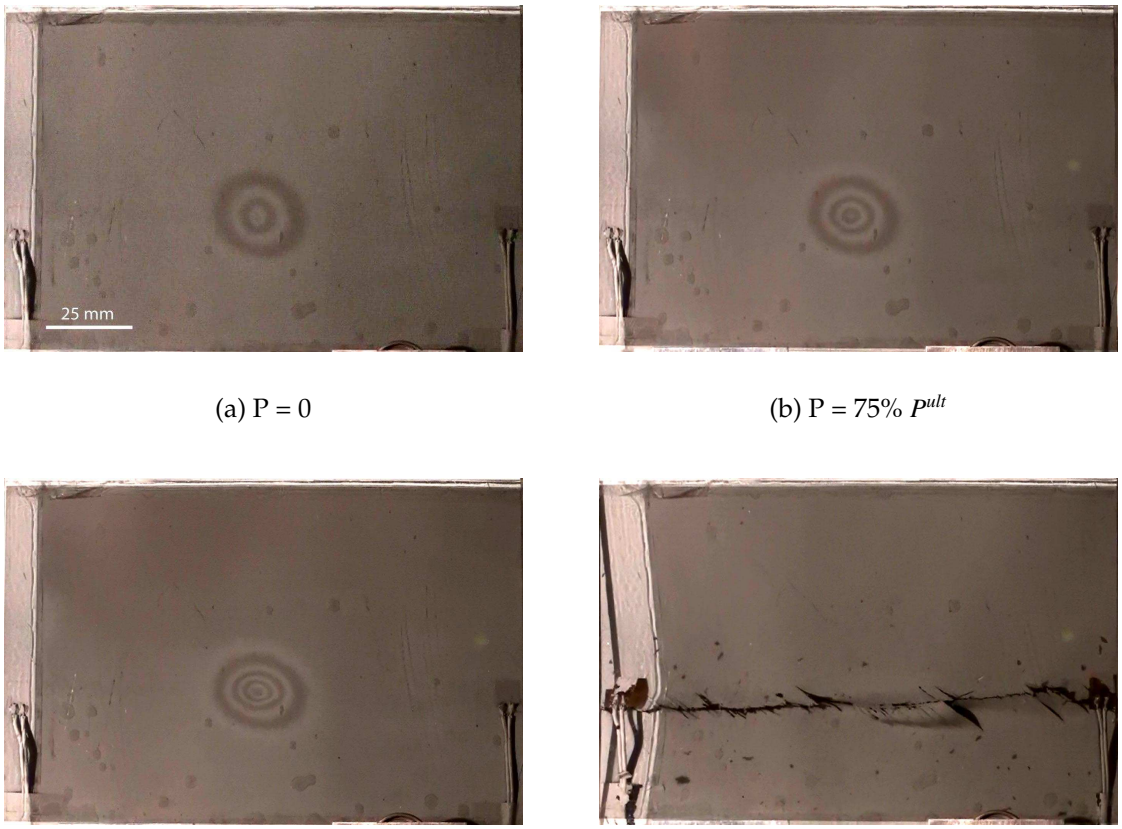

(a) P = 0

(b) P = 75% P^{ult}

(c) P = 99% P^{ult}

(d) failure

Figure 4.16: Example of dent growth and fiber failure during compression after impact of a Q4-C2 specimen with QSI damage from 25.4 mm dia. indentor (4.7 lpmm Shadow Moiré).

bility (GI) of the indented face sheet, resulting in catastrophic failure. The three modes of failure described here are represented in Figures 4.13-4.21, where all solid symbols represent specimens failing due to DG and FF, and open symbols represent those that failed due to combination of DG, DB and FF. The 76.2 mm dia. "high QSI load" specimens that failed due to unstable DG and GI are marked with individual arrows.

Examining Figure 4.13, for a given specimen type and QSI indentor diameter, the CAI strength generally remains essentially constant (Q1-C1 and Q2-C1)

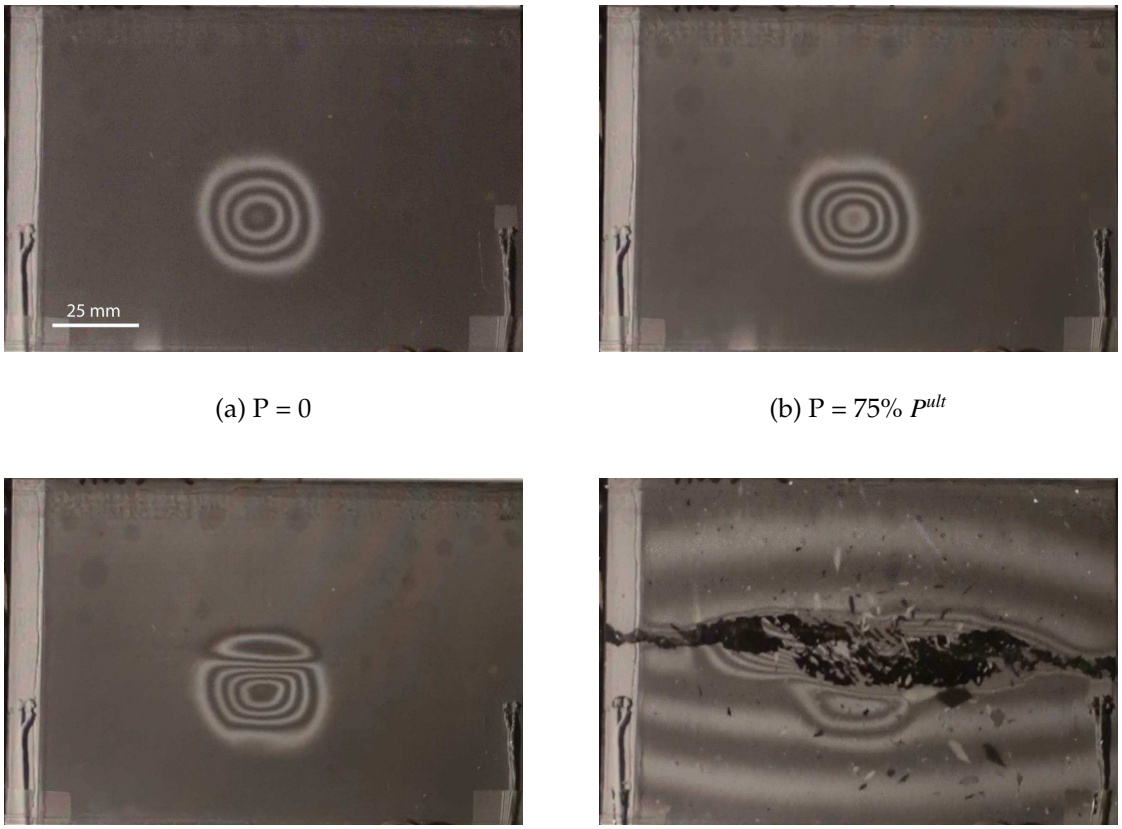

(a) P = 0

(b) P = 75% P^{ult}

(c) P = 99% P^{ult}

(d) failure

Figure 4.17: Example of delamination buckling and fiber failure during CAI of a Q1-C3 specimen with QSI damage from 76.2 mm dia. indentor (3.5 lpmm Shadow Moiré).

or decreases with increasing dent depth. The primary exception to this trend appears to be the Q1-C2 samples which is likely due to different modes of failure observed for that configuration. Figure 4.13 indicates that there are competing failure modes and, taking note of Figure 4.20 data, it can be observed that the mode that controls final failure will be dictated by the damage (dent and delamination), the layup of the face sheets, and the type of core.

Note that for specimens indented with the 25.4 mm dia. indentor, all but one specimen (solid Q1-C2) with Q1 face sheets exhibited delamination buckling

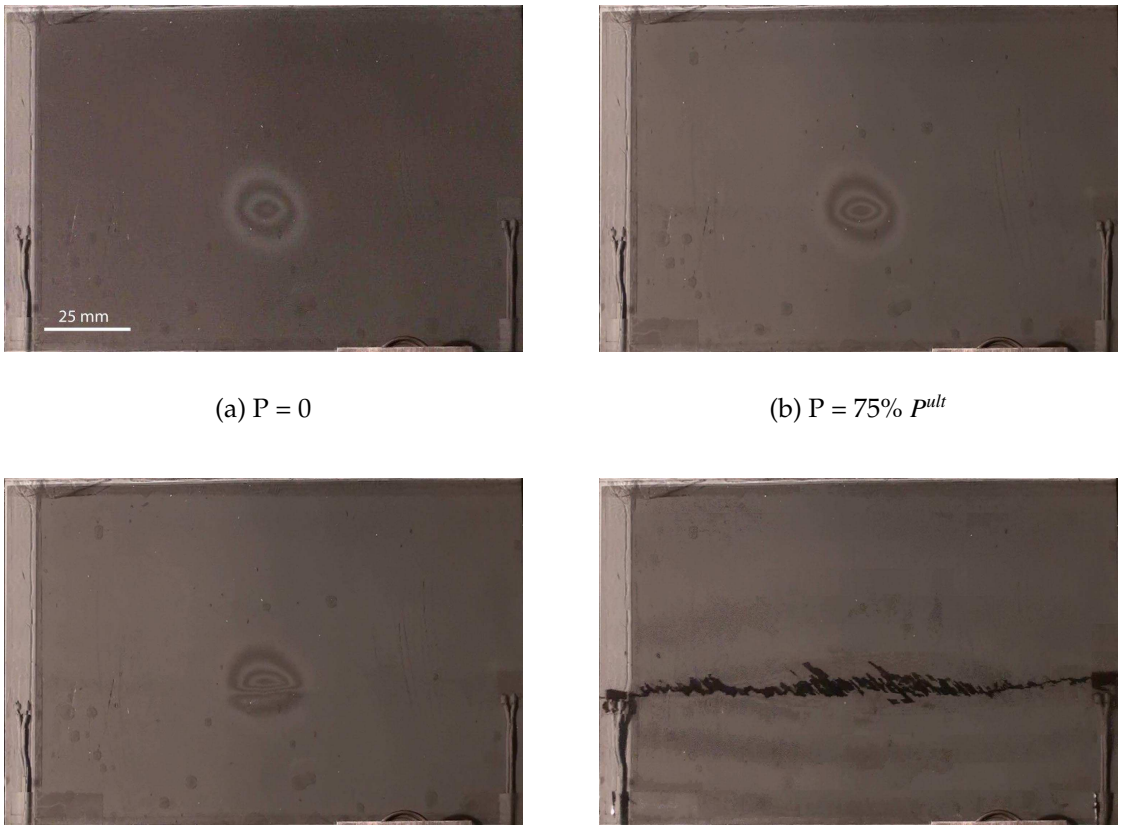

(a) P = 0

(b) P = 75% P^{ult}

(c) P = 99% P^{ult}

(d) failure

Figure 4.18: Example of delamination buckling and fiber failure during CAI of a Q1-C3 specimen with QSI damage from 25.4 mm dia. indentor (4.7 lpmm Shadow Moiré).

during failure, and the Q1 layup shows the greatest propensity for DB for all indentor diameters. Interestingly, the results in [58] suggest that the Q1 and Q4 layups were the most delamination resistant; that is, they showed the smallest delaminated areas of all layups for a given QSI event.

The increased propensity for DB in the Q1 face sheet can be explained by the proximity of the 0° ply to the free surface and the resulting increased stiffness of the delaminated region in comparison to those of the other layups. Generally a stiff delamination will attract more load making it more prone to buck-

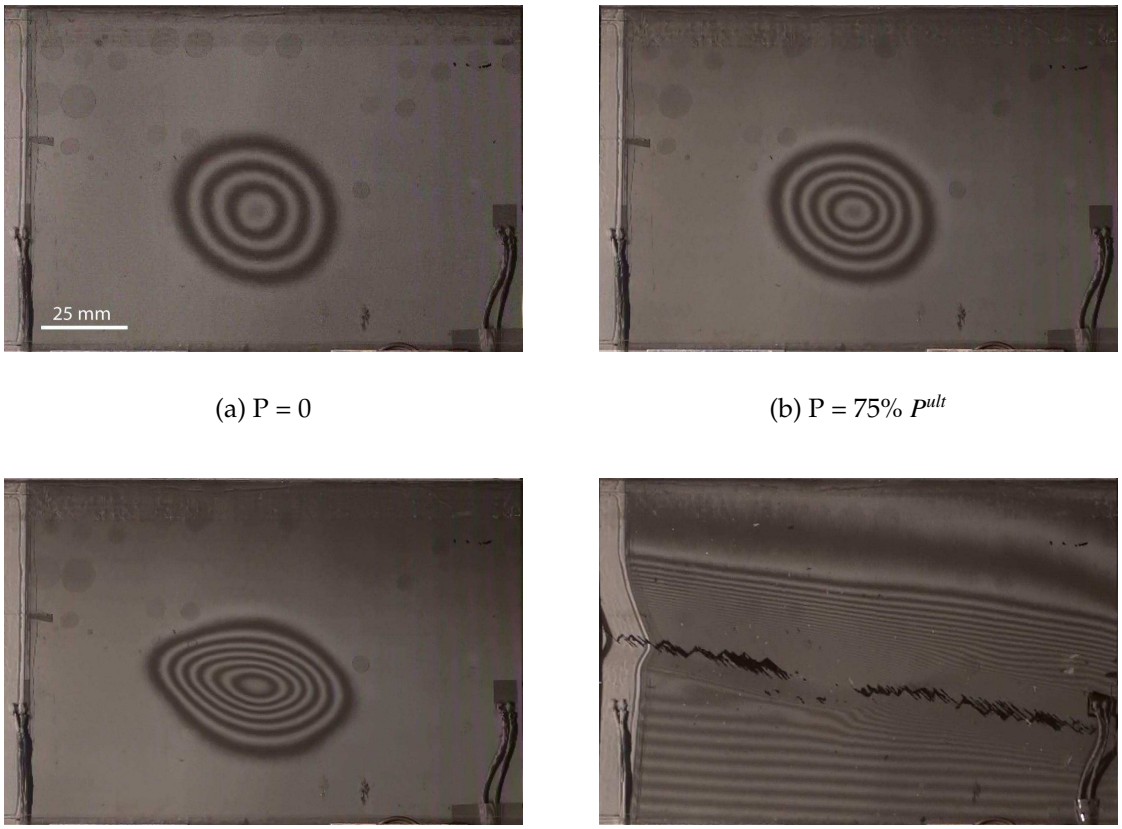

(a) P = 0

(b) P = 75% P^{ult}

(c) P = 99% P^{ult}

(d) failure

Figure 4.19: Example of unstable dent growth and global instability during CAI of a Q4-C2 specimen with QSI damage from 76.2 mm dia. indentor (3.5 lpmm Shadow Moiré).

ling. Those specimens that exhibited DB with other face sheet layups always corresponded to cases where the delaminations were quite large. For example, the single Q4 layup that shows DB in Figure 4.13 corresponds to the specimen where a QSI force of 1730 N was used and which, therefore, produced a very large delamination (Fig. 4.20). Note from Figure 4.20 that the Q3-C1 specimen that showed DB also had a very large delamination. Figure 4.13 shows that DB is less likely to occur in specimens indented with the 76.2 mm dia. indentor, which have large dent depths, than for the specimens indented with the 25.4 mm dia. indentor. Failures by DG and FF are associated with higher

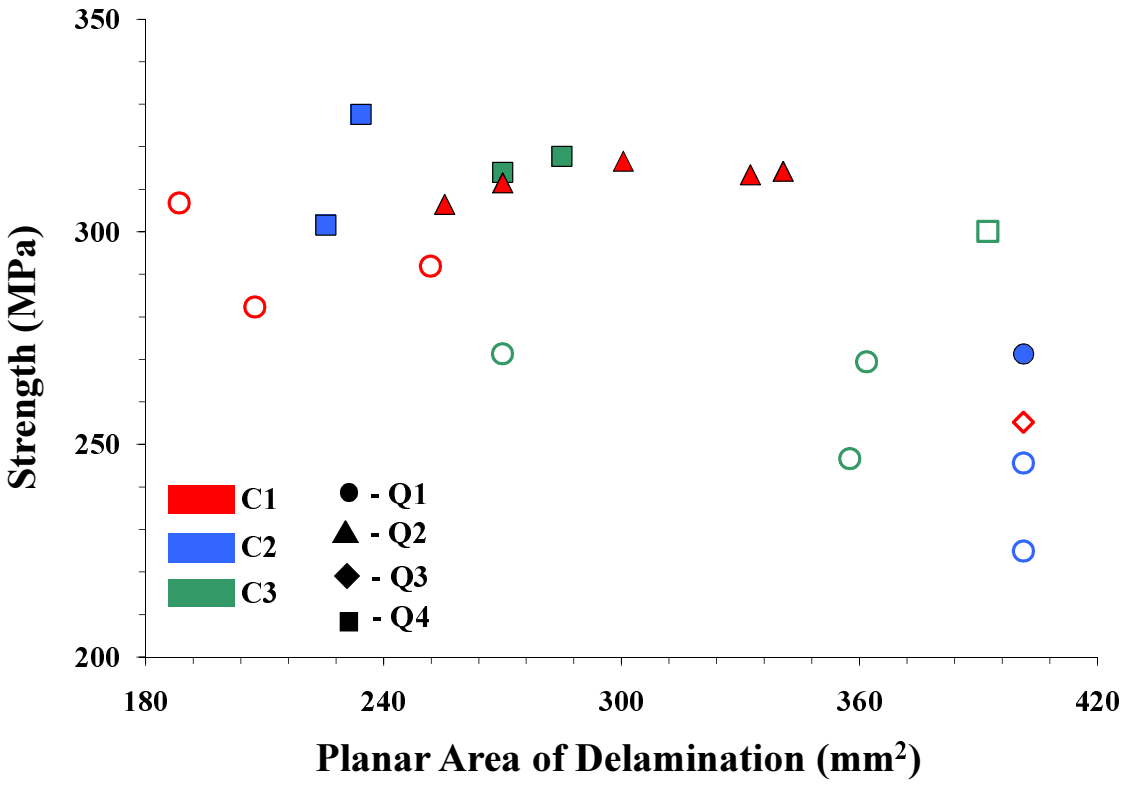

Figure 4.20: The CAI strength versus dent depth. The data for dents from 76.2 mm dia. indentor is not included.

strengths than DB-induced failures, and this failure mode transition across the indentor size partially explains the higher residual strength for Q1-C1 specimens indented with 76.2 mm dia. indentors in comparison to those indented with 25.4 mm dia. indentors. However, considering all specimen types, regardless of whether or not a failure mode transition occurs, the residual strength in specimens indented with large diameter indentors is generally higher than for those indented with small diameter indentors (Fig. 4.14). The exceptions are Q2-C1, for which strength is essentially constant until the dents are quite large, and Q4-C2, which is the only specimen type where the residual strength is lower for indentation due to large diameter indentor.

Comparing the results for Q1-C1 and Q1-C3, the higher density C3 core gives

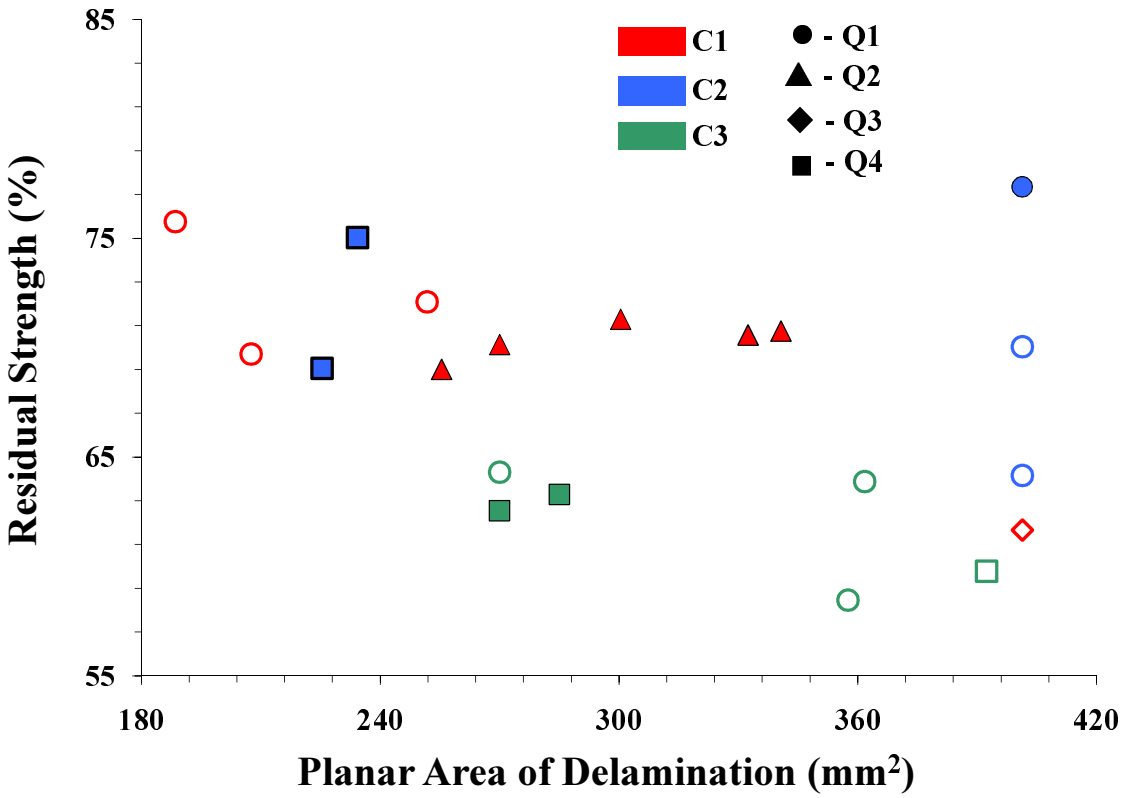

Figure 4.21: The CAI strength versus dent depth. The data for dents from 76.2 mm dia. indentor is not included.

a slightly larger undamaged strength (Table 4.3) but the CAI strength of Q1-C3 is always lower (Fig. 4.13). This is due to the larger delaminated area in this specimen type (Fig. 4.20). Thus, from a damage tolerance viewpoint, there is no reason to use the higher weight C3 core. Considering the effectiveness of the various face sheets, it was found that Q1 and Q4 showed less delamination than Q2 and Q3. Q4 shows a higher undamaged strength than Q1 (Table 4.3). As previously mentioned, this may be related to the waviness of the inner portion of the face sheet, thereby reducing the effect of the innermost 0° ply in the Q1 layup. Also, the outer 0° ply in the Q1 layup makes Q1 more prone to DB than Q4. The result (Fig. 4.20) is that the CAI strengths of Q4-C3 and Q4-C2 are generally larger than those of Q1-C3 and Q1-C2, respectively, making Q4 a better

overall choice. Interestingly, Q2, although showing relatively large delaminations (see Fig. 4.20) shows the most consistent CAI performance with a CAI strength that is virtually independent of the QSI event until very large (easily observable) dents are created. It also shows a large undamaged strength. Thus, the "rule of thumb" that says that it is best to put ±45° plies on the outside of a laminate, even if it means that there will be more subsequent 90° angle changes, appears to be validated by our data.

4.3 Modeling

4.3.1 Modeling Preliminaries

The second part of this investigation describes the development of a numerical model for assessing damage tolerance of composite sandwich structures. The primary objective of this model was to provide further insight into the experimentally observed failure of impact-damaged specimens and, in particular, to study the effects of unstable dent growth, delamination buckling, and compressive fiber failure on residual strength. Ultimately, this study intends to provide a robust and computationally efficient numerical tool that can be used for design and parametric study.

An additional motivation of the current modeling efforts was to improve upon the existing analysis methods. To date, the numerical models of CAI assumed an initial state of impact damage, thereby neglecting many of the complex damage mechanisms that arise during QSI. Some of these damage mechanisms include delamination and residual stresses in the core and face sheets.

With this in mind, the current approach explicitly simulates QSI and the associated damage mechanisms. By explicitly simulating QSI, the history of the cumulative damage processes that occur during the impact/indentation event are inherently incorporated into the CAI simulation.

To accurately simulate the evolution of damage from the moment of impact through ultimate panel failure during compression, a number of failure mechanisms had to be considered. Based on the non-destructive and destructive evaluation of specimens prior to and during QSI and CAI testing, the fundamental failure mechanisms were classified according to their location. Localized, through-thickness core crushing was the primary damage mechanism of concern for the honeycomb core. In the case of the impacted face sheet, the critical failure mechanisms included the intra-laminar fiber/matrix failure and inter- and intra-ply delamination. Additionally, the mechanisms of face-sheet/core debonding should generally be considered, although in the present experiments this process was not explicitly observed.

Given the potential difficulties involved in modeling of each failure mechanism, the approach of this numerical study was to consider the least complex failure mechanisms first. With this in mind, the numerical efforts focused on simulating the process of honeycomb core crushing and face sheet compressive fiber failure. To allow for expansion, the finite element model was structured to allow for incorporation of interlaminar delaminations. The simulation efforts were primarily focused on the baseline, Q1-C1 panel geometry. Among all of the panel geometries tested, the Q1-C1 geometry exhibited each of the three major modes of failure, making it an ideal case study.

To broaden the applicability of the proposed model, the development was

fully encompassed within the framework of FE analysis, and implemented in the commercially available Abaqus® software. To facilitate future extension of the the model to dynamic analysis of impact, the numerical integration was performed using an explicit dynamic formulation. The geometry of the sandwich panel was represented as an idealized QSI/CAI test specimen. The specimen geometry consisted of top and bottom face sheets and the honeycomb core. The evolution of core crushing was examined by employing two distinct honeycomb core damage models. In the first model, the core geometry was homogenized into a three-dimensional, orthotropic, compressible, elastic-plastic solid. In the second model, the hexagonal core geometry was explicitly represented using elastic-plastic shell elements. The in-plane, compressive failure of the impacted face sheet was simulated by incorporating a progressive lamina damage model.

The following sections detail the proposed damage models and the experimental material property testing required for model implementation. The sandwich panel model development is presented next, followed by simulation results of QSI and CAI.

4.3.2 The Honeycomb Core Models

4.3.2.1 Homogenized Honeycomb Core Model

The first of two honeycomb core models explored in this study was based on a homogenization of the core geometry into a three-dimensional, orthotropic, elastic-plastic solid [66, 67]. The model formulation was based on Hill's plasticity theory for orthotropic, incompressible materials [68] where the requirement for incompressibility was removed to account for deformation of cellular mate-

rials.

The material model was implemented in [66, 67] through a user-defined, ABAQSU/Explicit VUMAT code. To fully define the inelastic orthotropic behavior of the core, the model required six independent, experimentally determined stress-strain curves—three from uni-axial stressing, two from out-of-plane shear and one from in-plane shear. In the case of QSI/CAI simulation the critical hardening functions included the uni-axial compression in the thickness direction, $\sigma_{33} = f(\epsilon_{33})$, and out-of-plane shear in the ribbon direction, $\tau_{13} = f(\gamma_{13})$. In this study the two functions were determined experimentally, as described in Sections 4.3.4.2 and 4.3.4.3. The parameters describing the out-of-plane shear behavior in the direction perpendicular to ribbon direction, $\tau_{23} = f(\gamma_{23})$, were estimated based on the ribbon-direction data and Ref. [69]. The remaining less critical parameters were estimated from [70]. A summary of all VUMAT input parameters is graphically presented in Figure D.1 of the Appendix.

4.3.2.2 Explicit Geometry Honeycomb Core Model

The idea of explicitly representing the honeycomb core geometry using FE has been proposed in several studies [66,67,71–76]. Generally, due to small cell wall thickness with respect to other dimensions, core deformation is represented using thin, linear elastic or inelastic shell elements. Limited by the extremely high number of small elements necessary to capture large deformation gradients during core crushing, early modeling attempts by others focused on modeling only the elastic response. For example, in [71] the geometrically explicit core model with relatively coarse, elastic shell elements was used to compute the energy

release rate during face-sheet/core debonding of sandwich panels. Similarly, in [73,74] an ABAQUS® sandwich model with aluminum face sheets and aluminum core was proposed to simulate low-velocity impact and the resulting damage. Additionally in several references, honeycomb models containing one to eight unit cells with highly refined inelastic mesh were used to simulate large compressive and shear deformations and cell wall collapse [66,67,72]. In recent years, authors of [75,76] exploited a significant improvement in computational efficiency, and extended the unit cell approach proposed in [66,67,72] to larger geometries containing multiple cells.

In this study, the approaches proposed in [66, 67, 71–76] are used as an alternative to homogenized models for simulating core damage resulting from QSI and CAI. The model development herein was based primarily on [75, 76] and validated with simulation of flatwise compression. An image of a generic 25×25×25 mm C1 core geometry model is presented in Figure 4.22.

The honeycomb geometry was created by first constructing a two-dimensional hexagonal unit-cell (seen on the right in Figure 4.22) and repeating it to construct the desired cross-sectional area. The area was then extruded in the thickness direction to create a full three-dimensional model. The geometry was discretized, as seen in Figure 4.23, using 0.16×0.16 mm square, four-noded, linear S4RS shell elements with small membrane strains and a bi-linear hardening, J_2 plasticity, constitutive model.

To create a realistic representation of the cell walls and improve the overall performance of the model, geometrical imperfections were introduced into the mesh using random perturbation of the in-plane nodal coordinates of all elements by a magnitude ranging between ± 0.0178 mm [75,76]. The shell element

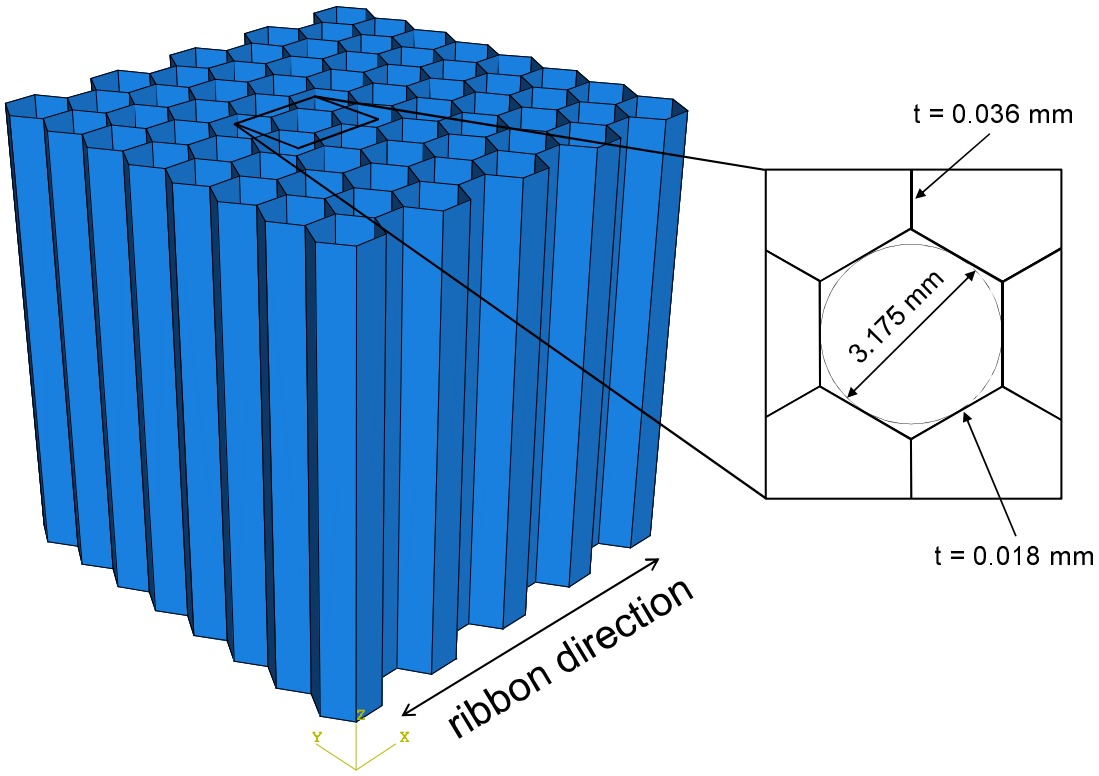

Figure 4.22: C1 core geometry model.

thickness was 0.0178 mm, based on the aluminum foil thickness listed by the manufacturer. In the regions where the corrugated sheets were adhered to create a hexagonal cross-section pattern, the wall thickness was doubled to 0.0356 mm. An elastic-plastic behavior of 5052-H39 aluminum alloy was assumed for all core elements. The material properties were estimated based on available data for 5052-H38 aluminum alloy [77] having elastic modulus of 70 GPa, yield stress of 220 MPa, stress of 282 MPa at one percent, and constant flow stress thereafter.

A general-contact algorithm with ”hard” normal-direction contact property was established between all the surfaces of the honeycomb core [78] to prevent unrealistic wall overlap during cell wall folding at large compressive strain lev-

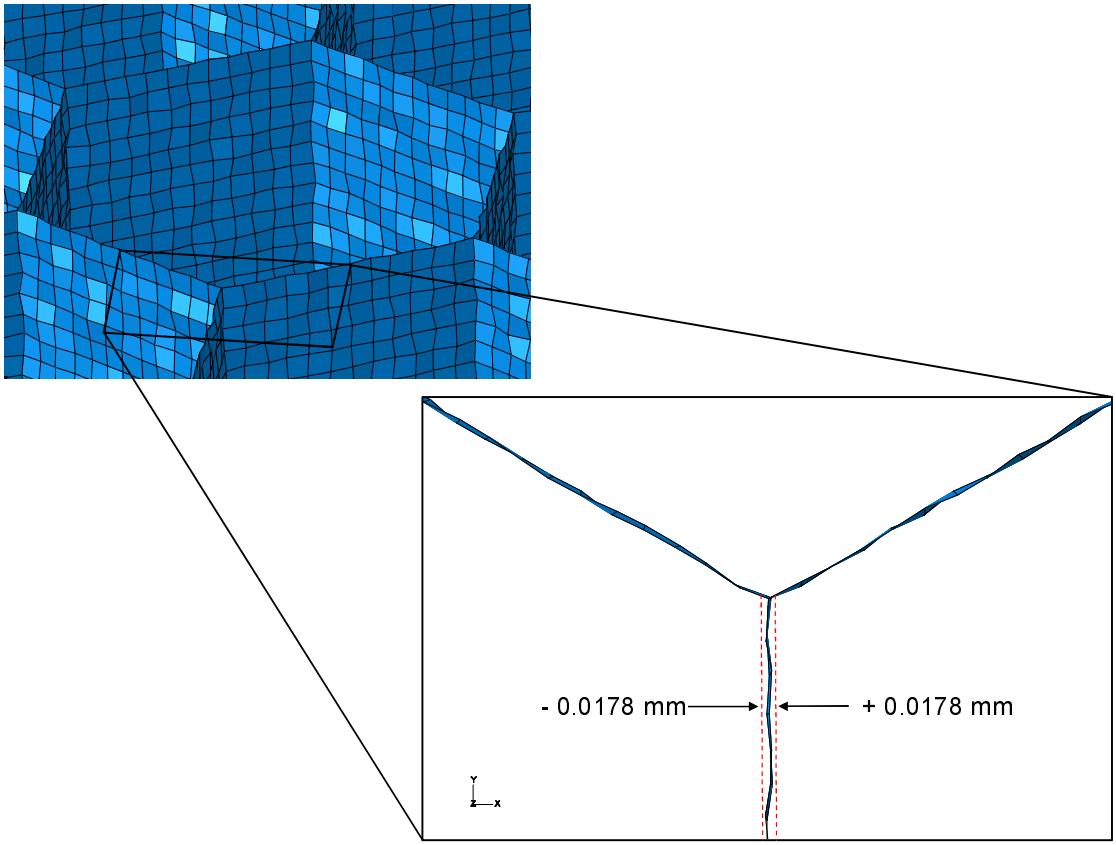

Figure 4.23: Honeycomb core geometry with random geometrical imperfections and discretization using S4RS shell elements.

els. To account for the expected structural softening and large amount of contact in the core during crushing, an explicit integration scheme (ABAQUS/Explicit) was utilized. To avoid long computation time needed to achieve a state of quasi-isotropic loading, the element mass was scaled to increase the critical time step during integration. The inertial effects due to mass scaling were kept small by ensuring that the kinetic energy of the model was small compared to the total energy [78].

In the proposed core model, the mesh density was determined based on a convergence study analogous to the one presented in [76], by simulating the

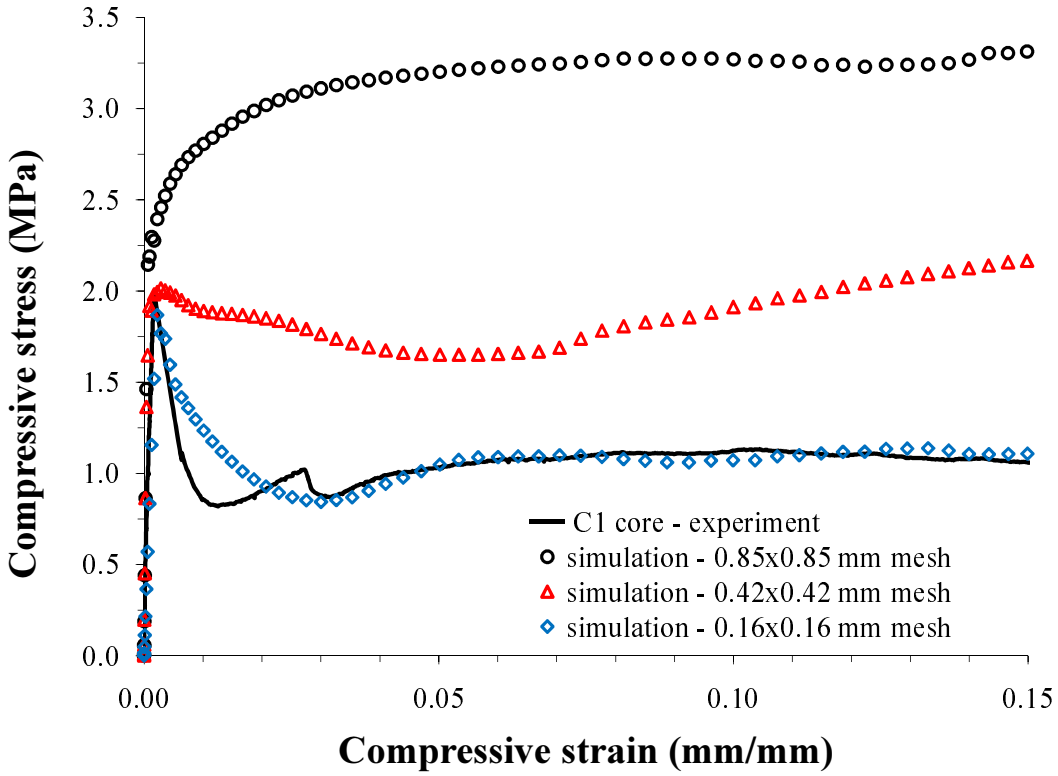

Figure 4.24: Results of mesh convergence study - C1 core geometry.

flatwise compression test (described in Section 4.3.4.2). The mesh convergence study was performed on the core geometry seen in Figure 4.22 under a quasi-static compression loading. The results of the convergence study are presented in Figure 4.24. As expected, the initial elastic response of the core was insensitive to mesh size, but the relatively coarse mesh (0.85×0.85 mm) resulted in an unrealistically high peak stress and a stiffening response after initial cell wall collapse. Gradual reduction of mesh size lowered the peak stress and the model simulated the expected post-yield softening and crushing at a constant stress level. The converged solution with the 0.16×0.16 mm square mesh was compared to the experimental data for C1 and C3 cores in Figure 4.25. In both cases, the numerical results showed an excellent agreement with the experiment. In each simulation stress in the shell elements at the onset of wall collapse was ap-

proximately half the yield stress of 5052-H39 aluminum alloy, suggesting that failure initiated by elastic buckling.

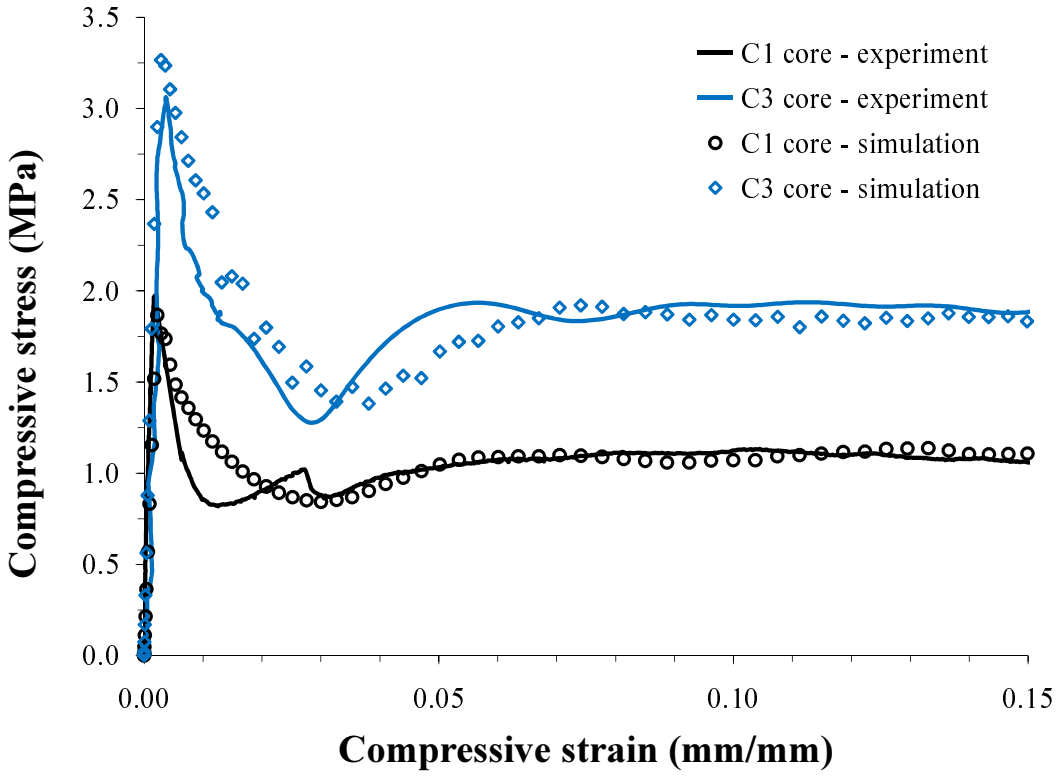

Figure 4.25: Crush response of C1 and C3 honeycomb cores - experiment versus simulation (experimental results described in Section 4.3.4.2).

The final step of model development focused on optimizing the computational performance by decreasing the number of shell elements needed to accurately capture the extent of core crushing during QSI and CAI. More specifically, a "hybrid" model was developed where regions of the core most likely to undergo crushing were represented explicitly, while regions away from damage zone were homogenized using three-dimensional, linear elastic, orthotropic brick elements.

The idea of using explicit core geometry "where needed" was based on de-

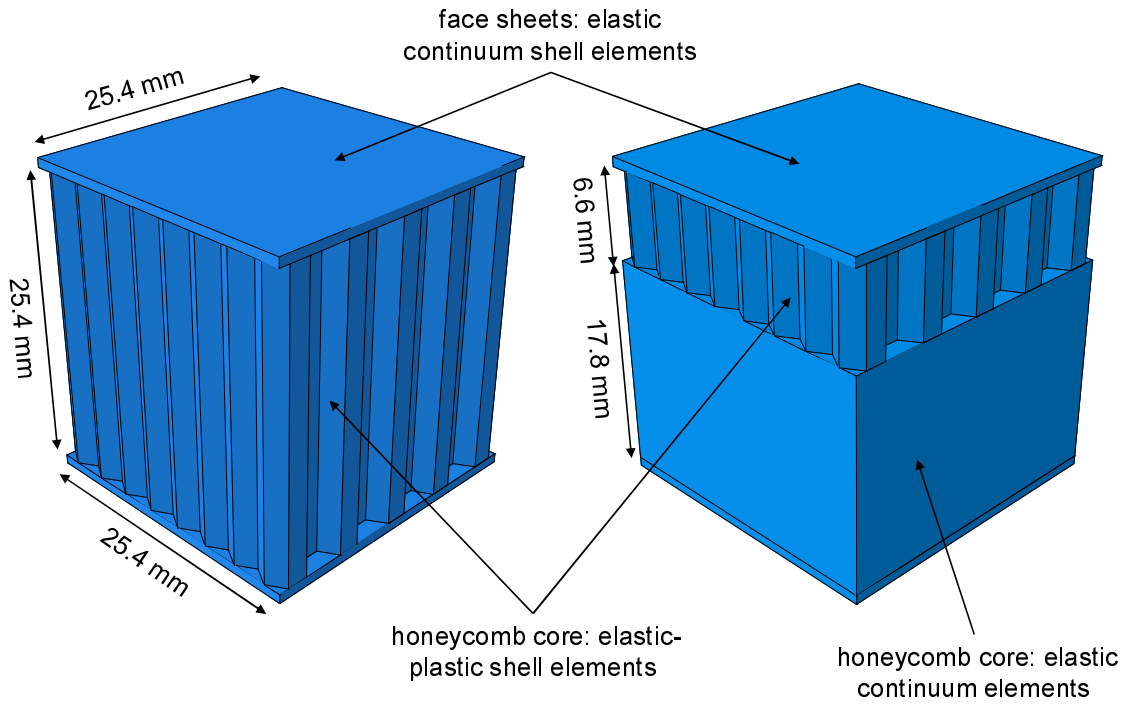

Figure 4.26: Comparison between full explicit and "hybrid" geometry core models.

structive evaluation of indented specimens and observed extent of dent deepening during CAI. Examining a typical cross-section view of an indented specimen presented in Figure 4.27, the zone of core crushing was no greater than 3 mm deep for the largest dents and was expected to no more than double during compression. With this in mind, the "hybrid" model seen on the right of Figure 4.26 contained a 6.6 mm thick (30% of total core thickness) layer of explicit geometry core and an 18.8 mm thick region of the homogenized core. To ensure consistency between the two models in Figure 4.26, their compressive response was compared in Figure 4.28, showing a good agreement.

The hybrid model compared equally well for other loading conditions (eg. out-of-plane shear) as long as the deformation was kept relatively small and core behavior remained elastic. For large, post-yield deformation, a fully geo-

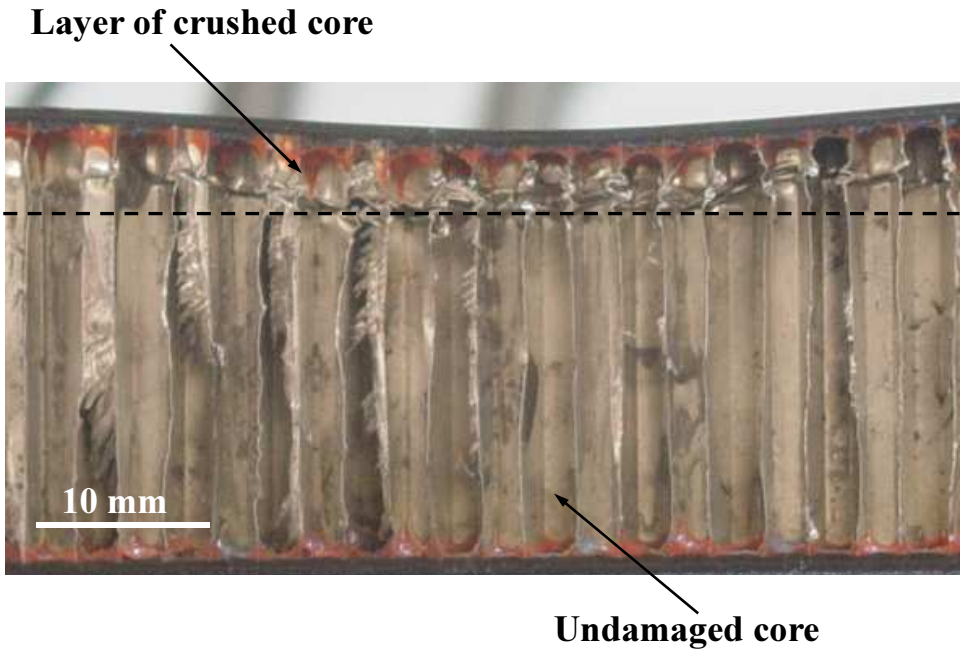

Figure 4.27: Cross-section of an indented Q1-C3 specimen.

metrically explicit model was necessary.

4.3.3 The Face Sheet Model

The face sheet deformation was modeled hybrid continuum shell elements. The continuum shell elements combine advantages of shell and continuum elements, allowing for improved computational efficiency without loss of through-thickness discretization [78]. The process of compressive fiber failure at the lamina level was modeled by incorporating the Hashin progressive failure criterion that is currently implemented in ABAQUS®. In ABAQUS® the Hashin degradation model is based on a failure criterion proposed in [79, 80]. Unlike the commonly used polynomial-based interactive failure criteria (eg. Tsai-Wu, Tsai-Hill), the Hashin criterion is failure-mode dependent, and the onset of degra-

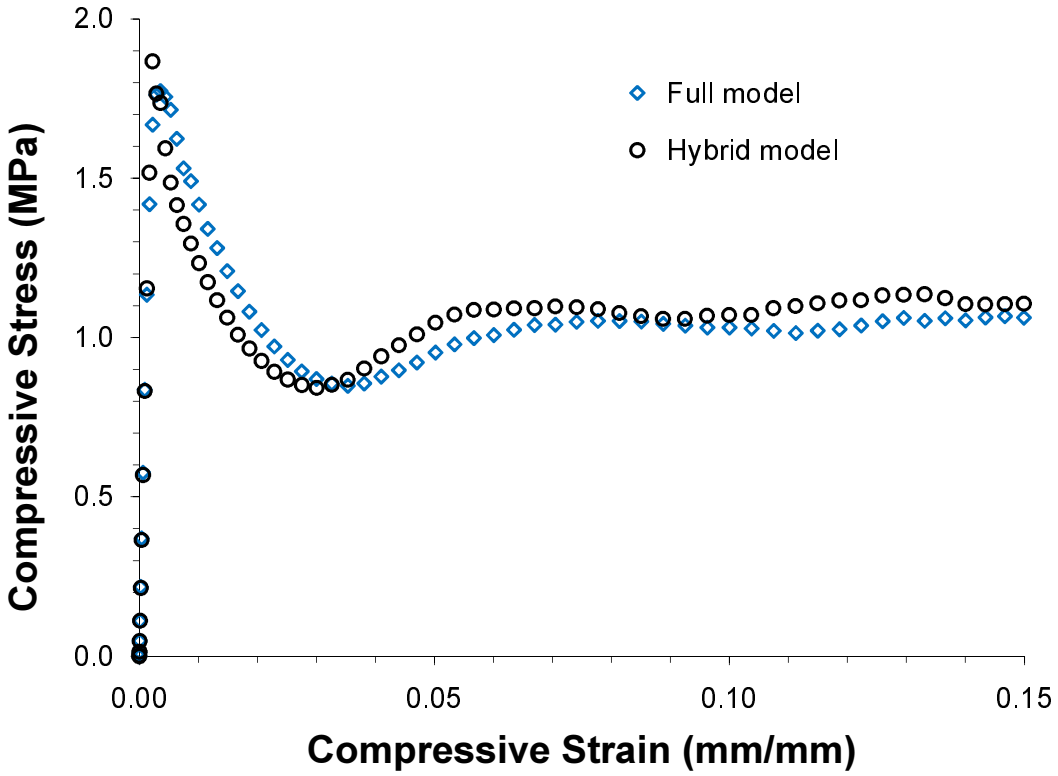

Figure 4.28: Comparison of compressive response between the full and "hybrid" geometry core models.

dation at a material point is initiated due tensile fiber failure (F_f^t), compressive fiber failure (F_f^c), tensile matrix failure (F_m^t), or compressive matrix failure (F_f^t).

In the Hashin model, the four failure modes can descried in the effective-stress space with the following analytical expressions:

$$F_f^t = \left(\frac{\hat{\sigma}_{11}}{X_t}\right)^2 + \left(\frac{\hat{\tau}_{12}}{S_l}\right)^2, \tag{4.1}$$

$$F_f^c = \left(\frac{\hat{\sigma}_{11}}{X_c}\right)^2, \tag{4.2}$$

$$F_m^t = \left(\frac{\hat{\sigma}_{22}}{Y_t}\right)^2 + \left(\frac{\hat{\tau}_{12}}{S_l}\right)^2, \tag{4.3}$$

$$F_m^c = \left(\frac{\hat{\sigma}_{22}}{2S_t}\right)^2 + \left[\left(\frac{Y_c}{2S_t}\right)^2 - 1\right]\frac{\hat{\sigma}_{22}}{Y_c} + \left(\frac{\hat{\tau}_{12}}{S_l}\right)^2, \tag{4.4}$$

where X_t, X_c, Y_t, Y_c, S_l and S_t correspond to axial tension, axial compression, transverse tension, transverse compression, longitudinal shear, and transverse shear lamina strengths values, respectively.

In the current implementation of the Hashin model in ABAQUS® the damage evolution is govern by four, individual bi-linear stress-displacement laws (analogous to a traction-separation laws used in a cohesive zone model). The initial part of each bi-linear degradation function is defined according to a positive-slope, linear equation that corresponds to elastic response of the material prior to damage. Upon initiation of failure, the damage function evolves according to a negative-slope linear equation that defines the progression of damage. The area under the bi-linear degradation function is related to the energy lost during the damage process, and is defined as G^c_{ft}, G^c_{fc}, G^c_{mt}, G^c_{mc} for failure due to fiber tension, fiber in compression, matrix in tension, and matrix in compression, respectively [78].

4.3.4 Material Property Testing in Support of Modeling

Development of a high fidelity numerical model required accurate characterization of the elastic and inelastic response of the face sheet and the honeycomb materials. For each material, obtaining a full set of material properties can be rather difficult, costly, and time consuming. However, given the relatively common use of the IM7/8552 graphite/epoxy and HexWeb CR-III honeycomb materials, a number of sources publish the required material data. With this in mind, the approach of this study was to employ the published data whenever possible and to perform selective testing to obtain most significant parameters.

In the case of the honeycomb core, most of the elastic properties were available from the manufacturer [69] or were estimated from simple elasticity theory [81]. Some inelastic properties were available in the literature; however, these were insufficient to fully define the orthotropic plasticity, homogenized core model [66, 67] and to validate the geometrically explicit core model. To complete the material characterization, including the in-plane tensile and compressive and out-of-plane shear responses of the core, two test methods were employed. As described in subsequent sections, the in-plane tensile and compressive material response was measured with a flatwise tension-compression test setup [50]. In addition, a novel axial-torsion test was developed to determine the inelastic response of the core in a state out-of-plane shear and the various combinations of out-of-plane shear and in-plane compression.

The properties required for modeling of discrete IM7/8552 carbon/epoxy plies were readily available from the manufacturer [53] and several publications [82, 83]. However, most of the published data was determined based on mechanical testing of unidirectional, monolithic, laminate coupons having relatively straight and densely packed fibers. In the case of face sheets co-cured with honeycomb, waviness of plies at the core/face sheet interface generally reduces the in-plane and flexural properties; hence, published data must be used with caution. To address this issue, the axial response of the co-cured face sheets was measured directly form the EC and CAI tests. Flexural response was measured by testing debonded face sheet coupons using a four-point bend test. With this data, the published elastic properties were appropriately corrected to produce a consistent set of parameters representative of co-cured face sheets. Finally, the failure parameters required for the Hashin ply degradation model were deemed too difficult to measure without significant effort, so these were taken from pub-

lished data.

4.3.4.1 Face Sheet Properties Testing

The correction of the published IM7/8552 carbon/epxoy orthotropic data was based on measured in-plane compliance, a_{11}, and flexural compliances, d_{11} and d_{12}, of the Q1 layup.

The in-plane compliance, a_{11}, was extracted from the EC and CAI compression data using classical laminate theory (CLT) [62]. For each Q1 specimen tested in this study, the a_{11} term was determined based on the inverse slope of the applied edge load, N_x (applied load divided by specimens width) and the average of strain data from the four alignment gages (see Fig. 4.11). In all cases, the slope was determined over a 10-90 percent range of the critical edge load.

The flexural compliances, d_{11} and d_{12}, were measured using a four-point bend test [84,85] depicted in Figure 4.29. The flexure specimens were fabricated by placing a thin layer of Teflon foil between the layer of film adhesive and the inner most face sheet ply. After debonding, the specimens were trimmed with a water-jet cutter to a length of 130 mm and width of 26 mm. The specimens were then instrumented with a CEA-06-125UT-350, 350Ω, Vishay Micro-Measurement $0/90^\circ$ strain gage at the mid-span. The outer span of the four-point bend fixture was 107 mm, the inner span was 51 mm, and the support and loading roller diameters were all 10 mm. Due to relatively small forces needed to apply sufficient bending moments, loading was performed using dead-weights in increments of 3, 5, 8 and 13 N. The applied load was converted to the edge bending moment (applied moment divided by specimen width), M_x,

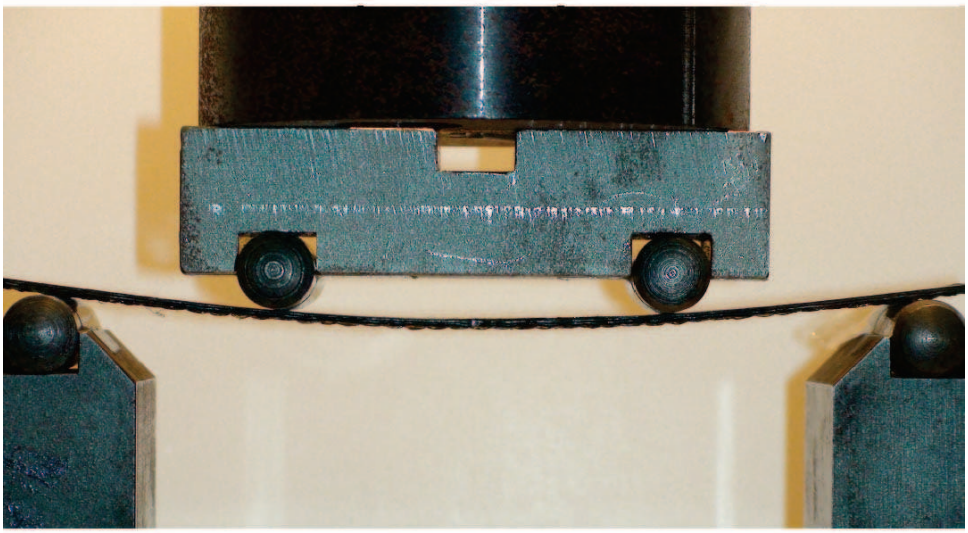

Figure 4.29: The four-point bend test setup with an 8-ply Q1 specimen. The bottom surface of the specimen shows visible face sheet waviness.

and the measured strains were converted to middle surface curvatures, k_x and k_{xy}. The surface curvatures were determined based on the assumed face sheet thickness of 1.016 mm. The slope of k_x-M_x and k_{xy}-M_x curves determined the flexural compliances, d_{11} and d_{12}, respectively.

Table 4.4: The in-plane and flexural compliance values for Q1 - $[45/0/-45/90]_s$ layup.

	a_{11} (m/N)	d_{11} (1/Nm)	d_{12} (1/Nm)
Measured	1.719E-8	0.224	-0.112
Computed with published data	1.566E-8, (- 8.9%)	0.183, (- 18.3%)	-0.112, (0%)
Computed with corrected data	1.780E-8, (+ 3.5%)	0.211, (- 5.8%)	-0.133, (+ 18.8%)

The three measured compliance values are summarized in the first row of Ta-

ble 4.4. The second row of Table 4.4 lists the compliance values computed based on CLT using the published IM7/8552 lamina properties from [53]. Comparison of respective compliance values in both rows shows that use of published lamina properties causes a significant overestimation of the in-plane and flexural stiffness of the entire laminate. To correct this issue, the published lamina properties were appropriately adjusted such that the newly computed compliance values, and in particular the critical a_{11} and d_{11} terms, were all within percent error (see third of Table 4.4). The corrected lamina properties, which were ultimately used in the numerical model, are listed in the second row of Table 4.5.

Table 4.5: Elastic material properties for IM7/8552 carbon/epoxy uni-directional lamina. Values in bold represent the corrected properties used in the model

	$\mathbf{E_1}$ **(GPa)**	$\mathbf{E_2}$ **(GPa)**	$\mathbf{E_3}$ **(GPa)**	$\mathbf{G_{12}}$ **(GPa)**	$\mathbf{G_{13}}$ **(GPa)**	$\mathbf{G_{23}}$ **(GPa)**	ν_{12}	ν_{13}	ν_{23}	**Thickness (mm)**
From Ref. [53]	164	12.0	12.0	5.17	5.17	3.98	0.32	0.32	0.44	0.127
Corrected	**143**	**12.9**	**11.7**	**4.13**	**4.13**	**3.98**	**0.32**	**0.32**	**0.44**	**0.127**

The complete summary of IM7/8552 carbon/epoxy ply strength and ply fracture toughness values required for the Hashin ply degradation model were taken from [82, 83] and are listed in Table 4.6.

Table 4.6: Ply strength and ply fracture toughness values for IM7/8552 carbon/epoxy uni-directional lamina

$\mathbf{X_t}$ **(MPa)**	$\mathbf{X_c}$ **(MPa)**	$\mathbf{Y_t}$ **(MPa)**	$\mathbf{Y_c}$ **(MPa)**	$\mathbf{S_l}$ **(MPa)**	$\mathbf{S_t}$ **(MPa)**	$\mathbf{G^c_{ft}}$ **(N/mm)**	$\mathbf{G^c_{fc}}$ **(N/mm)**	$\mathbf{G^c_{mt}}$ **(N/mm)**	$\mathbf{G^c_{mc}}$ **(N/mm)**
2323	1200	160.2	199.8	130.2	151.7	81.5	106.3	0.277	0.788

4.3.4.2 Honeycomb Flatwise Tension-Compression Test

The flatwise tension-compression test seen in Figure 4.30 was used to measure the tensile and compressive response of the honeycomb structure in the thickness direction [50, 86].

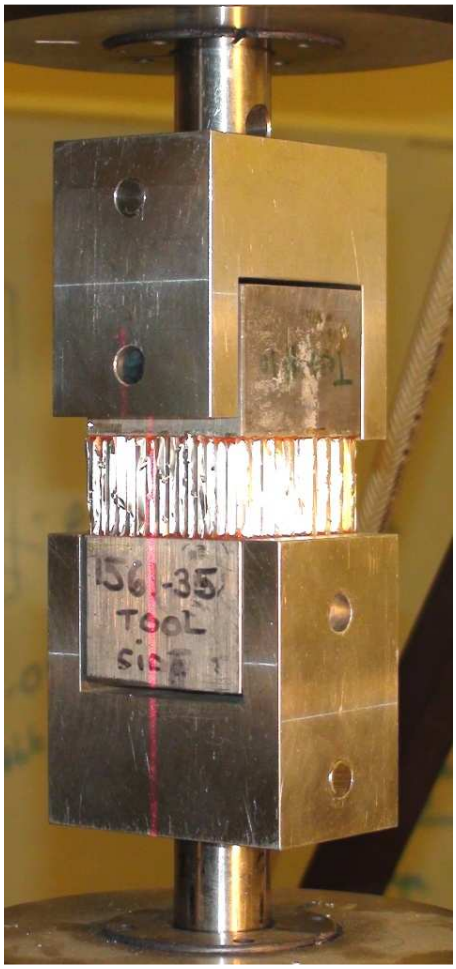

Figure 4.30: Flatwise compression test setup with a C1 honeycomb core specimen.

The test specimen consisted of 50.8×50.8 mm square honeycomb core bonded to aluminum loading blocks using the AF-555 film adhesive. The specimen deformation measured between the two loading blocks was performed

using the MTS LX-500, non-contact laser extensometer. The deformation in the elastic region was measured with the extensometer range set to 2.54 mm, while the large deformation during core crushing was done with the range set to 25.4 mm.

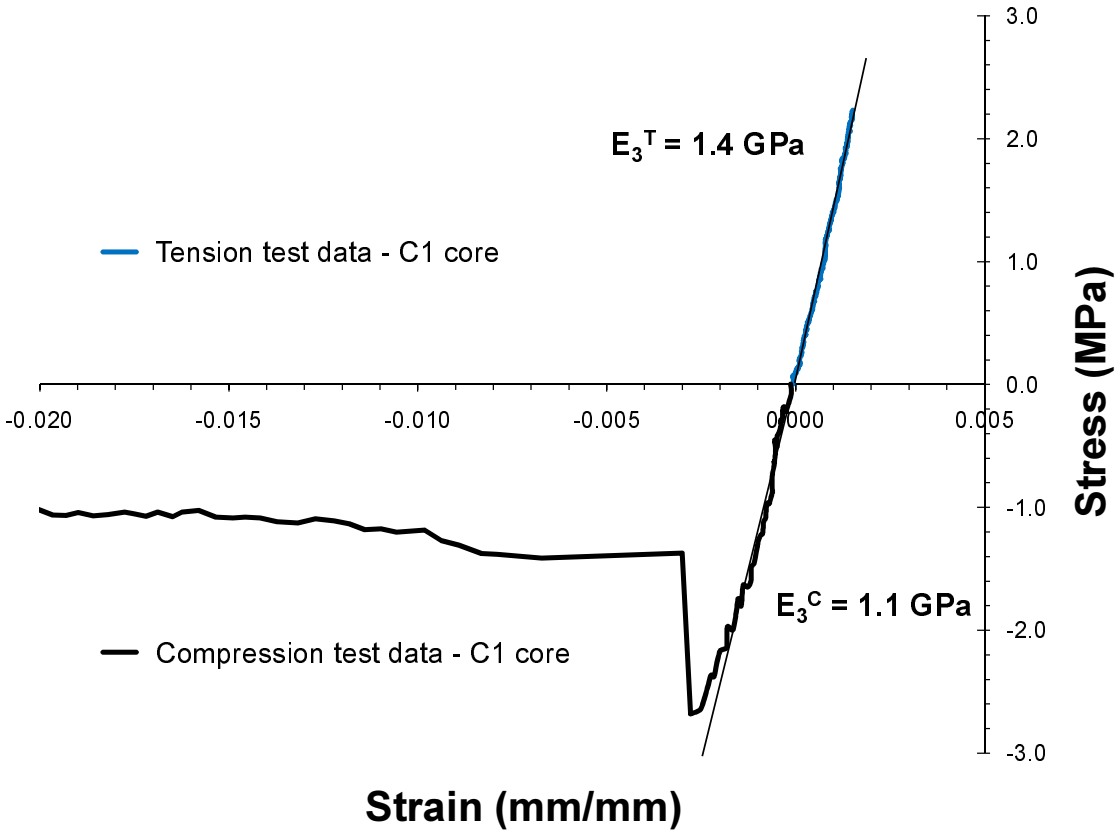

Figure 4.31: Flatwise tension-compression test data for C1 core.

Example test data from a tension-compression test of a C1 core is presented in Figure 4.31. In this test, the specimen was first loaded in tension at a rate of 0.0237 mm/s to a stress level approximately equal to 2.1 MPa. The particular tensile stress level was chosen to prevent debonding between the core and the loading blocks. Next, the loading direction was reversed and the specimen was compressed at the same rate until the peak compressive stress was reached, followed by sudden softening of the material, and core crushing at a constant stress

level. Once this stress plateau was reached, the test was halted, and the range of the extensometer switched to 25.4 mm. The compressive loading was next re-initiated and the specimen was crushed to roughly 40% of its initial thickness. An example of a full compression test for cores C1 and C3 core is presented in Figure 4.32.

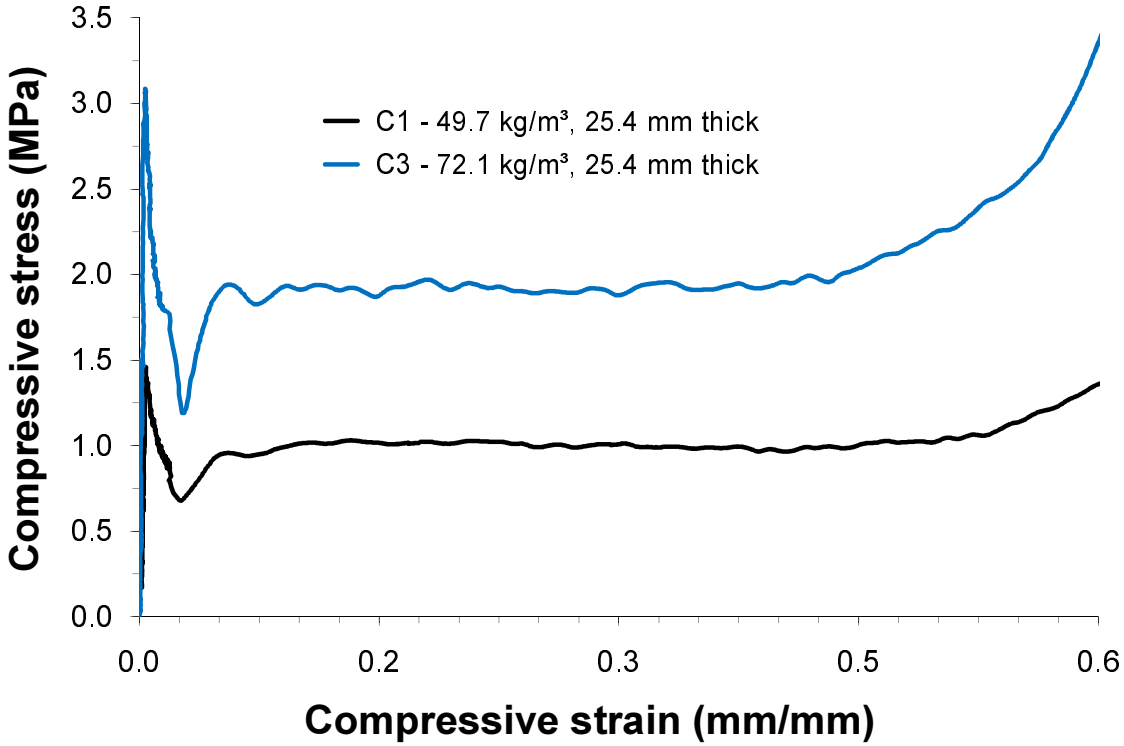

Figure 4.32: Flatwise compression test data for C1 and C3 cores.

Examining the data in Figure 4.31, the difference between the tensile and compressive moduli is approximately 0.3 GPa. The measured tensile modulus was approximately 0.1 GPa larger than the theoretically predicted modulus of 1.3 GPa, while the measured compressive modulus was approximately 0.2 GPa smaller than theoretically predicted. The difference between the experimentally measured tensile and compressive moduli can be related to initial cell wall waviness of most core specimens. During tension, the applied load partially

straightens the cell walls, and tensile modulus gradually approaches the theoretically predicted value. During compression, however, the cell walls become increasingly distorted, and the elastic compressive response becomes increasingly softer. As the load increases, the cell walls undergo finite lateral deformation, and trigger the onset of wall collapse, resulting in the sudden softening response.

4.3.4.3 Honeycomb Compression-Torsion Test

Others have proposed test setups that include combinations of compression and shear responses in honeycomb core test specimens. For example, a test setup to produce a state of pure out-of-plane shear and a combination of shear and thickness-wise compression was proposed in [87]. In that study, the core samples were tested in a specially modified bi-axial load frame, where a coupled application of lateral and vertical loads allowed for essentially any combination of shear and compression. Additionally, a similar study [88] employed a modified Arcan apparatus, where, by changing the orientation of the test fixture with respect to the loading direction, the test provided a range of compression/shear load cases.

In this study, duplicating one of the two existing test methods was limited either by the complexity of the testing equipment or by the inability to attain the entire spectrum of compression/shear loading cases. Therefore, a new test was developed and incorporated into the existing axial-torsion load frame to provide an approximate state of pure out-of-plane shear and any combination of out-of-plane shear and thickness-wise compression. The test proposed in this study was based on the fact that twisting of a thin-wall cylinder about its axis

produces an approximate state of uniform, pure shear in the wall. In such a case, the assumption holds true given the ratio of the inner and outer radii of the cylinder remains close to unity.

Exploiting this idea, the newly proposed test consisted of a honeycomb specimen (see Fig. 4.33) having geometry of a hollow cylinder with an inner and outer radii of 50.8 and 63.5 mm, respectively. The specimen geometry was chosen such that when twisted, the ratio of the minimum and maximum values of shear stress across the wall thickness remained near unity (appx. 0.8), while keeping the specimen wide enough to measure the out-of-plane shear across several cell units. To ensure that shear was measured along the ribbon direction, the test specimen consisted of four, quarter-pieces seen in Figure 4.33, each aligned with that direction. The set of four quarter-pieces was bonded to two circular loading platens using AF-555 adhesive, forming a cylindrical specimen. The specimen was then clamped to the axial-torsional load frame using hydraulic grips (Fig. 4.34). The compression was measured using a non-contact, MTS LX-500, laser extensometer, while rotation was measured using a rotary variable differential transformer (RVDT) built into the MTS axial-torsion load frame system.

In the test, the approximate state of pure shear was achieved by twisting the specimen in rotation control, while simultaneously enforcing zero axial force between the loading platens. The enforcement of zero axial force minimized the tensile stresses that can develop in the honeycomb walls at large angles of rotation. A pure compression test was done in the same way as the previously mentioned flatwise compression test. Rotation and displacement control were used in each test to ensure test stability in the post yield, softening loading regime.

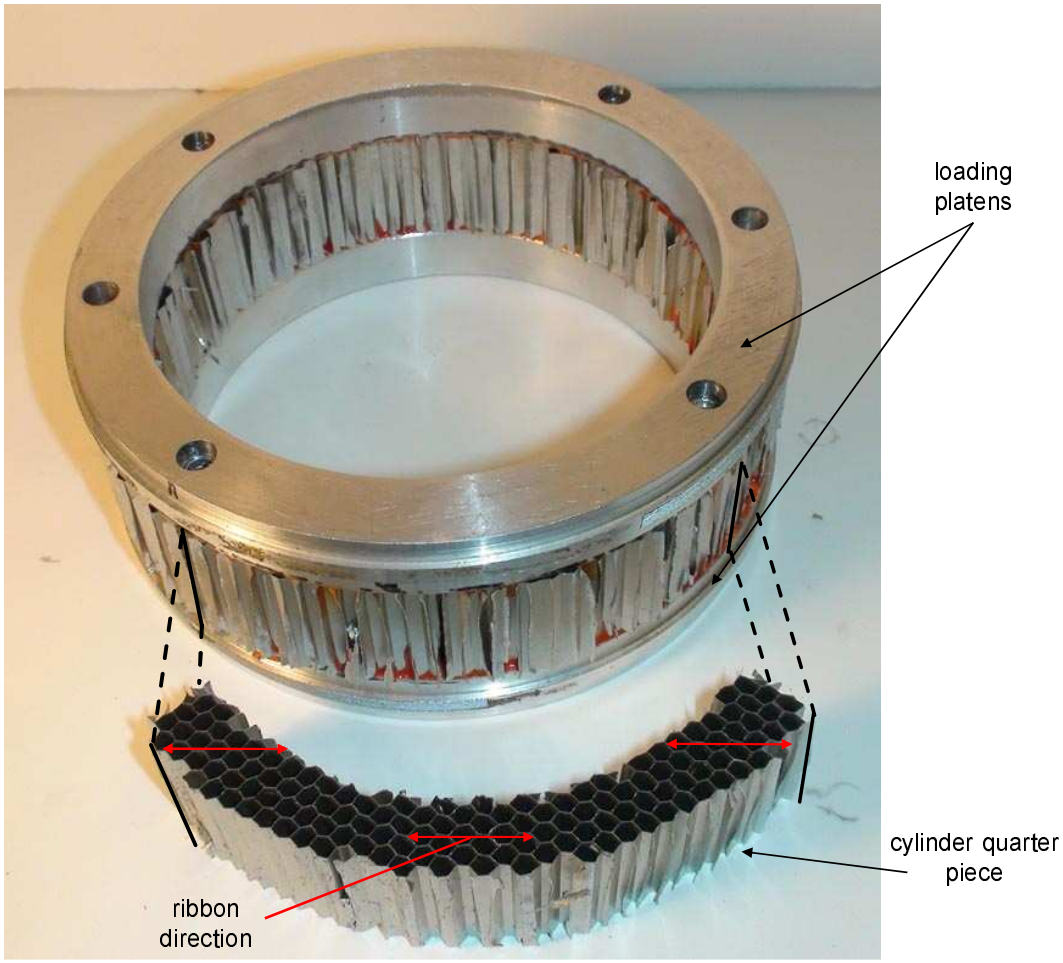

Figure 4.33: The torsion/compression test specimen.

The data from each tests provided a measure of yield stress in pure shear, τ_{yld}, and pure compression, σ_{yld}, and the corresponding angle and displacement at yield, ϕ_{yld} and δ_{yld}, respectively.

A combined shear/compression test procedure depended on a desired ratio of shear and compression stresses. Defining parameters S $\equiv$ τ/τ_{yld}, and C $\equiv$ σ/σ_{yld}, where τ and σ are the applied shear and axial stresses, respectively, the loading rates depended on the exact ratio of S to C. For instance, to achieve a loading scenario where S/C=1, compression and rotation had to be applied

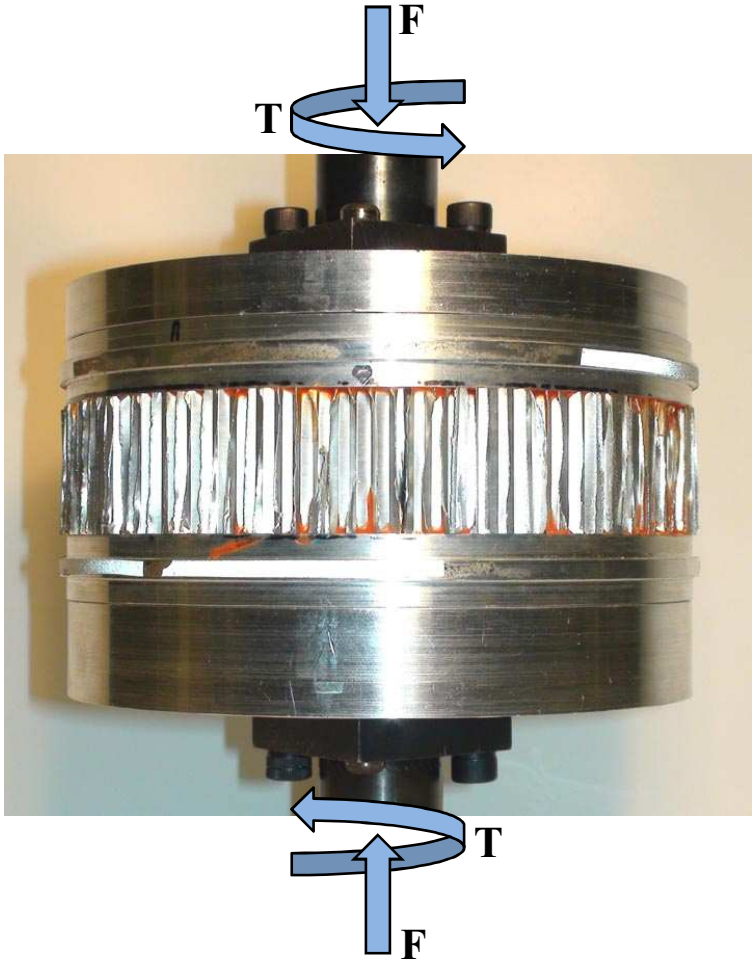

Figure 4.34: The torsion/compression test setup.

such that ϕ_{yld} and δ_{yld} were attained at the same time. Similarly, for the ratio S/C=0.5, compression and rotation had to be applied such that ϕ_{yld} and $\delta_{yld}/2$ were attained at the same time.

Using this approach, a number of tests were performed over a range of S/C ratios to determine the τ_{yld}/σ_{yld} yield envelope, which is presented in Figure 4.35. In Figure 4.35, for each loading configuration, the shear yield stress is plotted as a function of compressive yield stress. Hence, the left most data point corresponds to a pure shear test, and the right most data point corresponds to

a pure compression test. The intermediate points correspond to different values of S/C ratios. Surprisingly, the experimentally determined yield envelope appears to be essentially elliptical in the τ_{yld}/σ_{yld} stress space.

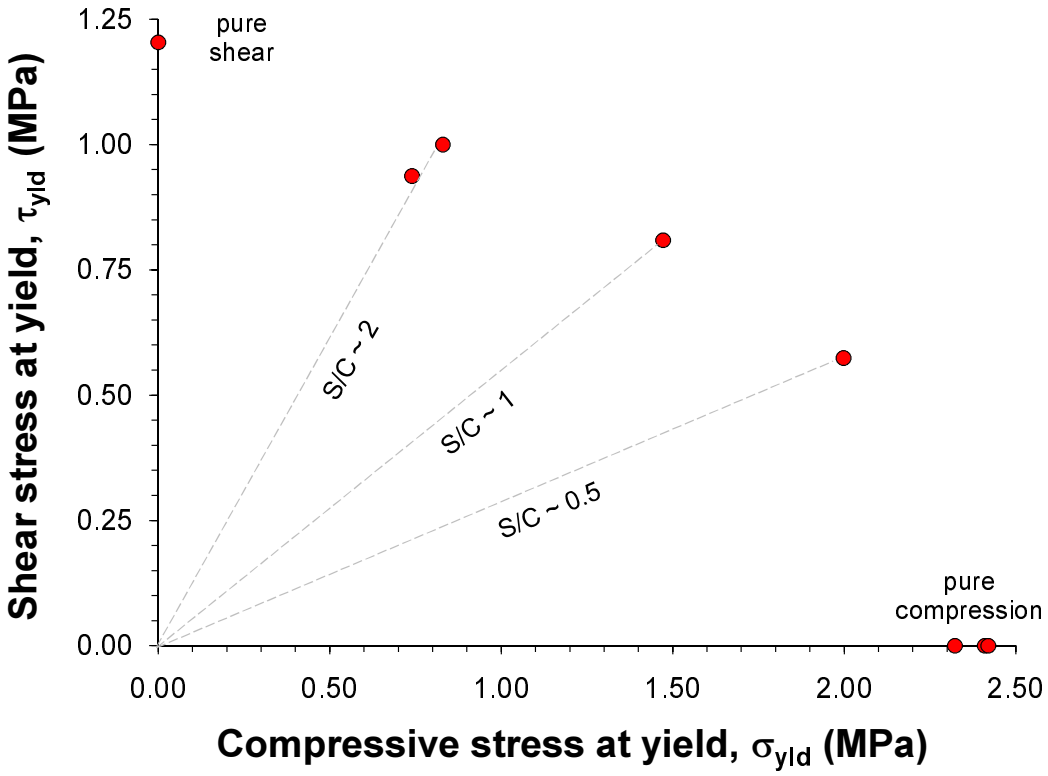

Figure 4.35: The shear/compression yield envelope for C1 core (49.7 kg/m^3, 25.4 mm thick).

4.3.5 Assembly of the Sandwich Panel Models

The development of sandwich panel models was focused on simulating core damage resulting from QSI and core and face sheet failure during CAI. Two distinct types of sandwich panel models were developed. In the first model, the honeycomb core was fully homogenized and represented as an anisotropic plasticity material described in Section 4.3.2.1. In the second model type, the "hy-

brid" core idea presented in Section 4.3.2.2 was employed, where honeycomb was represented as a combination of homogenized continuum and explicit cell geometry. In each model, face sheets were identically represented using continuum shell elements, and both models shared the same set of boundary conditions and loads.

The overall planar size of all models was optimized according to a preliminary set of simulations of a full 15.2×17.7 cm specimen. Based on expected extent of planar damage during QSI/CAI, the model size was lowered to 7.62×7.62 cm, allowing for reduction of computation time without affecting the simulation results. In all models, the 7.62×7.62 cm face sheets were discretized using 1.27×1.27 mm square, 1.02 mm thick, eight-noded, general purpose, SC8R continuum shell elements. Each element was assigned material properties from Tables 4.5 and 4.6 on the per-lamina basis using ABAQUS/CAE "*Composite Layup*" module. In this module, the elastic lamina properties were specified and arranged according to a pre-defined face sheet stacking sequence to determine the laminate global stiffness response. The final mesh size was determined based on a convergence study and simulation of the four-point bend test described in Section 4.3.4.1. The progressive face sheet failure model based on the Hashin failure criterion was implemented using the "*Damage for Fiber-Reinforced Composites: Hashin Damage*" material property module.

For the sandwich panel model with the homogenized, inelastic core material, the entire 7.62×7.62×2.54 cm core region was discretized using 1.27×1.27×25.4 mm, eight-noded, C3D8R linear brick elements. The interaction between the core "slave surface" and the face sheet "master surface" elements was achieved using ABAQUS/CAE surface-to-surface "Tie" feature. The "Tie" feature assigns

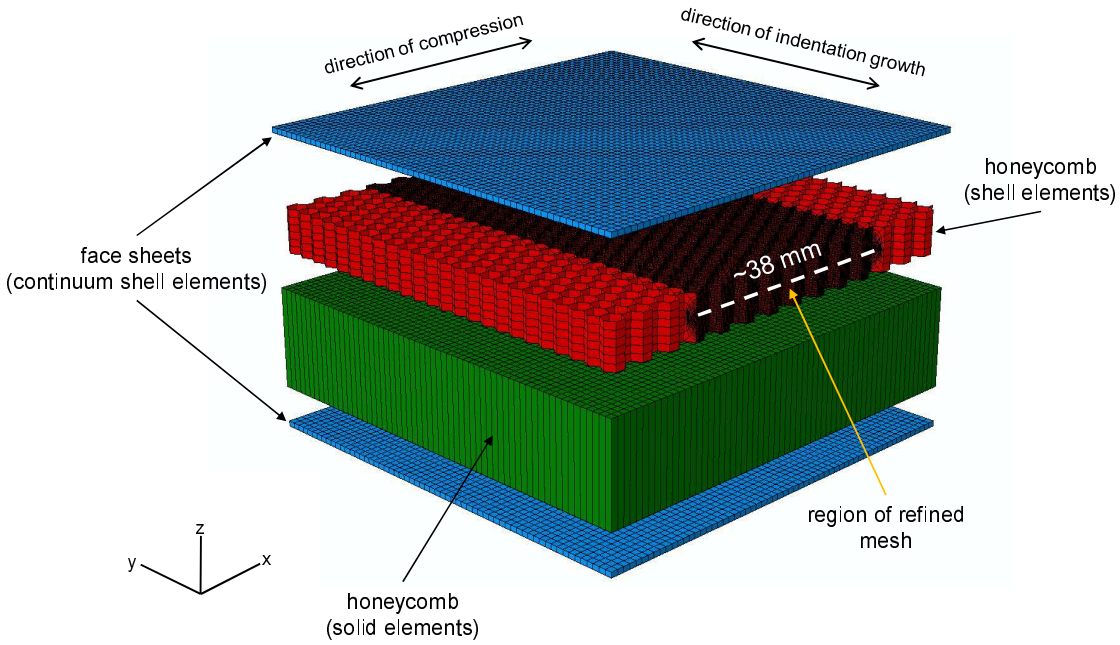

Figure 4.36: An exploded view of a sandwich panel model with a combination of homogenized and explicit core geometry. The refined mesh of the explicit geometry core was used to accommodate extensive damage during indentation with the 76.2 mm dia. indentor and the resulting unstable dent growth during compression.

to each nodal degree of freedom on the slave surface the corresponding values taken from the nearest neighboring node of the master surface.

The sandwich panel models with the ”hybrid” core employed distinct regions of highly refined mesh, where the size of the refined region depended on one of two indentor sizes. Details of each region are presented in the ”exploded” view of the sandwich panel model presented in Figures 4.36 and 4.37. In each case, the extent of the refined mesh was determined based on the extent of core crushing in a QSI/CAI simulation that had a fully refined mesh. For a QSI simulation with the 76.2 mm dia. indentor (Fig. 4.36), the refined mesh region had a length of approximately 38 mm, and spanned the entire width of the

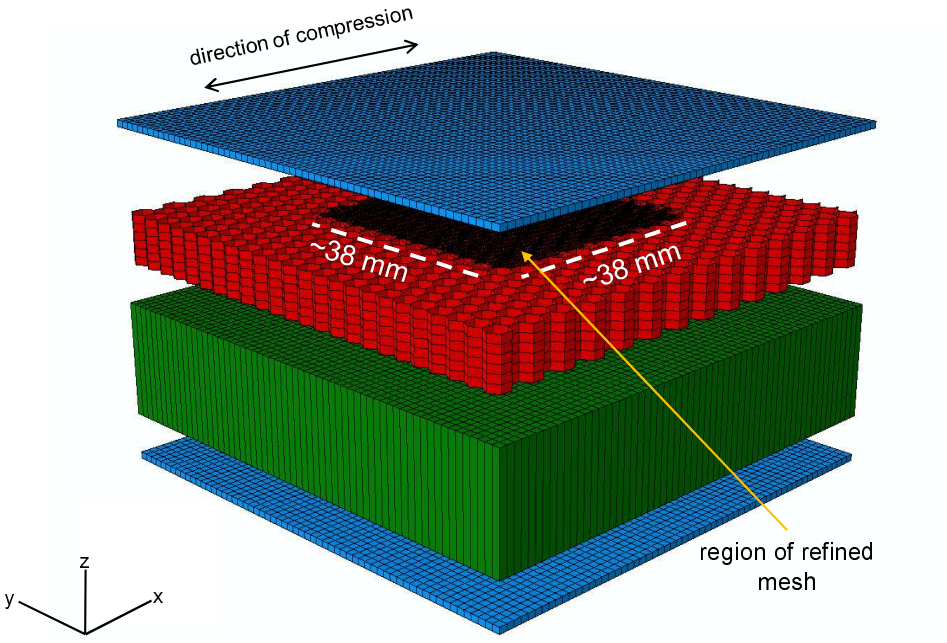

Figure 4.37: An exploded view of a sandwich panel model with a combination of homogenized and explicit geometry core. The refined mesh of the explicit geometry core was used to accommodate smaller extent of core crushing during QSI using the 25.4 dia. indentor.

panel in the direction perpendicular to the loading direction. The large region was needed to accommodate extensive core crushing from a large diameter indentor and was placed in a path of expected unstable dent growth. For a QSI simulation with 25.4 mm dia. indentor, where extensive dent growth was not expected, the mesh refinement was contained within a 38×38 mm square inner region. The homogenized region of the honeycomb core away from impact damage was modeled using 1.27×1.27×17.78 mm, eight-noded, C3D8R linear brick elements with orthotropic properties from Table D.1. The interactions between the explicit core and the top face sheet and between the explicit core and the homogenized core were established using ABAQUS/CAE "Shell-to-Solid" coupling module. The "Shell-to-Solid" coupling feature couples the displacements and rotations of each shell node to the average computed displacements

and rotations of the solid surface in the vicinity of the shell node [78]. The interaction between the homogenized core and the bottom face sheet was achieved using the surface-to-surface "Tie" feature.

In all simulations, the 25.4 and 76.2 mm dia. spherical indentors were modeled as rigid hemi-spherical shells, discretized using four-noded R3D4 rigid elements. A general-contact algorithm with "hard" normal-direction contact property was established between the top face sheet and the indentor. No tangential friction was assumed.

In each modeling case, both QSI and CAI were simulated using the same FE model and two distinct ABAQUS/Explicit loading steps. The boundary conditions and loading for each step are presented in Figures 4.38 and 4.39. During QSI, the bottom face sheet was constrained from displacement in the z-direction to simulate the surface of the bottom compression platen in the QSI test. Additional corner nodes of the bottom face sheet were constrained in the x and y direction to prevent any rigid body rotation or translation in the x-y plane. The quasi-static indentation was performed in load control by applying a z-direction point load to a reference node located in the center of the hemispherical indentor. The load incrementation used a "smooth" amplitude, which allowed for a desired gradual load ramp during a quasi-static simulation.

In the second step of the simulations, all of the initial boundary conditions applied to the panel were retained, and additional constraints were added to represent boundary conditions at the compression platens. The z-direction constraint on the bottom face sheet was not removed in this step, as it did not change the behavior of the panel during compression and its removal would require an additional model equilibration step, significantly lengthening the en-

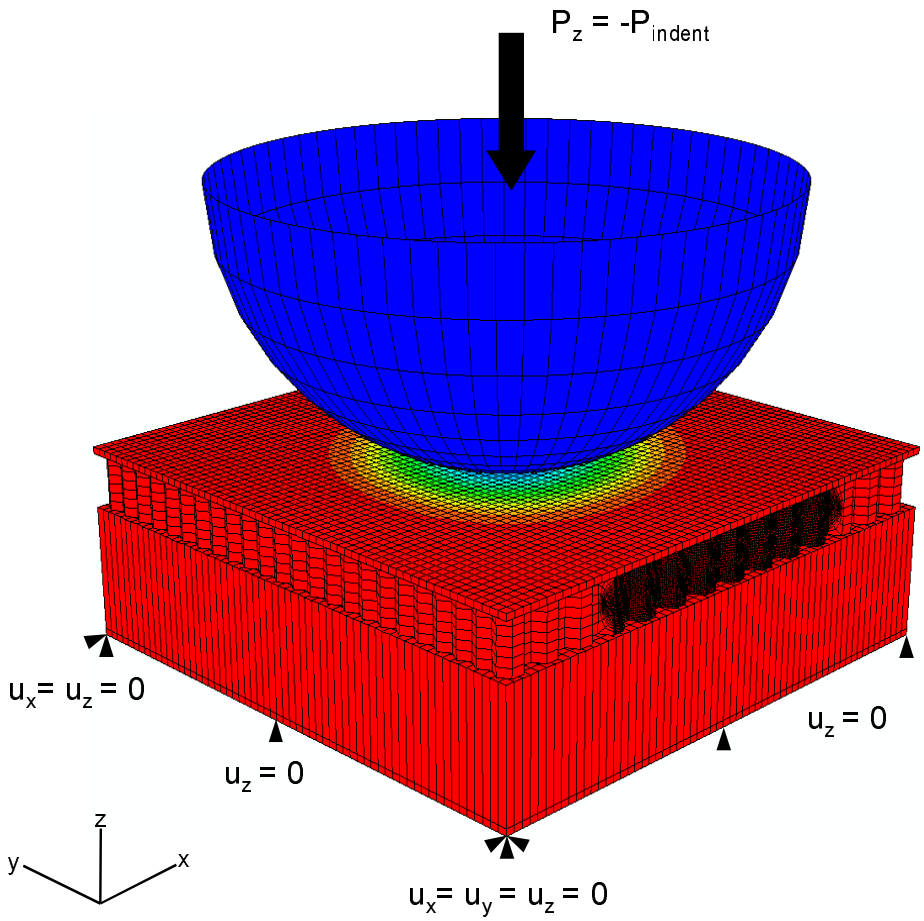

Figure 4.38: Boundary conditions and loading during simulation of quasi-static indentation.

tire simulation. As seen in Figure 4.39, the left hand side of the panel was constrained from displacing in the x-direction, and the compression was applied in displacement control using a linear amplitude ramp on the opposite side.

4.3.6 Simulation Results of Quasi-Static Indentation

The numerical results of QSI simulation using the homogenized core model are presented in Figures 4.40 and 4.41. Figure 4.40 compares the QSI force-

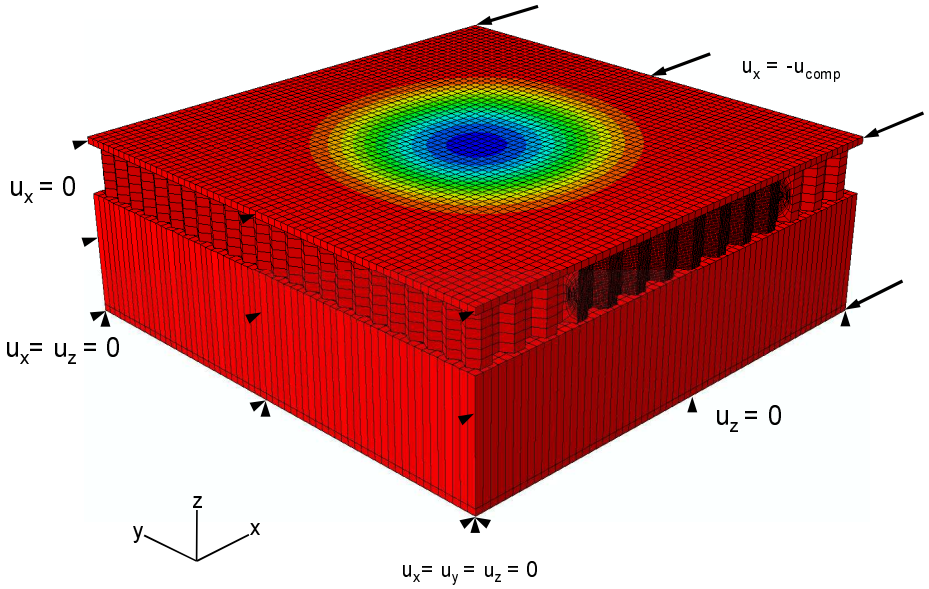

Figure 4.39: Boundary conditions and loading during simulation of CAI test.

displacement response of the experiment and the simulation. As seen in this figure, the numerical simulation significantly overestimates the stiffness of the panel during indentation, but appears to converge to the correct permanent dent depth upon unloading. However, as discussed in Section 4.2.3, the permanent deformation measured using the indentor position does not physically correspond to the actual dent depth. A more direct way of assessing accuracy of the simulation is by comparing the simulated dent profiles to the ones measured with ultrasonics. As seen in Figure 4.41, the homogenized core model significantly overestimates the dent size as evident by the maximum depth depth. The simulated permanent dent depth was approximately 14% larger than measured for the 76.2 mm dia. indentor and approximately 25% larger than measured for the 25.4 mm dia. indentor.

One explanation for this difference could be the inability of the homogenized core model to distinguish between tensile and compressive loading during the

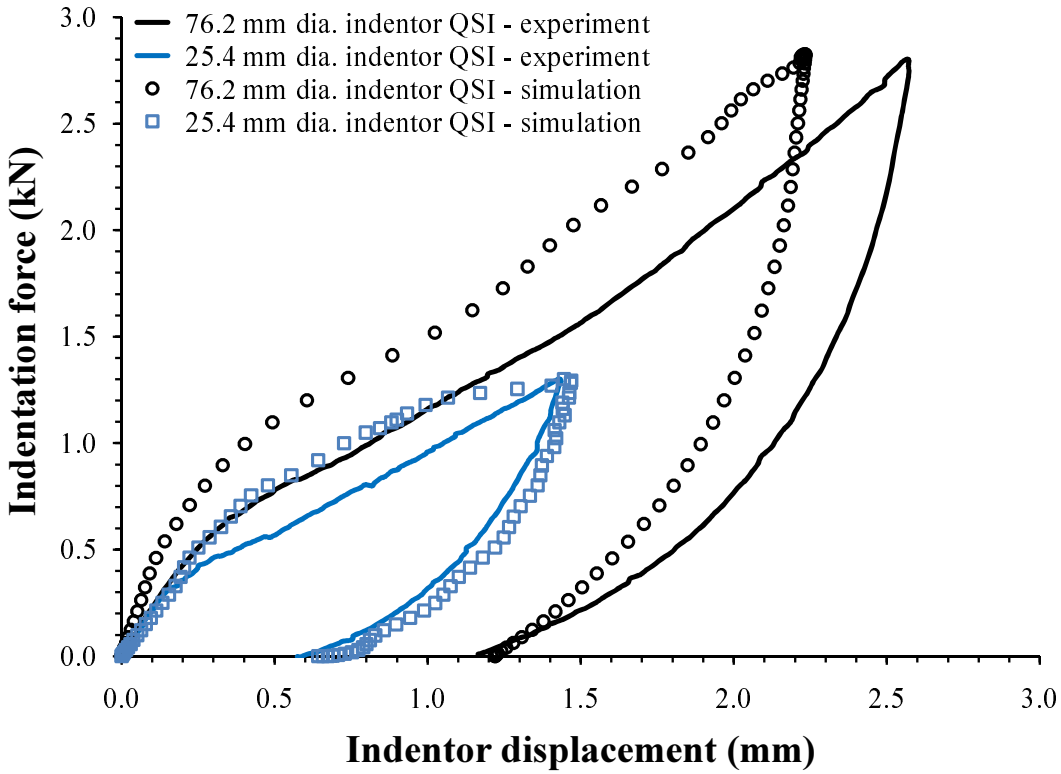

Figure 4.40: Force-displacement response during quasi-static indentation - experiment versus simulation using the homogenized core model (Q1-C1 panel geometry).

simulation. More specifically, analogous to a typical isotropic plasticity model, the present homogenized core model uses a single hardening curve to represent both the compressive and tensile response of the material for each of the six components of stress. Consequently, as long as the indentor is imparting a compressive load onto the core, a correct, compressive, hardening curve is used. However, when the loading is reversed during the indentor removal, and the core is placed in tension by the rebounding face sheet, the core model response is artificially stiff. The increased tensile stiffness causes reduced face sheet rebound and, hence, a significant discrepancy between the simulation and the experiment.

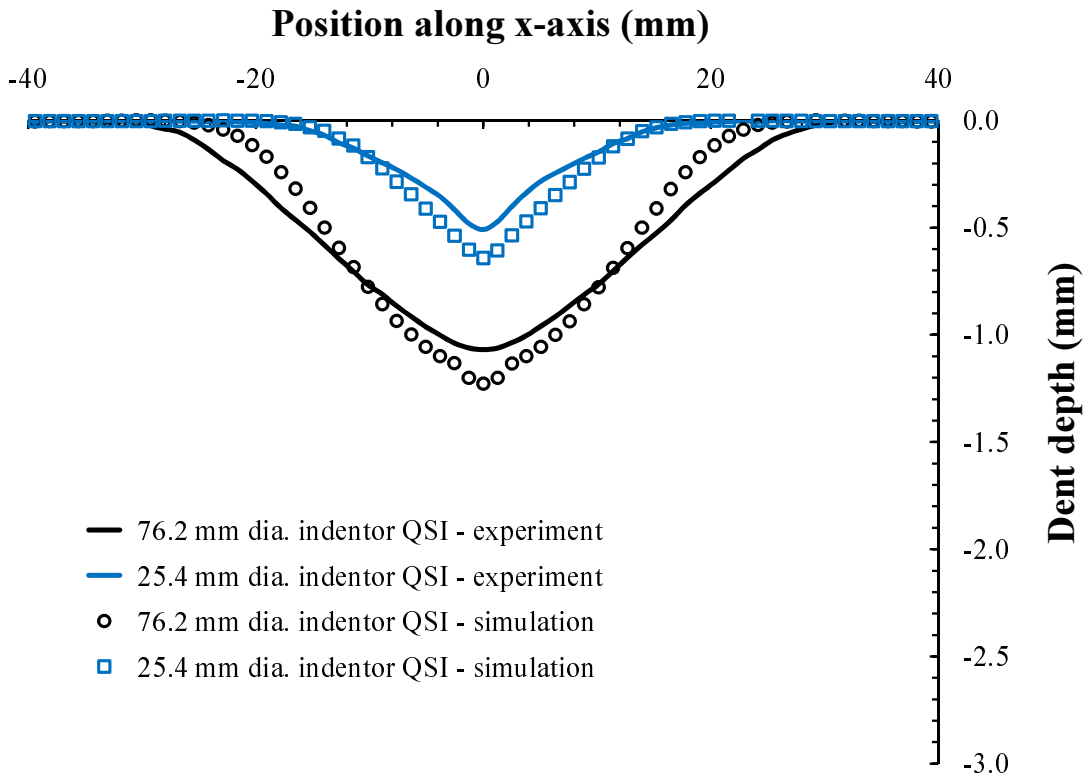

Figure 4.41: Dent profiles resulting from quasi-static indentation - experiment versus simulation using the homogenized core model (Q1-C1 panel geometry).

The explicit geometry core model simulation data is compared to the experiment in Figures 4.42 and 4.42. Examining Figure 4.42, the simulated dent depths are slightly shallower than the experimental measurements, and there appears to be some variation in the profile shapes. In both indentor cases, the simulated permanent dent depths are approximately 7-8% smaller than the measured dent depths. The relatively small discrepancies between dent profiles are likely due to internal face sheet damage in the form of interlaminar delaminations and fiber/matrix failure, which is not included in this model. Generally, internal damage will cause an increase in the face sheet compliance, and hence reduce rebound of the face sheet during indentor unloading. In addition, the delamination located near the free surface of the specimen may undergo some open-

ing deformation upon unloading of the indentor and result in slightly distorted dent profiles.

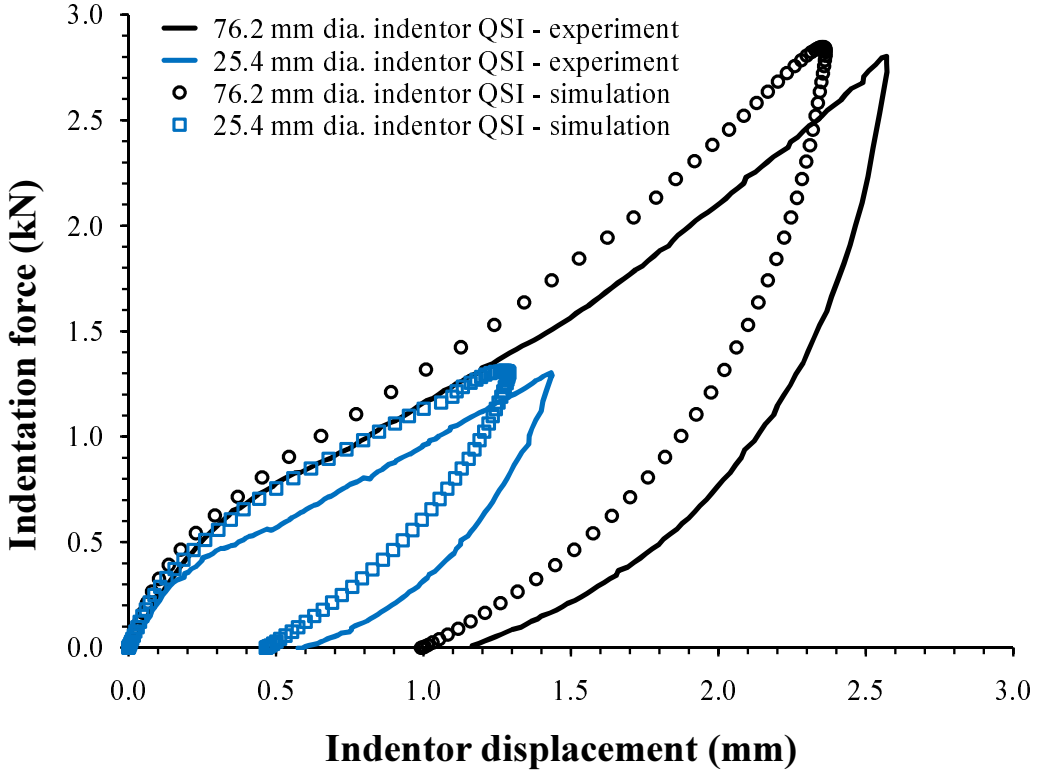

Figure 4.42: Force-displacement response during quasi-static indentation - experiment versus simulation using the explicit core model (Q1-C1 panel geometry).

Despite these small differences, the explicit core model provides a significant improvement over the homogenized core model, and this approach was explored further by examining the effects of maximum QSI indentation force on the residual dent depth. Here, for both 25.4 and 76.2 mm dia. indentor, the QSI simulation was repeated over the range of QSI loads considered in this study. The resulting dent depths were plotted versus the applied QSI force and are presented in Figure 4.44. The data in Figure 4.44 include simulations where core crushing is the only failure mechanism (solid symbols), and a simulation where both core crushing and Hashin face sheet failure model were included (open

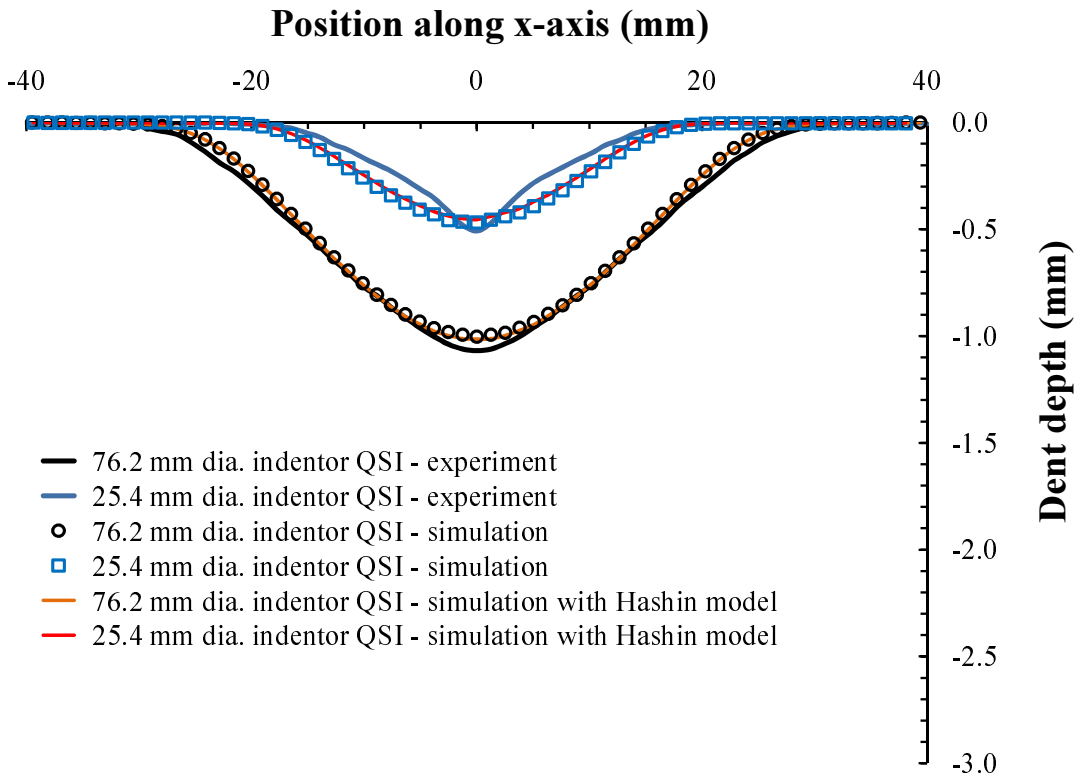

Figure 4.43: Dent profiles resulting from quasi-static indentation - experiment versus simulation using the explicit core model (Q1-C1 panel geometry).

symbols), and experimental data (individual symbols). Additionally, each set of simulated data was fit using a second degree polynomial to express the maximum QSI load as a function of maximum dent depth.

Despite the small number of data points, the numerical results remained in close agreement with the experiment. For both indentor diameters, the inclusion of the face sheet damage model provided improved correlation to the experimental data, especially for high QSI loads. However, the numerical results obtained from the model with Hashin face sheet degradation must be examined with caution. Examining the QSI simulation for the 25.4 mm dia. indentor at the highest QSI load, 1.88 kN, the difference between the simulated dent

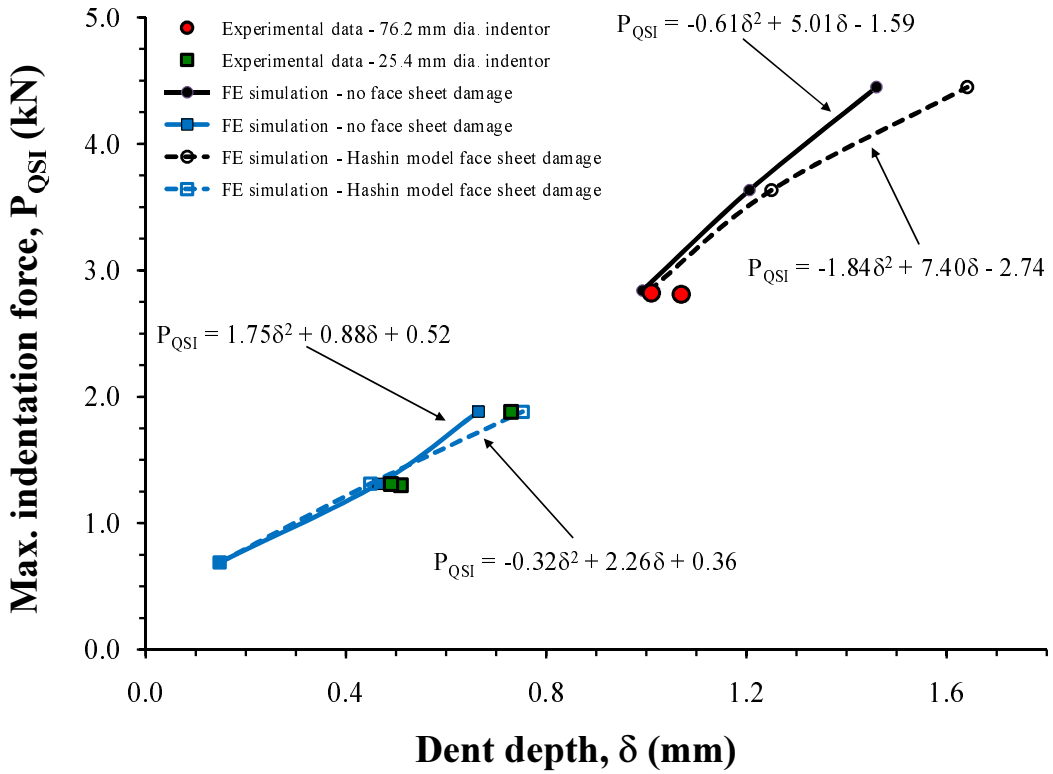

Figure 4.44: Maximum indentation force as a function of dent depth - numerical results and experimental data (Q1-C1 panel geometry).

depths with and without face sheet damage is approximately 12.4%. For the 76.2 mm dia. indentor and the highest QSI load, 4.45 kN, the difference between simulated dent depth with and without face sheet damage is approximately 11.7%. The significant difference at high QSI loads results from a number of elements underneath the indentor exceeding the failure criterion during indentation, causing degradation of the element stiffness and resulting in a decreased face sheet rebound. However, destructive evaluation of the indented specimens revealed no evidence of intra-ply damage in the form of fiber breakage or matrix cracking. It is very likely, therefore, that the excess energy that caused the simulated intra-ply failure would likely go towards inter-ply damage (a process that was indeed observed experimentally) if an appropriate delamination

initiation/growth model was included. The presence of interlaminar delaminations would similarly decrease the face sheet stiffness, and result in deeper, more accurate dents.

4.3.7 Simulation Results of Compression After Impact

Following the simulation of QSI, the second step of the analyses was the simulation of CAI. In the case of the homogenized core model, the simulation of CAI was performed without the Hashin face sheet degradation model and with QSI damage from only the 76.2 mm dia. indentor. This particular model and QSI damage was selected to investigate the unstable dent growth failure mode that is largely controlled by the core behavior. An example of stress-strain data from the CAI simulation is presented in Figure 4.45. As expected, based on the QSI simulation results, use of the homogenized core model resulted in unrealistically high failure loads, which were roughly 54% higher than observed in the experiment.

Based on the results, it is evident that in the current form the homogenized core model provides marginally good results when used to simulate the QSI, and rather poor results when simulating CAI. Given the current results, it appears that improving performance of the homogenized model would require unrealistically "tuning" the input properties to obtain better correlation with experimental data. This correction, however, may only apply over a certain range of data and goes against the idea of developing numerical tools that are robust and generalizable over a wide range of panel geometries.

Given the above conclusion, the remainder of this section focuses on simula-

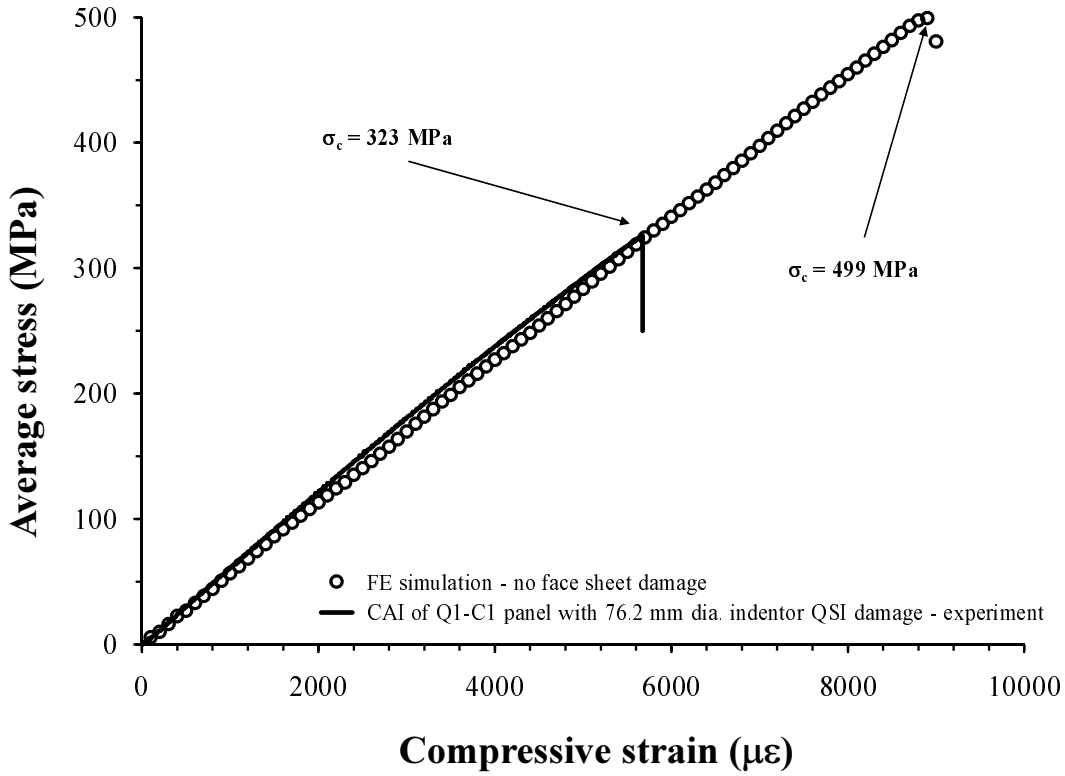

Figure 4.45: CAI test of a Q1-C1 specimen containing 76.2 mm dia. indentor QSI damage - experiment versus simulation using the homogenized core model.

tion of CAI using the explicit geometry core model. Face sheets were modeled with and without Hashin degradation to examine unstable dent growth during CAI following QSI with a 76.2 mm dia. indentor. Because unstable dent growth was not expected during CAI following QSI with a 25.4 mm dia. indentor, face sheets were modeled only using Hashin degradation in that simulation.

Two examples of typical stress-strain data from the CAI simulation of a panels indented using a 25.4 and 76.2 mm dia. indentors are presented in Figures 4.46 and 4.47, respectively. In both figures, the small differences between slopes of the experimental and simulated curves are related to elastic lamina properties used in the simulation (see Sec. 4.3.4.1) and moderate non-linearity of the

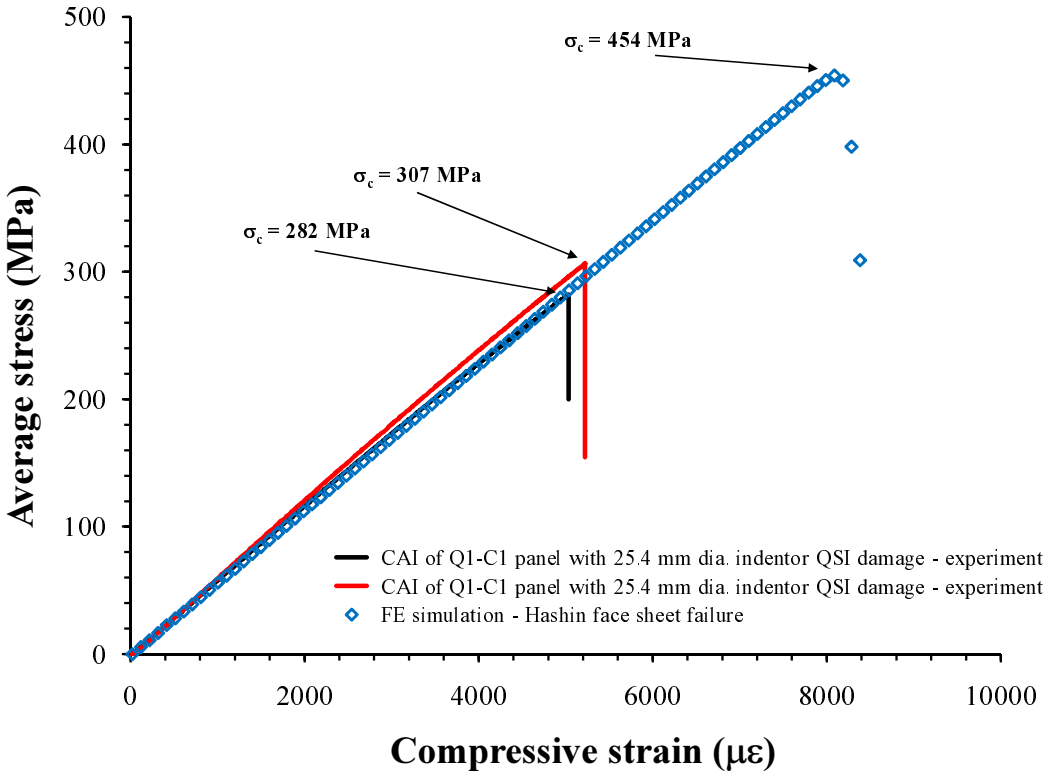

Figure 4.46: CAI test of a Q1-C1 specimen containing 25.4 mm dia. indentor QSI damage - two experimental curves versus simulation using the explicit core model.

experimental curves. A summary of the computed strength data for all CAI simulation is presented in Figure 4.48. Examining Figure 4.48, for panels with QSI damage resulting from 76.2 mm dia. indentor, the CAI simulation over-predicts the residual strength by approximately 17% (with face sheet damage) to 22% (without face sheet damage). For QSI damage resulting from 25.4 mm dia. indentor, the CAI simulation over-predicts the residual strength by approximately 45-54%. In both cases, as expected, the residual strength decreases with the increase in QSI damage, where damage is defined as the residual dent depth.

For specimens with smaller QSI damage (i.e. due to a 25.4 mm dia. indentation) the simulation yielded neither qualitatively nor quantitatively accurate

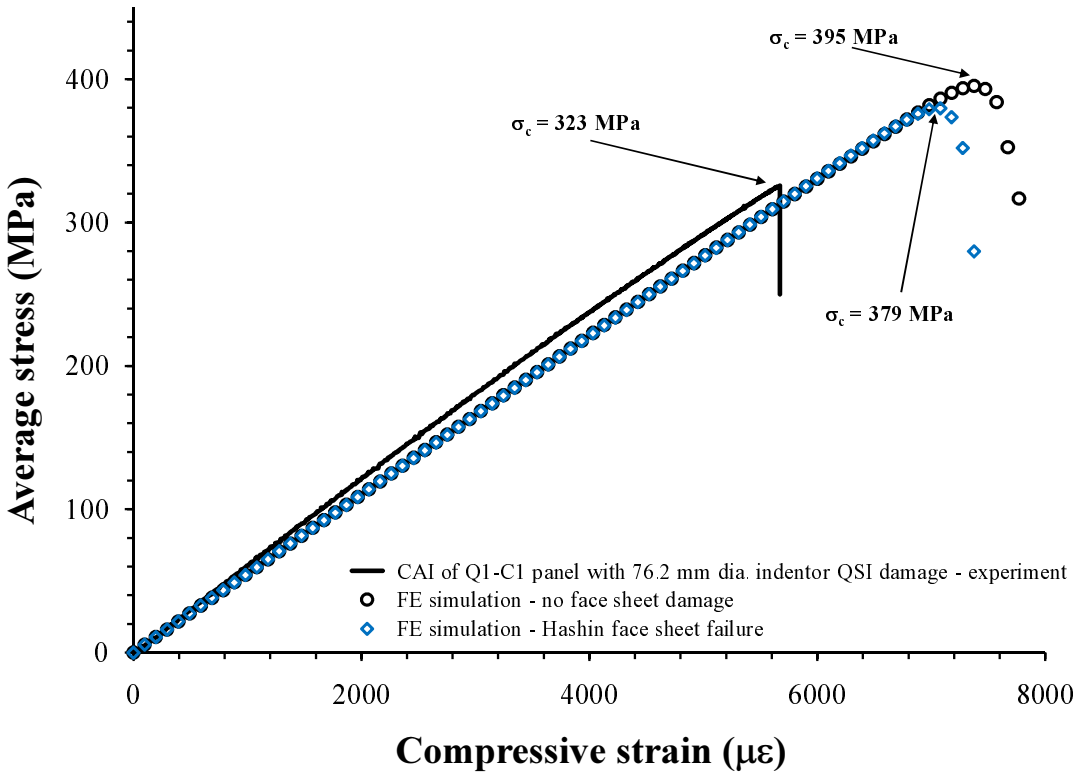

Figure 4.47: CAI test of a Q1-C1 specimen containing 76.2 mm dia. indentor QSI damage - experiment versus simulation using the explicit core model.

results. One reason for the relatively large discrepancy between the simulation and the experimental data can be explained by examining the use of Hashin progressive failure model to simulate failure during edgewise compression on an undamaged sandwich specimen (i.e. without indentation damage). The result of this simulation, shown as a horizontal dashed line in Figure 4.48 suggests that the model overestimates the experimentally measured undamaged strength (solid horizontal line) by approximately 35%. The large difference is likely because the strength and fracture energy parameters that control initiation and evolution of failure in the Hashin model (see Table 4.6) were measured on monolithic, waviness-free, unidirectional laminate coupons, which are not exactly representative of co-cured sandwich face sheets. That is, given the sen-

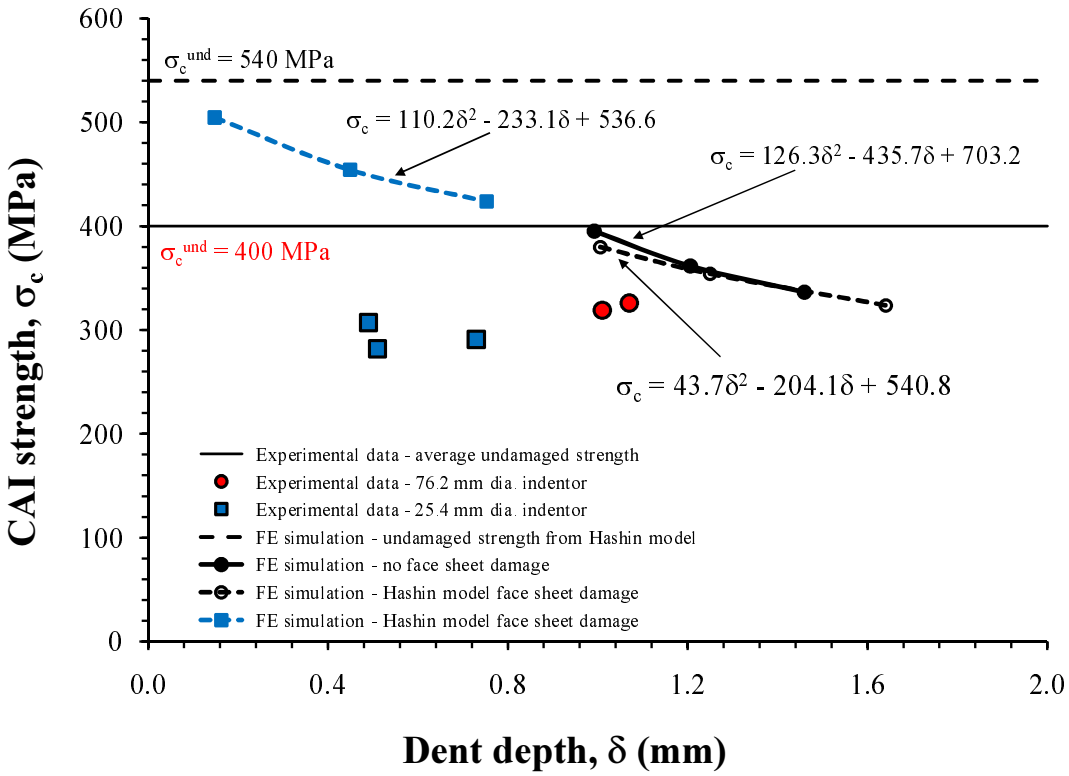

Figure 4.48: CAI strength as a function of dent depth - numerical results and experimental data (Q1-C1 panel geometry).

sitivity of compressive fiber failure on presence of fiber imperfections, it is very likely that the present model inadequately captures the onset of micro-buckling in the wavy sandwich face sheets, and hence overestimates the compressive strength in both undamaged and indented specimens.

The large discrepancy between simulation and experimental data can be further explained by examining damage mechanisms that control failure of the Q1-C1 specimens. In the simulation, the CAI failure initiated with compressive fiber failure of a single element in the center of the dent. The initiation of damaged occurred in the top-most, 0° ply, followed by slow propagation in the direction lateral to the load direction. Upon reaching a critical size, the damage area caused a load re-distribution in the face sheet, triggering failure of the bottom-

most, 0° ply. This was followed by sequential failure of the 45/-45/90° plies and the ultimate panel collapse. In the experiment, all but one specimen with the Q1 layup exhibited damage in the forms of delamination buckling and unstable delamination growth. Presence of these failure mechanisms in the experiment resulted in significant reduction of the residual strength, especially when compared to specimens that exhibited compressive fiber failure alone. Because the present FE model does not yet include the initiation or evolution of interlaminar delaminations, their presence is not accounted for during panel failure, hence causing further discrepancy between the experimental and numerical strength values.

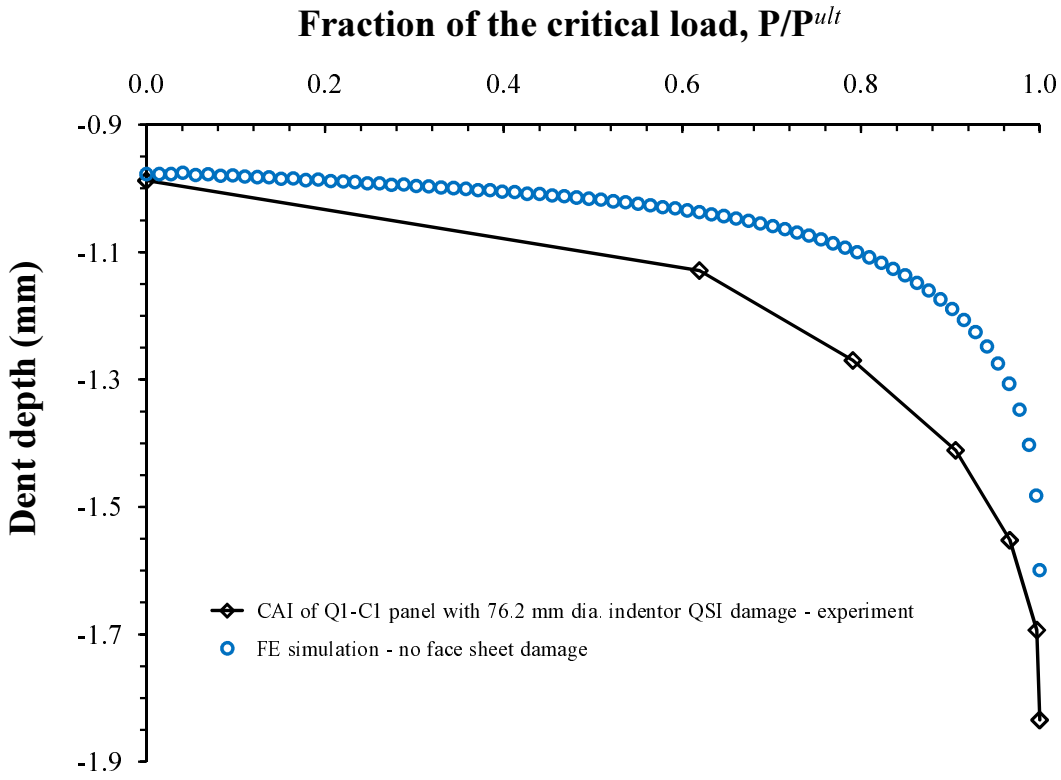

Figure 4.49: Dent depth as a function of the applied load (Q1-C1 panel geometry). The applied load is normalized by the ultimate failure load.

In the case of CAI simulation of the panel indented using a 76.2 mm dia.

indentor, the predicted failure occurred due to dent deepening and eventual unstable growth to the free edges of the panel. A comparison of experimentally observed damage evolution to the simulation results is presented with a sequence of Moiré images in Figure 4.50. In this figure, the four photos on the left represent the experimentally determined sequence of dent profiles measured during a CAI test using a 3.5 lpmm Moiré grating. The sequence of images on the right depicts the simulated dent profiles extracted from the model and post-processed using ABAQUS/CAE Viewer to "mimic" the 3.5 lpmm Moiré grating contours. A comparison between the simulated and experimentally measured dent depths as a function of the applied load fraction (i.e. applied load divided by ultimate load) is presented in Figure 4.49. Qualitatively, the experimental and simulated dent profiles in Figure 4.50 show an excellent agreement in evolution of the dent shape and area. Quantitatively, the simulation underestimates the evolution of dent depth and overestimates the CAI strength. However, the discrepancies are less significant than for the 25.4 mm dia. indentor simulation. The improved correlation between simulation and experiment can be related to the fact that the core plays a much greater role in progression and ultimate failure of the sandwich panel.

4.4 Discussion and Conclusions

A combined experimental and numerical study for assessing the residual compressive strength of sandwich panels with BVID has been presented. In an attempt to reveal the underlying damage mechanisms and highlight competition between different modes of failure, the experimental efforts considered sandwich panels with a broad range of quasi-isotropic face sheets layups and light-

weight aluminum honeycomb cores. BVID was induced in test specimens using QSI, and damage tolerance was evaluated using a CAI test. The experiments revealed three distinct modes of failure characterized by combinations of indentation growth, delamination buckling, fiber failure, and global instability. The study found no correlation between a single metric (e.g. dent depth or delamination area) and damage tolerance for all configurations considered. Residual strength was found to be dependent on specific panel type (i.e. face sheet layup and core type) and extent of internal damage due to QSI. In terms of damage tolerance at BVID, the damage caused by small diameter indentor was more critical in terms of strength reduction. Moreover, the Q1 layup, having a 0° ply near the free surface, was found to be increasingly prone to delamination buckling, leading to higher reduction in residual strength. In contrast, the Q2 layup yielded the most similar damage tolerance results for QSI damage from both small and large indentor diameters. In addition, the dense C3 core provided high undamaged strength and best damage resistance for a given impact event; however, for a given QSI dent depth, the baseline C1 core provided best damage tolerance.

In addition to the experimental efforts, this study developed numerical models for assessing damage tolerance of impact-damaged composite sandwich structures. The purpose of the modeling effort was to provide further insight into the aforementioned experimental observations and to develop a robust tool for design and analysis of damage tolerant sandwich composite structures. To improve upon the existing state-of-the-art, both QSI and CAI were explicitly modeled within a single simulation. To extend functionality, the numerical models were developed in the framework of the finite element method by employing the commercially available Abaqus® software. The preliminary mod-

eling efforts focused on development of an improved honeycomb core material model to assess core damage during indentation and core damage evolution during CAI. Two distinct modeling approaches were explored for representing non-linear behavior of the damaged honeycomb core. In the first approach, the core was represented as a homogenized geometry with an orthotropic plasticity model. In the second approach, the honeycomb cell walls were explicitly represented using thin, elastic-plastic shell elements. In either approach, the core model was combined with a progressive, intra-laminar failure model to represent a QSI/CAI composite sandwich specimen.

Simulation results of QSI to BVID were insensitive to evolution of intra-laminar face sheet damage and were primarily controlled by the non-linear behavior of the damaged honeycomb core. In general, the simulation of QSI using the homogenized core model correlated poorly with the experimental data, under-predicting residual dent area and significantly over-predicting the maximum dent depth. In contrast, simulation of QSI using the explicit core model provided significantly better results, predicting accurately the reaction force and displacement of the indentors and the residual dent area and depth. For the 76.2 mm dia. QSI case, the failure mode during CAI (unstable dent growth) was accurately simulated for both the explicit and homogenized core models. While residual strength was over-predicted using either core model, the explicit core model provided a more accurate prediction than did the homogenized core model. Since failure of panels with extensive core damage was largely controlled by the core crushing behavior, inclusion of the intra-laminar face sheet damage model had minor effect on the predicted residual strength. For the 25.4 mm dia. QSI case, both simulation and experimental results revealed that core crushing was relatively insignificant and consequently played little role in fail-

ure of the panel during CAI. Moreover, simulation (using both homogenized and explicit core models) grossly overestimated residual strength, suggesting that the intra-laminar damage model used was inadequate in predicting damage evolution and ultimate sandwich panel failure during CAI. To accurately predict failure of impact damaged sandwich structures considered in this study, modeling should account for inter-laminar delaminations.

Overall, development of the numerical methods presented in this study demonstrated the feasibility of predicting the processes of QSI and CAI using a single numerical simulation. Based on the numerical results, two recommendations are now offered to further improve the proposed QSI/CAI model. First, to accurately capture the onset of compressive fiber failure using the Hashin progressive failure model, all of the model input parameters must be measured for laminate coupons that are geometrically representative of co-cured sandwich panel face sheets (e.g. containing wavy plies). Additionally, since damage tolerance cannot be accurately determined without modeling inter-laminar delaminations, these must be incorporated as part of the present face sheet model. For specimens indented with the 76.2 mm dia. indentor, modeling of inter-laminar delaminations will lower the overall bending stiffness of the indented face sheet, increasing dent growth and causing unstable dent growth at lower compressive loads. For specimens indented with the 25.4 mm. dia. indentor, accurate modeling of initiation and evolution of delaminations may provide a means of simulating the process of delamination buckling. Delamination buckling will likely contribute to earlier initiation of face sheet failure, likely lowering the predicted compressive failure loads. Currently there are two approaches implemented in Abaqus® that can be employed for modeling inter-laminar delaminations. These include the virtual crack closure technique (VCCT) [89] and the

cohesive zone constitutive approach [90, 91]. The VCCT requires explicit representation of delaminations as geometrical discontinuities between individual plies of the laminate where shape and location of each individual delamination would be determined from non-destructive and/or destructive evaluation of indented panels. Currently Abaqus® provides tools necessary to calculate the total energy release rate (including the mode I/II components) and to simulate the progressive delamination growth. The cohesive zone constitutive approach does not require geometrically explicit representation of delaminations. The cohesive zone approach allows, to some extent, the evolution of delamination geometry. A subject of an ongoing research is the implementation of these two methods into the numerical framework presented in this study.

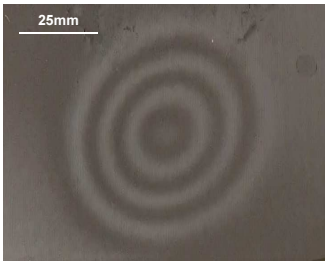

(a) P = 0

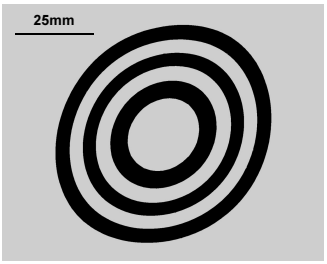

(b) P = 0

(c) P = 75% P^{ult}

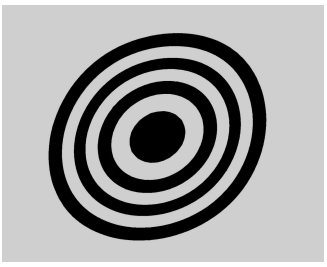

(d) P = 75% P^{ult}

(e) P = 99% P^{ult}

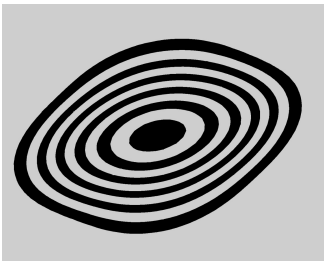

(f) P = 99% P^{ult}

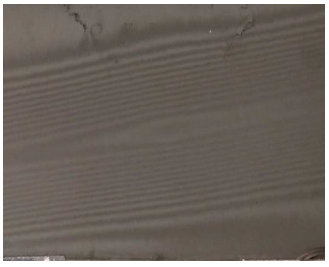

(g) failure

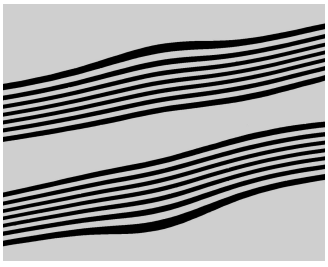

(h) failure

Figure 4.50: Sequence of Moiré images during CAI of Q1-C1 specimen with QSI damage from 76.2 mm dia. indentor. The column on the left shows the experimental data, while column on the right depicts the simulated Moiré contours post-precessed with ABAQUS/CAE Viewer.

APPENDIX A

THE UNDAMAGED SPECIMEN STRENGTH DATA SUMMARY

Nomenclature:

P^{ult} - ultimate failure load

N_x^{ult} - ultimate edge load (failure load divided by specimen width)

ε^{ult} - average strain at failure (average of four alignment gage data)

DB - delamination buckling

FF - fiber failure

GI - global instability

Table A.1: Summary table of EC test data. Note that all strength values was computed based on an assumed double face sheet thickness of 2.032 mm, and not the measured values listed below.

Specimen	Width (mm)	Length (mm)	Face sheet thickness (mm)	P^{ult} (kN)	N_x^{ult} (kN/mm)	Strength (MPa)	ε^{ult} (mm/mm)
1-Q1-C1-1	152.4	167.1	0.710	128.6	0.844	415.4	0.00780
1-Q1-C1-3	50.0	171.3	0.719	43.3	0.864	425.4	0.00814
2-Q1-C1-6	54.2	177.8	0.720	39.6	0.731	359.6	0.00703
1-Q1-C2-3	47.9	177.4	0.762	32.7	0.682	335.9	0.00666
1-Q1-C2-4	50.4	176.6	0.785	36.0	0.714	351.3	0.00709
1-Q1-C2-5	49.1	177.8	0.743	34.0	0.693	341.0	0.00665
2-Q1-C2-5	51.4	178.0	0.756	38.1	0.742	364.9	0.00751
2-Q1-C3-3	50.8	177.9	0.799	43.0	0.846	416.2	0.00791
2-Q1-C3-4	51.7	177.6	0.772	43.9	0.849	417.8	0.00762
3-Q1-C3-5	51.4	177.5	0.721	45.0	0.877	431.4	0.00823
3-Q1-C3-6	51.0	177.9	0.732	43.8	0.858	422.2	0.00827
2-Q2-C1-5	51.7	177.3	0.696	41.1	0.795	391.3	0.00748
3-Q2-C1-5	50.7	177.8	0.726	45.2	0.891	438.6	0.00831
3-Q2-C1-6	50.9	177.7	0.742	52.0	1.021	502.4	0.00969
1-Q3-C1-3	50.5	177.5	0.763	42.4	0.841	413.9	0.00805
1-Q4-C2-4	49.8	177.8	0.711	44.2	0.887	436.8	0.00799
1-Q4-C2-5	49.8	177.8	0.730	38.5	0.774	381.0	0.00648
1-Q4-C3-5	50.9	177.8	0.699	51.9	1.020	502.0	0.00946

APPENDIX B

SPECIMEN GEOMETRY AND QUASI-STATIC INDENTATION RESULTS

Table B.1: Specimen geometry and quasi-static indentation results - 25.4 mm dia. indentor

Specimen	Width (mm)	Length (mm)	Face sheet thickness (mm)	QSI load (kN)	Dent depth (mm)	Dent dia. (mm)	Dent area (cm^2)	Planar delam. area (cm^2)
2-Q1-C1-2	153.8	181.6	0.725	1.30	0.51	37.6	11.1	2.06
2-Q1-C1-3	152.2	177.8	0.742	1.31	0.49	38.1	11.4	1.87
2-Q1-C1-4	153.5	177.8	0.742	1.88	0.73	45.7	16.4	2.52
1-Q1-C2-2	151.2	177.0	0.787	1.30	0.55	36.3	10.4	4.00
2-Q1-C2-3	152.8	177.8	0.752	1.32	0.48	33.8	9.0	4.00
2-Q1-C2-4	153.6	182.4	0.751	1.31	0.38	33.8	9.0	4.00
2-Q1-C3-2	154.0	177.8	0.782	1.77	0.43	27.9	6.1	3.61
3-Q1-C3-2	153.3	182.4	0.721	1.88	0.53	31.8	7.9	3.55
3-Q1-C3-3	152.9	177.8	0.709	1.32	0.29	23.6	4.4	2.71
2-Q2-C1-2	154.4	177.8	0.726	1.31	0.46	34.3	9.2	3.03
2-Q2-C1-3	152.6	177.8	0.726	1.31	0.46	36.8	10.7	3.35
3-Q2-C1-2	154.4	177.8	0.725	1.31	0.46	35.1	9.6	2.71
3-Q2-C1-3	153.0	181.6	0.727	1.43	0.53	39.4	12.2	2.58
3-Q2-C1-4	151.6	177.3	0.734	1.88	0.75	47.8	17.9	3.42
1-Q3-C1-2	152.3	177.8	0.781	1.30	0.47	39.4	12.2	4.00
1-Q4-C2-1	151.9	177.8	0.726	1.31	0.53	37.6	11.1	2.26
1-Q4-C2-3	149.5	177.8	0.747	1.31	0.52	36.3	10.4	2.32
1-Q4-C3-2	152.4	177.8	0.752	1.31	0.30	27.9	6.1	2.84
1-Q4-C3-4	152.5	175.3	0.757	1.76	0.46	30.7	7.4	3.94

Table B.2: Specimen geometry and quasi-static indentation results - 76.2 mm dia. indentor

Specimen	Width (mm)	Length (mm)	Face sheet thickness (mm)	QSI load (kN)	Dent depth (mm)	Dent dia. (mm)	Dent area (cm^2)	Planar delam. area (cm^2)
1-Q1-C1-2	151.3	168.7	0.760	2.81	1.07	59.2	27.5	NA
2-Q1-C1-1	154.0	177.8	0.738	2.82	1.01	57.2	25.7	NA
1-Q1-C2-1	151.8	180.6	0.814	2.81	0.97	55.9	24.5	NA
2-Q1-C2-1	154.8	177.8	0.732	2.83	0.96	54.1	23.0	NA
2-Q1-C2-2	153.5	177.8	0.734	2.81	1.03	54.6	23.4	NA
2-Q1-C3-1	152.4	177.8	0.803	3.54	1.01	47.0	17.3	NA
3-Q1-C3-1	153.6	181.6	0.733	3.54	1.06	47.0	17.3	NA
3-Q1-C3-4	151.0	173.7	0.709	2.85	0.91	39.4	12.2	NA
1-Q2-C1-1	152.5	177.8	0.808	4.46	1.69	71.1	39.7	NA
1-Q2-C1-2	151.4	177.8	0.749	2.84	1.04	57.2	25.7	NA
1-Q2-C1-4	152.4	177.8	0.838	4.45	1.68	72.4	41.2	NA
2-Q2-C1-1	154.4	177.8	0.711	2.82	0.93	57.2	25.7	NA
2-Q2-C1-4	152.8	182.1	0.730	2.96	1.05	57.2	25.7	NA
3-Q2-C1-1	153.7	177.8	0.730	2.82	0.91	57.2	25.7	NA
1-Q3-C1-1	152.4	177.8	0.747	2.80	1.10	54.6	23.4	NA
1-Q3-C1-4	152.4	181.0	0.768	4.41	1.49	72.4	41.2	NA
1-Q4-C2-2	148.5	177.3	0.744	2.82	1.02	56.6	25.2	NA
1-Q4-C3-1	152.4	177.8	0.747	2.81	0.91	41.9	13.8	NA

APPENDIX C

THE COMPRESSION AFTER IMPACT TEST DATA SUMMARY

Table C.1: Summary of CAI tests data - 25.4 mm dia. indentor. Note that all strength values was computed based on an assumed double face sheet thickness of 2.032 mm, and not the measured values listed below.

Specimen	P^{ult} (kN)	N_x^{ult} (kN/mm)	Strength (MPa)	ε^{ult} (mm/mm)	Residual Strength (%)	Failure strain retention (%)	Failure Mode
2-Q1-C1-2	88.2	0.574	282.2	0.00511	69.7	67.4	DB
2-Q1-C1-3	94.9	0.623	306.8	0.00522	75.8	69.0	DB
2-Q1-C1-4	91.0	0.593	291.9	0.00505	72.1	66.7	DB
1-Q1-C2-2	69.1	0.457	224.9	0.00345	64.6	49.4	DB
2-Q1-C2-3	84.3	0.551	271.3	0.00483	77.9	69.2	FF
2-Q1-C2-4	76.6	0.499	245.6	0.00436	70.5	62.4	DB
2-Q1-C3-2	84.3	0.548	269.4	0.00458	63.9	57.2	DB
3-Q1-C3-2	76.8	0.501	246.6	0.00419	58.5	52.3	DB
3-Q1-C3-3	84.3	0.551	271.3	0.00468	64.3	58.4	DB
2-Q2-C1-2	99.4	0.643	316.6	0.00538	71.3	63.3	FF
2-Q2-C1-3	97.2	0.637	313.4	0.00521	70.6	61.4	FF
3-Q2-C1-2	97.7	0.633	311.5	0.00560	70.1	66.0	FF
3-Q2-C1-3	95.3	0.623	306.4	0.00519	69.0	61.1	FF
3-Q2-C1-4	96.8	0.639	314.2	0.00534	70.8	62.9	FF
1-Q3-C1-2	79.0	0.518	255.1	0.00400	61.7	49.6	DB
1-Q4-C2-1	93.1	0.613	301.6	0.00523	69.1	65.5	FF
1-Q4-C2-3	99.5	0.666	327.6	0.00587	75.0	73.4	FF
1-Q4-C3-2	98.4	0.646	317.7	0.00570	63.3	60.2	FF
1-Q4-C3-4	93.0	0.610	300.1	0.00509	59.8	53.8	DB

Table C.2: Summary of CAI tests data - 76.2 mm dia. indentor. Note that all strength values was computed based on an assumed double face sheet thickness of 2.032 mm, and not the measured values listed below.

Specimen	P^{ult} (kN)	N_x^{ult} (kN/mm)	Strength (MPa)	ε^{ult} (mm/mm)	Residual Strength (%)	Failure strain retention (%)	Failure Mode
1-Q1-C1-2	100.2	0.662	325.8	0.00570	80.5	75.3	GI
2-Q1-C1-1	100.0	0.649	319.5	0.00552	78.9	73.0	FF
1-Q1-C2-1	88.3	0.582	286.3	0.00500	82.2	71.7	FF
2-Q1-C2-1	81.0	0.523	257.6	0.00450	74.0	64.5	DB
2-Q1-C2-2	87.3	0.569	280.1	0.00508	80.4	72.8	FF
2-Q1-C3-1	88.7	0.582	286.5	0.00496	67.9	62.0	DB
3-Q1-C3-1	87.8	0.572	281.4	0.00496	66.7	61.9	DB
3-Q1-C3-4	91.1	0.603	296.8	0.00524	70.4	65.5	DB
1-Q2-C1-1	83.0	0.544	267.8	0.00445	60.3	52.4	GI
1-Q2-C1-2	94.8	0.626	308.2	0.00507	69.4	59.8	GI
1-Q2-C1-4	87.3	0.573	282.0	0.00486	63.5	57.2	GI
2-Q2-C1-1	97.1	0.629	309.6	0.00529	69.7	62.3	DB
2-Q2-C1-4	95.3	0.624	306.9	0.00533	69.1	62.7	DB
3-Q2-C1-1	99.9	0.650	319.9	0.00567	72.0	66.8	FF
1-Q3-C1-1	87.1	0.572	281.4	0.00505	68.0	62.7	GI
1-Q3-C1-4	79.9	0.524	258.1	0.00460	62.4	57.1	GI
1-Q4-C2-2	84.6	0.570	280.3	0.00397	64.2	49.7	GI
1-Q4-C3-1	118.5	0.778	382.6	0.00685	76.2	72.4	FF

APPENDIX D

HOMOGENIZED HONEYCOMB CORE MODEL INPUT DATA

Table D.1: Elastic material properties for Q1 - HexWeb, CR-III, 3.2 mm cell size, 5052-H39 aluminum honeycomb core

E_1 (GPa)	E_2 (GPa)	E_3 (GPa)	G_{12} (GPa)	G_{13} (GPa)	G_{23} (GPa)	ν_{12}	ν_{13}	ν_{23}	Density (kg/mm^3)
148E-6*	147E-6*	1.1**	89E-6*	0.17**	0.127*	1.0*	1E-5*	1E-5*	49.7***

* - estimated

** - measured experimentally

*** - from Ref. [69]

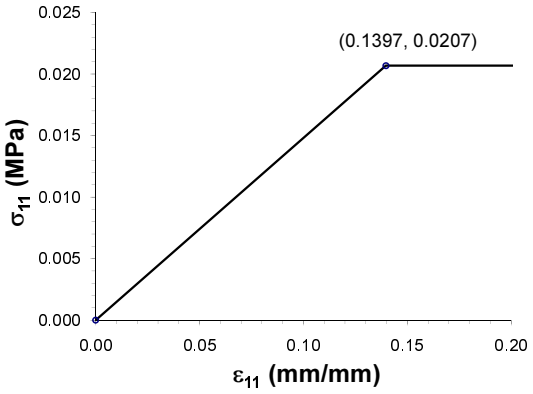

(a) $\sigma_{11} - \epsilon_{11}$

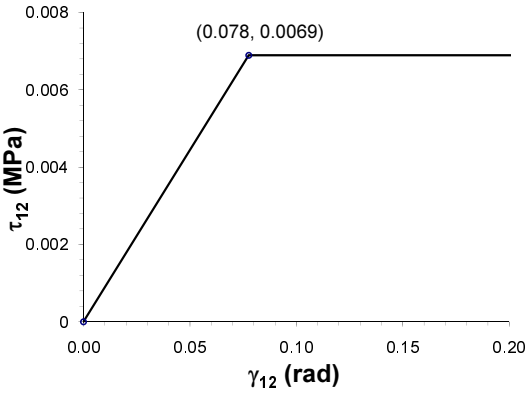

(b) $\tau_{12} - \gamma_{12}$

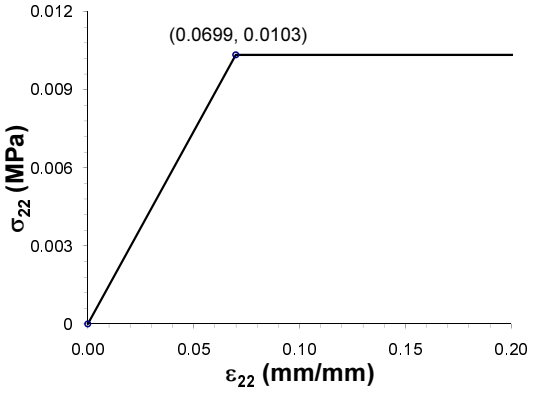

(c) $\sigma_{22} - \epsilon_{22}$

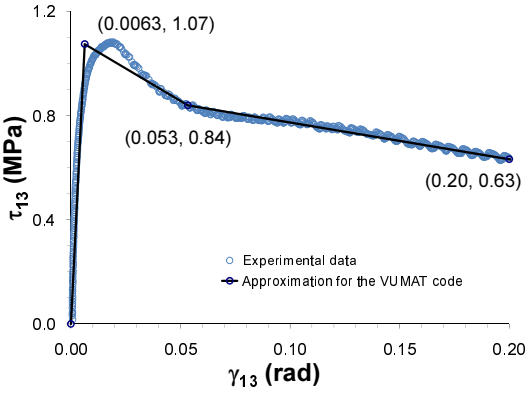

(d) $\tau_{13} - \gamma_{13}$

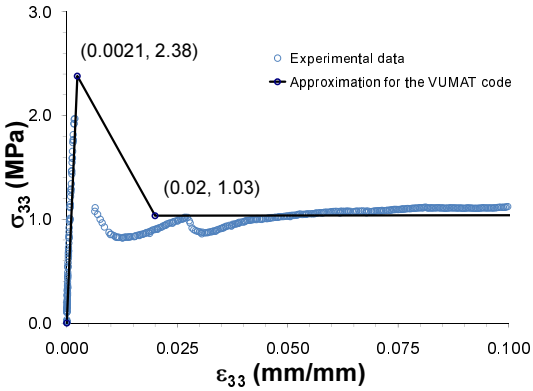

(e) $\sigma_{33} - \epsilon_{33}$

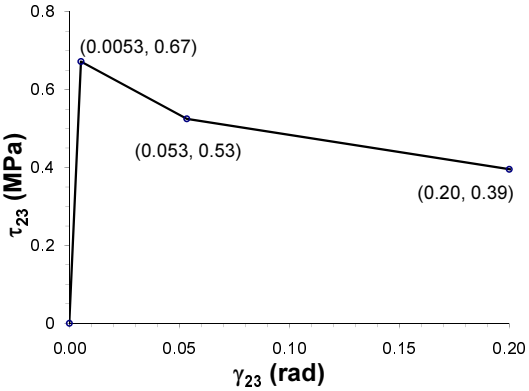

(f) $\tau_{23} - \gamma_{23}$

Figure D.1: The six hardening functions used as input in the homogenized core VUMAT model. The $\sigma_{33} - \epsilon_{33}$ figure shows a single experimental curve. The $\sigma_{33} - \epsilon_{33}$ approximation used in the VUMAT is based on an average response from several tests.

BIBLIOGRAPHY

[1] C.L. Bowman, J.C. Thesken, K.C. Chuang, and C.P. Arendt. Graphite Fiber/Polyimide Composites Subjected to Moisture and Rapid Heating. *46th Internation SAMPE Technical Conference*, pages 1–11, 2001.

[2] M. Meador. Materials Challenge Diversification and the Future. *In 40th International SAMPE Symposium and Exhibition*, pages 268–276, 1995.

[3] B.P. Rice and C.W. Lee. Study of Blister Initiation and Growth in a High-Temperature Polyimide. *29th Internation SAMPE Technical Conference*, pages 675–685, 1997.

[4] R.J. Morgan, , E.E. Shin, and J.E. Lincoln. Thermal Properties of High Temperature Polymer Matrix Fibrous Composites. *Handbook of Thermal Analysis and Calorimetry: Applications to Polymers and Plastics*, 3:491–518, 2002.

[5] CMH-17-1F. *Composite Materials Handbook 17, Volume 1: Polymer Matrix Composites Guidelines for Characterization of Structural Materials*. Materials Sciences Corporation, 2002.

[6] V. Muralidharan and C.Y. Hui. Steam Pressure Generated in a Spherical Cavity in a Moisture Saturated Polymer Matrix Composite During Rapid Heating. *Journal of Engineering Materials and Technology*, 128(1):50–54, 2006.

[7] V. Muralidharan, C.Y. Hui, R.K. Krishnan, and K.D. Papoulia. A Flow Through Porous Media Model for Pore Pressure During Heating of Polymer Matrix Composites. *Composites Science and Technology*, 66(10):1409–1417, 2006.

[8] C.Y. Hui, V. Muralidharan, and M.O. Thompson. Steam Pressure Induced in Crack-Like Cavities in Moisture Saturated Polymer Matrix Composites During Rapid Heating. *International Journal of Solids and Structures*, 42:1055–1072, 2005.

[9] V. Muralidharan and C.Y. Hui. Effect of Heating Rate on Steam Pressure Induced in Crack-Like Cavities in Moisture Saturated Polymer Matrix Composites. *International Journal of Solids and Structures*, 43(20):6085–6099, 2006.

[10] K.C. Chuang, C.L. Bowman, T.K. Tsotis, and C.P. Arendt. 6F-Polyimides With Phenylenthynyl Endcap for 315-370°C Applications. *High Performance Polymers*, 15:459–472, 2003.

[11] J.P. Holman. *Heat Transfer*. McGraw-Hill, Inc., New York, NY, 1997.

[12] J. Crank. *The Mathematics of Diffusion*. Oxford Science Publications, Oxford University Press, Walton Street, Oxford, 1975.

[13] P. Bhargava, K.C. Chuang, K. Chen, and A.T. Zehnder. Moisture Diffusion Properties of HFPE-II-52 Polyimide. *Journal of Applied Polymer Science*, 102(4):3471–3479, 2006.

[14] J.N. Antonakakis, P. Bhargava, K.C. Chuang, and A. Zehnder. Linear Viscoelastic Properties of HFPE-II-52 Polyimide. *Journal of Applied Polymer Science*, 100(4):3255–3263, 2005.

[15] J.N. Antonakakis. Linear Viscoelastic Properties of HFPE-II-52 Polyimide, M.S. Thesis. *The Department of Theoretical and Applied Mechanics, Cornell University*, 2005.

[16] K. Shivakumar, H. Chen, and G. Holloway. Gas Turbine Environment Effect on Morphology and Mechanical Properties of Pultruded Composite. *Journal of Applied Polymer Science*, 108:189–198, 2008.

[17] G.S. Springer. *Environmental Effects on Composite Materials*. Technomic Publishing Company, Westport, CT 06880, 1981.

[18] MatWeb Material Property Data, The Properties of Polymide. 2007.

[19] ASTM-D3171. Standard Test Methods for Constituent Content of Composite Materials. *Annual Book of ASTM Standards, American Society for Testing and Materials*.

[20] P. Bhargava. High Temperature Properties of HFPE-II-52 Polyimide Resin and Composites, Phd Thesis. *The Department of Theoretical and Applied Mechanics, Cornell University*, 2007.

[21] M.W. Czabaj, A.T. Zehnder, and K.C. Chuang. Blistering of Moisture Saturated Graphite/Polyimide Composites Due to Rapid Hating. *Journal of Composite Materials*, 43(2):153–174, 2009.

[22] S. Neumann and G. Marom. Free-Volume Dependent Moisture Diffusion Under State in Composite Materials. *Journal of Material Science*, 21:26–30, 1986.

[23] J.N. Reddy. *Energy Principles and Variational Methods in Applied Mechanics*. John Wiley and Sons, Inc., Hoboken, NJ 07030, 2002.

[24] R.M. Sullivan and E.H. Stokes. A Model For The Effusion of Water in Carbon Phenolic Composites. *Mechanics of Materials*, 26:197–207, 1997.

[25] A.C. Loos and G.S. Springer. Moisture Absorption of Graphite/epoxy Composites Immersed in Liquids and in Humid Air. *In: Springer G.S. (Ed.), Enviromental Effects on Composite Materials, Technomic*, 1:34–50, 1981.

[26] R. Szilard. *Theory and Analysis of Plates - Classical and Numerical Methods*. Prentice-Hall, Inc., Englewood Cliffs, NJ 07632, 1974.

[27] K.C. Chuang, D.S. Papadopoulos, and C.P. Arendt. High Tg Polyimimide Composits ii. *In 47th International SAMPE Symposium and Exhibition*, pages 1175–1187, 2002.

[28] N. Alif, L.A. Carlsson, and L. Boogh. The Effect of Weave Pattern and Crack Propagation Direction on Mode I Delamination Resistance of Woven Glass and Carbon Composites. *Composites Part B*, 29(B):603–611, 1998.

[29] R.F. Gibson. *Principles of Composite Material Mechanics*. McGraw-Hill, Inc., New York, NY, 1994.

[30] M.W. Czabaj. Determination of the Mode I and Mode II Toughness of Graphite/Polyimide Composites at Room and Elevated Temperatures. *AIAA Regional Student Conference*, 2004.

[31] A.J. Kinloch, S.J. Shaw, D.A. Tod, and D.L. Hunston. Deformation and Fracture Behaviour of a Rubber-Toughened Epoxy: 1. Microsctructure and Fracture Studies. *Polymer*, 24:1341–1354, 1983.

[32] S. Hashemi, A.J. Kinloch, and J.G. Williams. Corrections Needed in Double-cantilever Beam Tests for Assessing the Interlaminar Failure of Fibre-composites. *Journal of Materials Science Letters*, 8:125–129, 1989.

[33] ASTM 5528. Standard Test Method for Mode i Interlaminar Fracture Toughness of Unidirectional Fiber-Reinforced Polymer Matrix Composites. *Annual Book of ASTM Standards, American Society for Testing and Materials*.

[34] B. Bednarcyk, S. Arnold, C.S. Collier, and P. Yarrington. Preliminary Structural Sizing and Alternative Materials Trade Study for CEV Crew Module.

48th AIAA/ASME/ASCE/AHS/ASC Structures, Structural Dynamics, and Materials Conference, Honolulu, HI, 2007.

[35] C. Collier, P. Yarrington, M. Pickenheim, B. Bednarcyk, and J. Jeans. Analysis Methods used on the NASA Composite Crew Module (CCM). *49th AIAA/ASME/ASCE/AHS/ASC Structures, Structural Dynamics, and Materials Conference, Schaumburg, IL*, 2008.

[36] W.B. Avery and D.H. Grande. Influence of Materials and Layup Parameters on Impact Damage Mechanisms. *Proceedings of the 22nd International Society for the Advancement of Materials and Process Engineering Technical Conference*, 22:470–483, 1990.

[37] P.H. Bull. Damage Tolerance and Residual Strength of Composite Sandwich Structures. *Ph.D. Thesis, Department of Aeronautical and Vehicle Engineering, Kungliga Tekniska Högskolan, Stockholm, Sweden*, 2004.

[38] W.J. Cantwell, R. Scudamore, J. Ratcliffe, and P. Davies. Interfacial Fracture in Sandwich Laminates. *Composites Science and Technology*, 59:2079–2085, 1999.

[39] T.N. Nicholas, J.A. Zukas, and H.F. Swift. *Impact Dynamics*. John Wiley and Sons, New York, NY, 1982.

[40] J. Tomblin, T. Lacy, B. Smith, S. Hooper, A. Vizzini, and Lee S. Review of Damage Tolerance for Composite Sandwich Airframe Structures. *Final Report, Federal Aviation Administration Report, DOT/FAA/AR-99/49*, 1999.

[41] P. Shyprykevich, J. Tomblin, L. Ilcewicz, A.J. Vizzini, T.E. Lacy, and Y. Hwang. Guidelines for Analysis, Testing, and Nondestructive Inspection of Impact-damaged Composite Sandwich Structures. *Final Report, Federal Aviation Administration Report, DOT/FAA/AR-02/121*, 2003.

[42] A.T. Nettles, D.G. Lance, and A.J. Hodge. An Examination of Impact Damage in Glass/Phenolic and Aluminum Honeycomb Core Composite Panels. *NASA Technical Paper 3042, Marshall Space Flight Center, Huntsville, AL*, 1990.

[43] P.H. Tshang and P.A. Lagace. Failure Mechanisms of Impact-damaged Sandwich Panels Under Uniaxial Compression. *35th AIAA/ASME/ASCE/AHS/ASC Structures, Structural Dynamics, and Materials Conference, Hilton Head, SC*, pages 745–754, 1994.

[44] C. Moody and A.J. Vizzini. Damage Tolerance of Composite Sandwich Structures. *Final Report, Federal Aviation Administration Report, DOT/FAA/AR-99/91*, 2000.

[45] Z. Xie, A.J. Vizzini, and M. Yang. On Residual Compressive Strength Prediction of Compressive Sandwich Panels After Low-velocity Impact Damage. *Sandwich Structures 7: Advancing with Sandwich Structures and Materials*, pages 363–372, 2005.

[46] J.G. Ratcliffe, W.C. Jackson, and J. Schaff. Predicting the Compression Strength of Impact-damaged Sandwich Panels. *Proceedings of the American Helicopter Society 60th Annual Forum, Baltimore, MD*, 2004.

[47] J.G. Ratcliffe and W.C. Jackson. A Finite Element Analysis for Predicting the Residual Compressive Strength of Impact-damaged Sandwich Panels. *NASA Technical Memorandum, NASA/TM-2008-215341*, 2008.

[48] A. Nettles and J. Jackson. Compression After Impact Testing of Sandwich Composites for Usage on Expandable Launch Vehicles. *Journal of Composite Materials*, 44(6):707–738, 2010.

[49] P.J. Minguet. A Model for Predicting the Behavior of Impact-damaged Minimum Gage Sandwich Panels Under Compression. *32st AIAA/ASME/ASCE/AHS/ASC Structures, Structural Dynamics, and Materials Conference, Baltimore MD*, pages 1112–1122, 1991.

[50] ASTM C297. Test Method for Flatwise Tensile Strength of Sandwich Constructions. *Annual Book of ASTM Standards, American Society for Testing and Materials*, 15.03, 2008.

[51] T.E. Lacy and Y. Hwang. Numerical Modeling of Impact-damaged Sandwich Composites Subjected to Compression-after-impact Loading. *Composite Structures*, 61:115–128, 2003.

[52] Y. Hwang and T.E. Lacy. Numerical Estimates of the Compressive Strength of Impact-damaged Sandwich Structures. *Journal of Composite Materials*, 41(3):367–388, 2007.

[53] Hexcel Corporation (http://www.hexcel.com). *HexPly® 8552 Product Data Sheet*, 2007.

[54] J.E. Williamson and P.A. Lagace. Response Mechanisms in the Impact of

Graphite/Epoxy Honeycomb Sandwich Panels. *Proceedings of the American Society for Composites Eighth Technical Conference on Composite Materials, Cleveland, OH*, pages 287–297, 1993.

[55] E.J. Herup and A.N. Palazotto. Low-velocity Impact Damage Initiation in Graphite/Epoxy/Nomex Honeycomb-sandwich Plates. *Composites Science and Technology*, 57:1581–1598, 1997.

[56] R. Ferri and B.V. Sankar. A Comparative Study on the Impact Resistance of Composite Laminates and Sandwich Panels. *Thermoplastic Composite Materials*, 10:304–315, 1997.

[57] D.W. Oplinger and J.M. Slepetz. Impact Damage Tolerance of Graphite/Epoxy Panels. *Foreign Object Impact Damage to Composites, ASTM STP 568*, pages 30–48, 1975.

[58] A.K. Singh, B.D. Davidson, D.P. Eisenberg, M.W. Czabaj, and A.T. Zehnder. Barely Visible Impact Damage Evaluation of Sandwich Composite Structures. *51st AIAA/ASME/ASCE/AHS/ASC Structures, Structural Dynamics, and Materials Conference, Orlando FL*, 2010.

[59] ASTM C364. Test Method for Edgewise Compressive Strength of Sandwich Constructions. *Annual Book of ASTM Standards, American Society for Testing and Materials*, 15.03, 2008.

[60] M.K. Cvitkovich and W.C. Jackson. Compressive Failure Mechanisms in Composite Sandwich Structures. *Journal of the American Helicopter Society*, 44(4):260–268, 1999.

[61] S.W. Tsai and E.M. Wu. A General Theory of Strength for Anisotropic Materials. *Journal of Composite Materials*, 5(1):58–80, 1971.

[62] R.M. Jones. *Mechanics of Composite Materilas*. Hemisphere Publishing Corporation, New York, NY, 1975.

[63] D. Post, B. Han, and P. Ifju. *High Sensitivity Moire*. Springer-Verlag New York Inc., 175 Fifth Avenue, New York, NY 10010, 1994.

[64] D. Post, B. Han, and P. Ifju. Moire Methods for Engineering and Science - Moire Interferometry and Shadow Moire. *Photomechanics, Topics in Applied Physics*, 77:151–196, 2000.

[65] E.S. Greenhalgh. *Failure Analysis and Fractography of Polymer Composites*. Woodhead Publishing Limited and CRC Press LLC, Cambridge, UK, 2009.

[66] Z. Xue and J.W. Hutchinson. Constitutive Model for Quasi-static Deformation of Metallic Sandwich Cores. *International Journal for Numerical Methods in Engineering*, 61:2205–2238, 2004.

[67] Z. Xue, A. Vaziri, and J.W. Hutchinson. Non-uniform Hardening Constitutive Model for Compressible Orthotropic Materials with Application to Sandwich Plate Cores. *Computer Modeling in Engineering and Sciences*, 10(1):79–95, 2005.

[68] R. Hill. *The Mathematical Theory of Plasticity*. Oxford University Press, Oxford, Uk, 1998.

[69] Hexcel Corporation (http://www.hexcel.com). *HexWeb® CR-III Product Data Sheet*, 2007.

[70] H.L. Schreyer, Q.H. Zuo, and A.K. Maji. Anisotropic Plasticity Model for Foams and Honeycombs. *Journal of Engineering Mechanics*, 120(9):1913–1930, 1994.

[71] S.C. TerMaath, A.R. Ingraffea, and P.A. Wawrzynek. A Computational Fracture Mechanics Approach for the Analysis of Facesheet-from-core Disbond of Honeycomb Core Sandwich Panels. *Fatigue and Fracture Mechanics: 30th Volume, ASTM STP 1360, Paris, P.C., and Jerina, K.L., Eds., American Society for Testing and Materials, West Conshohocken, PA*, pages 169–182, 1999.

[72] D. Mohr and M. Doyoyo. Deformation-induced Folding Systems in Thin-walled Monolithic Hexagonal Metallic Honeycomb. *International Journal of Solids and Structures*, 41:3353–3377, 2004.

[73] C.C. Foo, G.B. Chai, and L.K. Seah. A Model to Predict Low-velocity Impact Response and Damage in Sandwich Composites. *Composites Science and Technology*, 68:1348–1356, 2008.

[74] C.C. Foo, L.K. Seah, and G.B. Chai. Low-velocity Impact Failure of Aluminum Honeycomb Sandwich Panels. *Composite Structures*, 85:20–28, 2008.

[75] L. Aktay, A.F. Johnson, and B.H. Kroplin. Numerical Modeling of Honeycomb Core Crush Behaviour. *Engineering Fracture Mechanics*, 75:2616–2630, 2008.

[76] S. Heimbs. Virtual Testing of Sandwich Core Structures Using Dynamic Finite Element Simulations. *Computational Materials Science*, 45:205–216, 2009.

[77] MIL-HDBK-5H. Metallic Materials and Elements for Aerospace Vehicle Structures - Aluminum. *U.S. Department of Defense*, 1998.

[78] Dassault Systèmes Simulia Corp. (http://www.simulia.com). *Abaqus 6.8 Documentation*, 2008.

[79] Z. Heimbs and A. Rotem. A Fatigue Criterion for Fiber-reinforced Materials. *Journal of Composite Materials*, 7:448–464, 1973.

[80] Z. Heimbs. Failure Criteria for Unidirectional Fiber Composites. *Journal of Applied Mechanics*, 47:329–334, 1980.

[81] W.S. Burton and A.K. Noor. Assessment of Continuum Models for Sandwich Panel Honeycomb Cores. *Computer Methods in Applied Mechanics and Engineering*, 145(3-4):341–360, 1997.

[82] P.P. Camanho, P. Maimí, and C.G. Dávila. Prediction of Size Effects in Notched Laminates Using Continuum Damage Mechanics. *Composites Science and Technology*, 67:2715–2727, 2007.

[83] C. Bisagni, R. Vescovini, and C.G. Dávila. Assessment of the Damage Tolerance of Posbuckled Hat-stiffened Panels Using Single-stringer Specimens. *48th AIAA/ASME/ASCE/AHS/ASC Structures, Structural Dynamics, and Materials Conference, Orlando, FL*, 2010.

[84] J.M. Whitney, C.E. Browning, and A. Mair. Analysis of the Flexure Test for Laminated Composite Materials. *ASTM Special Technical Publications*, 546:30–45, 1974.

[85] ASTM D6272. Standard Test Method for Flexural Properties of Unreinforced and Reinforced Plastics and Electrical Insulating Materials by Four-point Bending. *Annual Book of ASTM Standards, American Society for Testing and Materials*, 08.03, 2009.

[86] ASTM C365. Test Method for Flatwise Compressive Properties of Sandwich Cores. *Annual Book of ASTM Standards, American Society for Testing and Materials*, 15.03, 2008.

[87] D. Mohr, Z. Xue, and A. Vaziri. Quasi-static Indentation of a Honeycomb

Sandwich Plate: Experiments and Modeling. *Journal of Mechanics of Materials and Structures*, 1(3):581–604, 2006.

[88] D. Mohr and M. Doyoyo. A New Method for the Biaxial Testing of Cellular Solids. *Experimental Mechanics*, 43(2):173–182, 2003.

[89] E.F. Rybicki and M.F. Kanninen. A Finite Element Calculation of Stress Intensity Factors by a Modified Crack Closure Integral. *Engineering Fracture Mechanics*, 9:931–938, 1977.

[90] D. Dugdale. Yielding of Steel Sheets Containing Slits. *Journal of the Mechanics and Physics*, 8:100–104, 1960.

[91] G. Barenblatt. The Mathematical Theory of Equilibrium Cracks in Brittle Fracture. *Advances in Applied Mechanics*, 7:55–129, 1962.